FE-BASED MAGNETIC NANOMATERIALS: WET CHEMICAL SYNTHESIS, MAGNETIC PROPERTIES AND EXPLORATION ON APPLICATIONS

HONG XIAOLIANG

(M.E., NATIONAL UNIVERSITY OF SINGAPORE, SINGAPORE)

A THESIS SUBMITTED

FOR THE DEGREE OF DOCTOR OF PHILOSOPHY

DEPARTMENT OF MATERIALS SCIENCE AND ENGINEERING

2016

DECLARATION

I hereby declare that this thesis is my original work and it has been written by me in its entirety.

I have duly acknowledged all the sources of information which have been used in the thesis.

This thesis has also not been submitted for any degree in any university previously.

HONG XIAOLIANG

05 Jan 2016

ACKNOWLEDGEMENTS

First of all, I would like to express my sincere appreciation to my supervisor, Prof. Ding Jun, for his advice, guidance and tremendous help during my PhD study. His constant encouragement and immense knowledge helped me in all the time of research work and writing of this thesis.

I also would like making a grateful acknowledgement to XiaoWen for helping me revise my manuscripts and gave insightful comments, from which I benefited a lot. Moreover, I greatly appreciate the kind help from Ms Bao Nina for operating pulsed laser deposition machine and conducting SQUID measurement. I would like to acknowledge all my research group members for their kind assistance in various aspects.

A special mention is given to the lab officers in Department of Materials Science and Engineering for their technical support in sample characterization.

In addition, I would like to offer my deep gratitude to the financial support provided by the National University of Singapore. Last but not least, I would like thanking my family: my parents for giving birth to me and supporting me throughout my life.

SUMMARY

Even though the start of research based on Fe-based magnetic nanomaterials could be dated back to hundreds years ago, the considerably large amount of emerging fields for their applications, including spintronic structures in information storage, biomedical and environmental applications, magnetic sensors, magnetic energy harvesters, has spurred renewed interest on the application-related properties of Fe-based nanomaterial in both the nanoparticle and film forms. Besides, an exploration of a simple, wide, effective technique that can be used for growth of high-quality Fe-based magnetic nanoparticles and films is of great importance for better materialization of these potential Fe-based devices. This thesis mainly focuses on fabricating different magnetic Fe-based materials (ferrites and ferrous alloys, nanoparticle and film) with wet chemical method, investigating their growth mechanism and magnetic and electrical properties. In addition, the possible applications of as-fabricated Fe-based nanoparticles and films are studied. The contribution of the work is summarized as below:

(1) Investigation indicated that the external magnetic field plays an important role in determining the microstructure, magnetic properties of the Fe_3O_4 nanoparticles. The magnetic field can promote the change of Fe_3O_4 nanocuboctahedrons to nanocubes. Compared the hyperthermia property of as-fabricated nanocuboctahedrons and nanocubes Fe_3O_4, the intrinsic loss power (ILP) of the Fe_3O_4 nanocubes was much higher than that of nanocuboctahedrons due to

the surface magnetic effect.

(2) A general and facile method for broadly deposition of thick Fe_3O_4 film and other ferrites has been demonstrated. It had been found that the epitaxial high-quality Fe_3O_4 film could be deposited either on MgO substrates directly or Si substrates with Fe_3O_4 seed layer deposited by PLD. As-deposited Fe_3O_4 film could be easily patterned and shows potential applications for microwave and MEMS supercapacitor. Besides Fe_3O_4, different ferrite compounds have been successfully fabricated, including Co-ferrite with high coercivity and perpendicular anisotropy, and Ni-ferrite with high resistivity and enhanced magnetization.

(3) A typical Fe-3d alloy, FeCo, was studied in our work. Mono-dispersed FeCo nanoparticles were synthesized by a safe and ecofriendly facile chemical process. The FeCo nanoparticles have saturation magnetization up to 187 emu/g and shows excellent chemical stability. In addition, the control Fe/Co ratio could be achieved by change of precursor ratio and tuning of particle size could be realized through change of surfactant amount used. The cytotoxicity of as-synthesized nanoparticles was investigated after transferring the nanoparticle to water phase by the emulsion process and the results demonstrated high biocompatibility. The results showed that this method could also fabricate spherical Fe_3O_4 particles and self-assembly Co nanoneedles. With the similar method that was applied to deposit Fe_3O_4, bcc-FeCo film could be fabricated through

thermal decomposition with the saturation magnetization around 1300 emu/cc.

(4) Fe-5d alloy, FePt, was investigated in both nanoparticle and film form. fcc-$Fe_{76}Pt_{24}$ nanoparticles were synthesized by thermal decomposition. TEM image showed the particle size was around 15 nm. From in-plane hysteresis loop, the coercivity of samples was about 150 Oe. The presence of nonzero value for the coercivity suggests that some amount of ordering should be present in fcc-$Fe_{76}Pt_{24}$ nanoparticles. In addition, fcc and $L1_0$-FePt films had been deposited on Pt substrate via a combination of chemical deposition and post-annealing process. Pt-doped Fe films were deposited on Pt substrate using thermal deposition and the as-deposited films were subsequently annealed from 300 ℃ to 800 ℃, FePt films were achieved through diffusion and rearrangement of Fe and Pt atoms in post-annealing process. The transformation from disordering fcc to ordering $L1_0$ phase had been observed from X-ray diffraction results. The $L1_0$-FePt film possessed an out-of-plane anisotropy and a coercivity of 9 kOe after annealing at 600 °C. A further increase in annealing temperature led to lower value of coercivity, probably due to grain growth. In addition, the thickness of Pt-doped Fe films was tunable by adjusting amount of surfactant used. Our SQUID analysis showed that Pt dopant could significantly improve the chemical stability of Fe films in air.

LIST OF PUBLICATIONS

X. L. Hong, Y. Yang, W. Xiao, Y. Yang, J. S. Chen, J. Ding. "A facile chemical solution-based method for epitaxial growth of thick ferrite films", *Advanced Electronic Materials*, 01, 1500102(2015).

X. L. Hong, W. Xiao, N. Bao, W. M. Li, O. Chichvarina, J. Ding. "$L1_0$-FePt films fabricated by wet-chemical route", *Thin Solid Films*, 589, 649(2015).

X. L. Hong, M. Li, N. Bao, E. Peng, W. M. Li, J. M. Xue, J. Ding. "Synthesis of FeCo nanoparticles from FeO(OH) and Co_3O_4 using oleic acid as reduction agent", *Journal of Nanoparticle Research*, 16, 1935(2014).

W. Xiao, X. L. Liu, **X. L. Hong**, Y.Yang, Y.B. Lv, J. Fang, J. Ding. "Magnetic-field-assisted synthesis of magnetite nanoparticles via thermal decomposition and their hyperthermia properties", *CrystEngComm*, 17, 3652(2015).

O. Chichvarina, T. Herng, W. Xiao, **X. L. Hong**, J. Ding. "Magnetic anisotropy modulation of epitaxial Fe3O4 films on MgO substrates", *Journal of Applied Physics*, 117, 17D722(2015).

TABLE OF CONTENTS

LIST OF TABLES

LIST OF FIGURES

Figure 3. 4. (a) Magnetic hysteresis loops of the Fe_3O_4 nanocube (250 nm), nanocuboctahedron (250 nm), and nanooctahedron (80 nm), (b) Zero-field-cooling (ZFC) and field-cooling (FC) curves of the 250 nm Fe_3O_4 nanocubes.

Figure 3. 5. (a) and (b) Fe_3O_4 (001) and (111) surface models, respectively. The corresponding surface magnetic anisotropy $K_S(001)$ and $K_S(111)$ are calculated by aligning magnetic dipole in and out of surface for each model.

Figure 3. 6. (a) Left: schematic diagram of Fe_3O_4 nanocubes coated with chitosan, Right: well-dispersed chitosan-coated nanocubes in water, (b) Dynamic light scattering (DLS) plots of chitosan-coated nanocubes dispersed in water; Red: fresh sample; Blue: sample dispersed in water for a week, (c) Schematic diagram of magnetic hyperthermia measurement system, (d) Hyper-thermia temperature-time dependence curves for Fe_3O_4 nanocubes (blue) and nanocuboctahedrons (red) with equal Fe concentration and deionized water (black).

Figure 4. 1. (a) A schematic diagram of deposition of Fe_3O_4 on Si Substrate, (b) X-ray diffraction θ-2θ scans of Fe_3O_4 film on Si Substrate, (c) The in-plane and out-of-plane hysteresis loops of Fe_3O_4 film, (d) Typical surface AFM image, (e) Cross-section of SEM micrograph of 0.5um Fe_3O_4 film.

Figure 4. 2. (a) X-ray diffraction θ-2θ scan of Fe_3O_4 film on MgO(111), MgO(100) and MgO(110) substrate, (b) X-ray diffraction φ scan of Fe_3O_4 film on MgO(111), MgO(100) and MgO(110) Substrate. Inset shows the rocking curve.

Figure 4. 3. (a) Reciprocal space mapping of the (111) Fe_3O_4 film, (b) Fe 2p

Chapter 1 Introduction

1.1 Magnetic materials

2500 years ago, our ancient ancestors found a type of mineral, magnetite (Fe_3O_4), has magic power of attracting iron. [1] From that moment, the story of magnetism begins. In 1600, William Gilbert published the first scientific study of magnetism in his book. [2] He experimented with lodestones and iron magnets, formed a clear picture of the Earth's magnetic field, and cleared away many superstitions that had clouded the subject. 200 years later, Hans Christian Oersted made great discovery that an electric current can produce a magnetic field and in 1824 year, [3] William Sturgeon invented the first electromagnets in human history, which can produce much more powerful fields than that by lodestones and other magnets. The research on magnetic materials was dated from the invention of the electromagnet. Today, magnetic materials had become one of integral part of modern society and the need for efficient generation of electricity is dependent on the improvement of magnetic materials and design. Besides, there is more and more desire for telecommunication industry to increase the speed for data transmission and decrease the size of devices, both of which can be realized by the development of the magnetic materials. [4]

Magnetic behaviors could be generally classified into five types [5]: Paramagnetic materials, such as aluminum and cooper, have some randomly arranged unpaired electrons and they are weakly attracted by magnets. In

materials that exhibit ferromagnetism, the unpaired electrons are all in parallel via a process known as ferromagnetic coupling. Antiferromagnetic materials have equal number of unpaired electrons line up opposite to one another, and, thus, possess zero net magnetic moment. Ferrimagnetic materials have net magnetic moment as there are more spins held in one direction. Diamagnetism, in which all electron spins are completely paired giving a zero net spin. Diamagnetic materials are weakly repelled by magnet (except in the case of superconductors). (Figure 1. 1) Besides the above 5 types of magnetism, there are two nonlinear magnetism, micromagnetism and spin glasses, which are significant in nanoscle materials. Micromagnetism describes a spin system in which various exchange interactions are mixed. At low temperature, the spin system is frozen with no ordered structure. Such magnetism is observed in Cu-Mn, Ni-Mn alloys. Similar to that of micromagnetism, the random spin arrangement is fixed below certain temperature for spin glasses. However, spin glasses mainly refer to the lower concentration regime. [6] Additionally, Magnetic materials could be divided into soft and hard magnetic materials. [7] If a materials is easily magnetized and demagnetized then it is referred as soft materials, whereas if it is difficult to demagnetized, it is hard (permanent) magnetic materials.

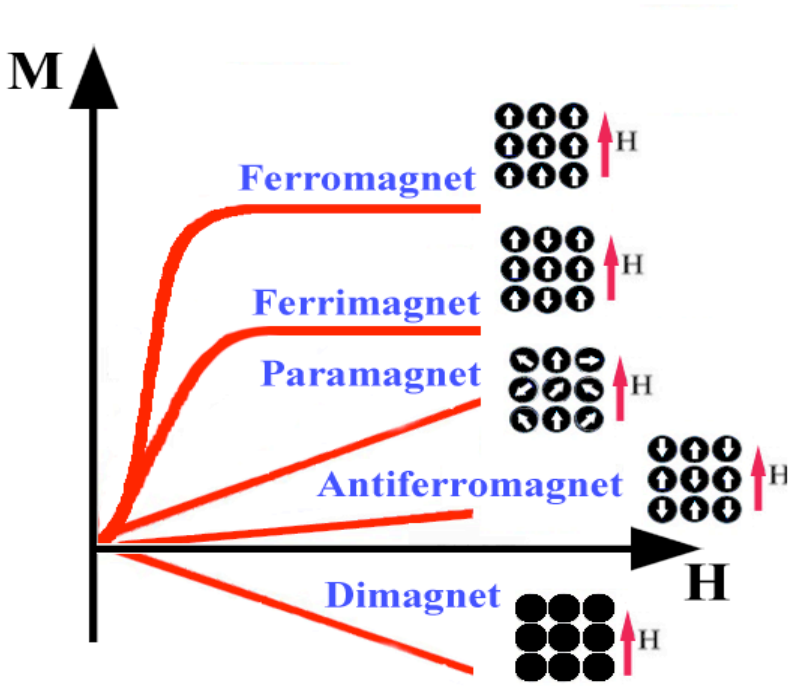

Figure 1. 1. Comparison of magnetic behavior of various kinds of magnetic materials.[8]

Magnetic materials encompass a wide variety of material. One of most studied magnetic materials is Fe-based nanomaterial for their excellent magnetic properties and promising applications, such as spintronics, [9-13] biomedicine [14-19] and high-frequency uses. [20-24]

This chapter presents an in-depth overview of Fe-based nanomaterials, including ferrites and ferrous alloys. The structure and magnetic properties of some specific materials, that are Fe_3O_4, FeCo and FePt, will be studied in detail. The rest of the review is devoted to the applications and growth methods of magnetic Fe-based nanomaterials.

1.2 Different types of Fe-based materials

Among all the metallic materials, iron always has a special place even a prehistoric period is named after it, the Iron Age. From the past to now, Iron has never lost any of its importance and always remains as the most functional material. The reserves of iron is plentiful, it is the forth most abundant element in the earth's crust occurring to the extent of 5.1%. [25] Pure iron is not commonly used commercially because it reacts and rapidly corrodes especially in moist air and elevated temperatures; besides, it is too mechanically soft for many industrial uses. Therefore, a surge in research into various iron-based materials has been observed and continues to expand. The variety of iron-based materials is mainly due to its versatility of iron that no other metal can compare. The origin of iron's versatility is its polymorphism, [26] i.e., on the property that it can be found in different crystal structures. Iron has two crystal structures (Figure 1. 2): the body centered cubic (bcc) and the face-centered cubic (fcc). Pure iron solidifies at 1811K in bcc δ phase and it undergoes first transition to fcc γ –Fe at 1667K. However, the fcc γ –Fe will transforms back to the bcc α-phase when the temperature decreases to 1185K. α-Fe is a soft ductile metal with a density of 7875 $kg.m^{-3}$. In addition α-Fe is a ferromagnetic with a saturation magnetization at room temperature of 220 $A.m^2.kg^{-1}$. Within the α phase a magnetic transition occurs at 1043 K, above which α-Fe will lose its ferromagnetic property and becomes paramagnetic. γ –Fe is nonmagnetic and has lower density (7648 $kg.m^{-3}$). [27] The very different solubility of substitutional and interstitial element in iron provides the possibility of existences of various iron-based materials with different microstructure and structure-related properties, including superconductivity,

ferroelectricity, magnetism, conductivity and catalytic activity, to name a few. The investigation on these application-related unique properties of Fe-based materials is one of the most important issues. Ferrites and ferrous alloys, as two main classes of iron-based materials, have been considered as promising materials because of their technologically significant electronic as well as magnetic properties. Thus, we have mainly focused on the synthesis, properties and applications of ferrites and ferrous alloy such as Fe_3O_4, FeCo and FePt.

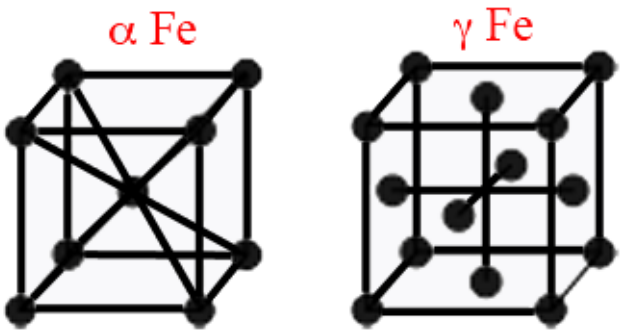

Figure 1. 2. The structure of bcc alpha iron (α) and the fcc gamma iron (γ).[26]

1.2.1 Ferrites

Ferrites are the most common ceramic magnets, black or dark grey in color and very brittle and hard. It is composed of iron oxide (Fe_2O_3) that combined chemically with one or more additional metallic elements. The magnetic properties of ferrites come from interactions between metallic ions occupying particular positions relative to the oxygen ions in the crystal. [28] The most magnetic naturally occurring ferrite minerals on earth are the magnetite

(Fe_3O_4). This material had been known since the ancient time and early navigators found its permanent magnetism and used it as lodestone. [29] The general formula of spinel ferrites is MFe_2O_4, M represents divalent metal ion such as Fe^{2+}, Ni^{2+}, Cu^{2+}, Co^{2+}, Zn^{2+}, Mg^{2+} and the indicated iron is Fe^{3+} trivalent iron ion.

The first reported systematic study on the relation between magnetic properties and the number of binary iron oxides was published by Hilpert in 1909. [30] 19 years later, Forestier in France and Hilpert and Wille in Germany investigated the connections between the chemical composition, the saturation magnetization and the Curie temperature. The most important advances made in ferrites was initiated by Snoek in the Netherlands in 1936, [31] he and his coworkers found that for the material used as inductor core, the most important property is the loss tangent (angle between the capacitor's impedance vector and the negative reactive axis) divided by the permeability (loss factor), thus, Shoek and his team started to develop manganese-zinc-ferrous ferrite which has low loss and high permeability. In the year 1945, Shoek laid the foundation of the physics and technology of practical ferrites and a new industry came into being. [32] After that, the ferrites had been used in many branches of telecommunication and electronic engineering and new applications of ferrite materials continue to be realized, such as in the cellular phone, medical, and automotive markets. More details about the history and development of ferrites could be found in reference [33].

The crystalline arrangement of ferrite is characteristic of a spinel-type structure

(space group Fd3m). [34] In a unit cell of spinel ferrite, there are 32 oxygen, 16 trivalent iron and 8 divalent metal irons. The arrays of 32 oxygen ions arranged in a cubic closed paced (fcc) structure leaving two types of interstices which could be filled by the metal ions. One of the interstices is 64 tetrahedral site A while the other is 32 octahedral site B. The unit cell of the spinel structure is shown in Figure 1. 3. Among all 96 sites; only 24 of them are occupied, that is 64 tetrahedral sites and 32 octahedral sites. If all sites of structure are occupied, the positive charge will be larger than that of negative and the structure cannot keep electrically neutral, therefore, only 24 sites in the two sublattices are occupied to maintain electric neutrality. In the normal spinel structure, the divalent metal ions occupy tetrahedral (A) while the trivalent metal ions occupy octahedral (B) sites. In the inverted spinel structure, the divalent metal ions occupy some octahedral (B) sites while the trivalent metal ions occupy the remaining tetrahedral (A) and octahedral (B) sites. A metallic ion located at A site has four nearest oxygen ion neighbors to form a regular tetrahedron and is said to be in a site of tetrahedral coordination. Similarly, A metallic ion in B site surrounded by six nearest oxygen ion neighbors to form a regular octahedron and metallic ion is in a site of octahedral coordination. The volume of A site is smaller than that of B site while both are smaller than the size of diameter of oxygen ion.

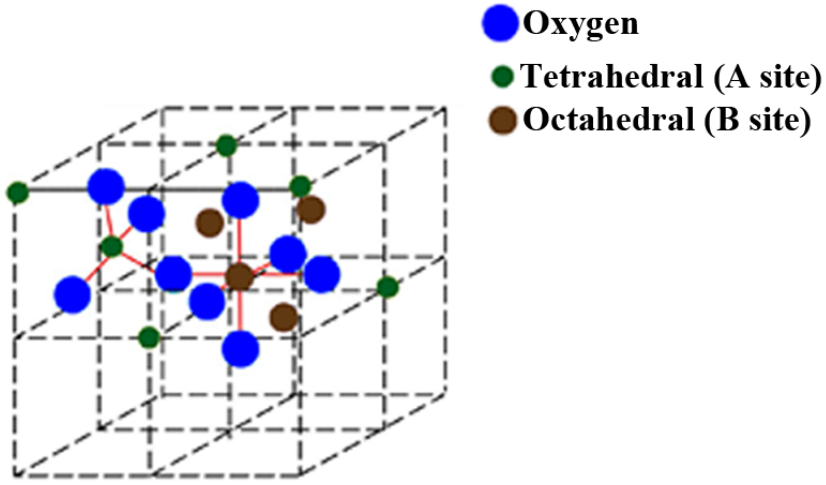

Figure 1. 3. Schematic diagram of the unite cell of spinel structure. [35]

According to the distribution at each site, the spinel ferrites can be roughly classified into those preferring A sites (Mn and Zn) and those preferring B sites (Co, Fe, Ni), [36] the former one is normal spinel structure where the 8 divalent metal ions go into the A sites and the 16 trivalent iron ions occupy the B sites. $ZnFe_2O_4$ is a typical example of ferrite in this configuration and their occupations of the cations may be designated as $(Zn^{2+})[Fe^{3+}Fe^{3+}]O_4$. The later is inverse spinel structure that the divalent ions have a preference for B sites, 8 divalent ions occupy 8 octahedral sites and the 16 Fe^{3+} ions are divided: 8 occupy octahedral sites and another 8 at tetrahedral sites. It is well established that Fe_3O_4 is in inverse spinel structure, its structure could be represented as $(Fe^{3+})[Fe^{2+}Fe^{3+}]O_4$. Besides, some of the ferrites show partial inverted spinel structure where the cations distributed randomly, leading to a state intermediate between the normal and inverse structures. In this case the general formula should be repented by $(M^{2+}_{1-X}Fe^{3+}_X)Fe^{2+}_{2-X}M^{2+}_X O_4$, The X is the

value between 0 and 1 which represents the inversion parameter. It had been reported $MnFe_2O_4$ has partial inverted spinel structure with the precise cation distributions include the notation $(Mn^{2+}_{0.8}Fe^{3+}_{0.2})Fe^{2+}_{1.8}M^{2+}_{0.2}O_4$. [37] What's more, certain amount of the divalent cation could be replaced by another type of divalent metal ions; for example, Zn had been used as substituent in mixed ferrites in many literatures to achieve higher magnetic moment.

Fe_3O_4 (Magnetite) is the one of most fundamental and important member of ferrite. It is widespread natural iron compounds and the most ancient known magnetic substance. Fe_3O_4 in nano-sized had been intensively studied for their applications in ferrofluids, [38-40] recording material, [41-43] cancer treatment [44-46] etc. The significance of magnetite nanoparticles also could be found in the living organisms, for example, magnetotactic bacteria can build highly organized chains of magnetite nanocrystals to generate a permanent dipole in their cells as a tool to sense the Earth's magnetic field for navigation toward favorable habitats. [47]

Fe_3O_4 shows ferrimagnetic behavior ($\mu_{net} = 4\mu_B$) with the inverse spinel structure. Fe^{3+} occupy the A site while equal number of Fe^{2+} and Fe^{3+} irons are placed at B site. For each unit of Fe_3O_4 lattice, there are 32 closely packed O^{2-} ions that embrace 64 tetrahedral and 32 octahedral sites, among them, 1/8 of the A sites and 1/2 of the B sites are occupied. To reflect the structure, the chemical formula sometimes could be reflected as $Fe^{3+}[Fe^{3+}, Fe^{2+}]O_4$. [48] The arrangement of spin is like what is shown in Figure 1. 4.

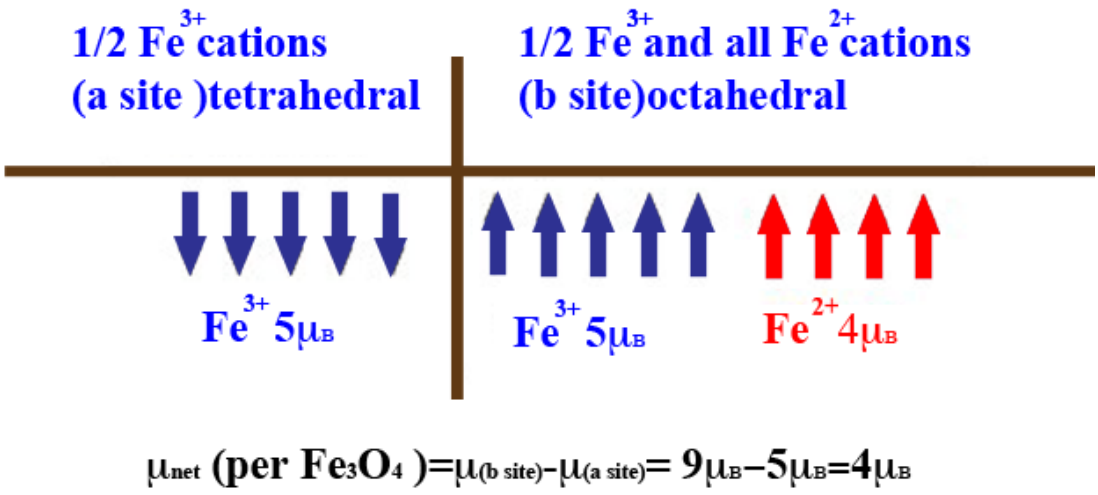

Figure 1. 4. The arrangement of Fe_3O_4 spin.

At around 120K, magnetite experiences the Verwey transition and exhibits a characteristic conductivity jump over 2 orders [49]. In addition, an anomaly in the temperature dependence of the heat capacity is also clearly detected. (Figure. 1.5) The name of Verwey transition is after the person who discovered it in 1939 and the temperature the transition occurred is called Verwey transition temperature (T_V). Similar metal-insulator transition and also found in a number of materials besides magnetite.

At transition temperature, Fe_3O_4 undergoes crystallographic distortion that transforms from cubic ($T > T_V$) to monoclinic ($T < T_V$) symmetry. The change in crystal symmetry and cation ordering result in dramatic difference in electrical and thermal properties as shown in Figure 1. 5. [50, 51] Above Verwey transition, the conductivity of Fe_3O_4 comes from the thermally activated fast electron hopping between Fe^{3+} and Fe^{2+} cations at B-sites of spinel structure. This explanation could be explained by the fact of insulation

of spinel ferrites that only Fe^{3+} cations located at B sites. Around 120K (isotropic point, V_i), the easy directions of magnetization change from the [111] cubic body diagonals to the [001] cube edge directions. In the process of symmetric transformation ($T < T_V$), one of the cube edge orientations becomes the new c-axis and easy magnetic orientation. [52] A drastic change in structure results in a long-range spatial ordering of Fe^{3+} and Fe^{2+} cations, effectively preventing the motion of carriers below T_V. It had been reported that the impurities or nonstoichiometry have a detrimental effect on the Verwey transition temperature. [53-55] In addition, Veywey transition temperature is also affected by presence of defects, structural deficiencies or inhomogeneities. The Verwey transition had been widely applied to identify of magnetite phase in research and natural samples, however the theories of Verwey transition still remain embroiled in controversy.

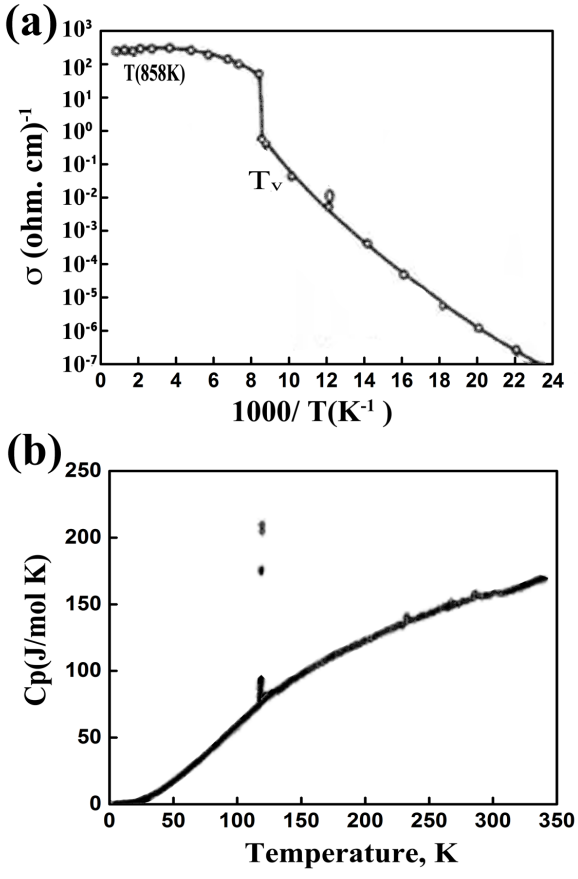

Figure 1. 5. (a) The temperature dependence of electrical conductivity in Fe_3O_4, (b) Anomaly in temperature dependence of heat capacity at T=Tv.[50,51]

1.2.2 Ferrous alloys

A ferrous alloy is a mixture of iron with other elements, which offer improved properties relative to their single-metal counterparts and can be tailored to use for a particular purpose. For example, the presence of different atoms in ferrous alloys can make it tougher when stressed because it is harder for iron layers to slide over each other. The addition of a second more stable metal in iron had been found an effective way to improve corrosion resistance. In addition, the alloy composition could be chosen to optimize one of a number of magnetic properties, including the saturation magnetization, magnetostriction coefficient, and magnetic anisotropy. Figure 1. 6 shows the Slater-Pauling curve [56] that describes the relationship between the magnetic moment and the number of electrons per atom. It can be seen iron has the highest magnetic moment of pure metals and FeCo binary alloy has the highest magnetic moment for all the metals and their alloys.

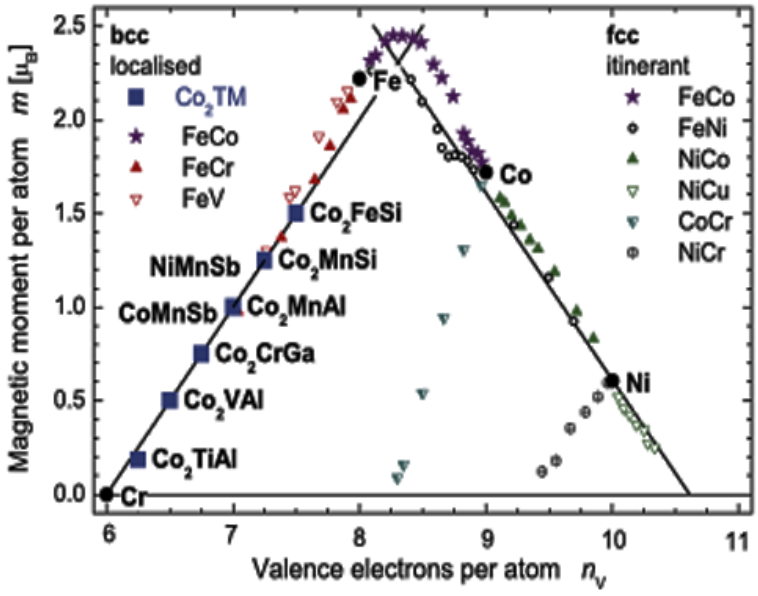

Figure 1. 6. The Slater-Pauling curve.[56]

There are essentially two types of alloys: interstitial alloys and substitutional alloys. In interstitial alloys, small nonmetallic elements like H, C, N, and B are incorporated into the space between the closely packed host metal atoms. Ferrous alloy mainly fall in the category of substitutional alloys, in this class, the atom of the host element (iron) is substituted by another element in the same position. The occurrence of such a substitution depends on the similarities of the properties of the iron and the alloying elements, like crystal and electronic structure, atomic volume. Ferrous alloy have raised considerable interest recently due to their unique properties and applications in biomedicine, magnetic recording, and so on. [57]

FeCo as a typical Fe-3d alloys had attracted much attention due to their exceptional magnetic properties. They have the highest saturation polarization of all known magnetic alloys. It measures 2.35 T. [58] In addition, FeCo

exhibits soft magnetic properties with low coercivity, high permeability, and high Curie temperature. By adjusting the composition and production processes, different properties and magnetization curves of FeCo can be achieved. They are ideal materials suited for applications requiring high flux densities.

The saturation magnetization of FeCo is regarded as independent of its microstructure. As can be seen in Figure 1. 7, [59] the maximum saturation is obtained around 35% cobalt while equiatomic compositions display a considerably larger permeability. Intense research and efforts over the years resulted in great improvements in magnetic properties of FeCo alloy and its relationship with phase transformations. It is commonly believed that Fe–Co alloy experience ordering transition around 730 ℃ that the bcc structure takes the CsCl (B2) ordered structure. [60] There had been many works reported that an increase of saturation has been observed following disorder–order transition, measurements of the saturation moment show an increase of around 4% after ordering [61-63]. The correlation between the structure transition and magnetic moment in turns has been used as an indicator of the order parameter. As for coercivity, FeCo alloys show soft magnetic behavior and its coercivity of the samples sensitively depended on the microstructure, in general, affected by defects, including dislocations, grain boundaries, and precipitates. The coercivity FeCo in the easy axis is on the order of 10 Oe. [64]

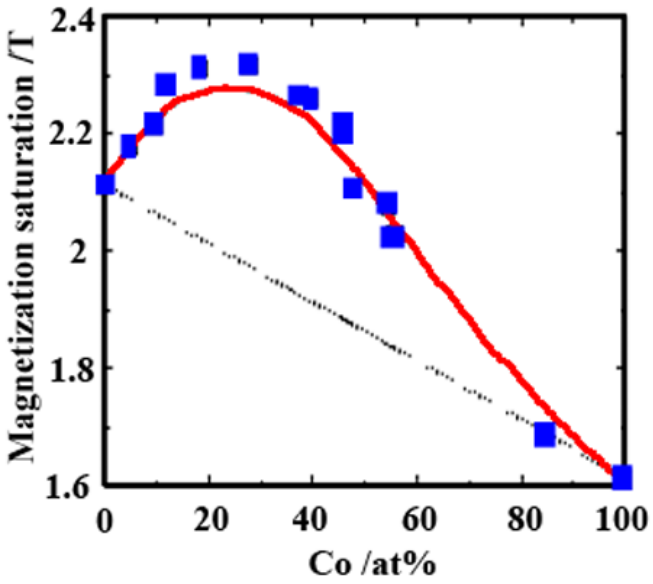

Figure 1. 7. The dependence of maximum saturation of FeCo alloy on Co compositions. [59]

FePt is a ferromagnetic binary Fe-5d alloy known from the past. It is known that the miscibility of two metals in alloy is reduced by lattice distortions originated form atomic sizes difference.[26] Compared with Co (3d metal) as discussed above, the solubility of Pt (5d metal) in iron is lower because its bigger difference in size with iron. There are two different crystal structures of stoichmertic FePt, face center cubic (fcc, A1) phase and $L1_0$ phase. The crystal structure A1 phase and $L1_0$ phase is shown in Figure 1. 8. The crystal structure of A1 phase FePt has a c/a ratio of 1 while $L1_0$ phase has c/a ratio of 0.968. [65] The A1 phase is magnetically soft phase which superparamagnetic behaviors at sub 10 nm scales while $L1_0$ phase shows ferromagnetic behavior due to the huge magnetic anisotropy from the coupling of 3d and 5d electrons. [26] The disordered FePt A1 phase to ordered $L1_0$ phase transited at a specific temperature. It had been reported that the transition temperature and

perpendicular anisotropy of FePt are dependent on the buffer layer and process employed. [66-68]

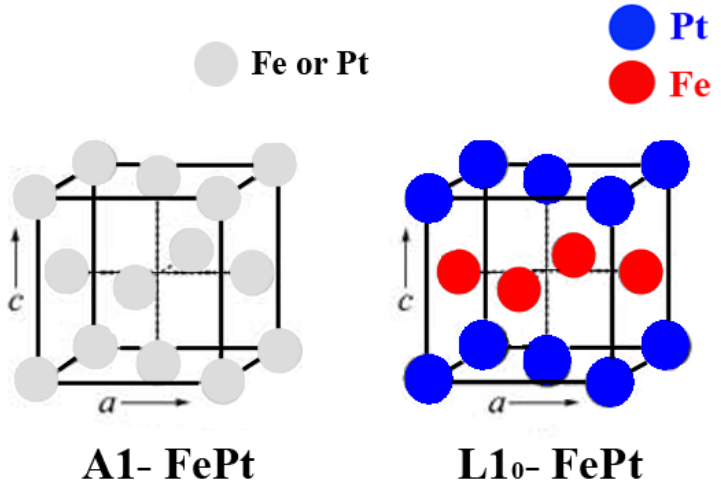

Figure 1. 8. The crystal structure of disordered (A1) and ordered ($L1_0$) FePt phase.

The ordered $L1_0$-FePt alloys possess very excellent hard magnetic properties with the saturation magnetization 1.4T, Currie temperature of 750 K, coercivity Hc = 1–10 kOe and the magnetocrystalline anisotropy 7.0×10^7 erg/cm^3. [69, 70] In addition, due to the Pt content, FePt alloy shows very good corrosive and wear resistance when compared with Fe metal. Recently, $L1_0$-FePt has received much attention due to its extremely high-magnetic-anisotropy energy, which meet the demands of applications in information technologies. For magnetic recording, as the recording bit is down to 10 nm scale, the recording bit might flip itself and result in recording data unstable because of thermal agitation. As a solution, ordered $L1_0$-FePt material with high Ku (magnetic anisotropy constant) value can effectively stabilize the spin state against thermal agitation. According to the report of Weller in 2000, [71] the high magnetic anisotropy energy of ordered $L1_0$-FePt allows for thermally

stable grain size down to 3 nm, therefore, realizing a magnetic medium capable of recording densities of the order of 1 Tb/in^{-2}. Other applications of $L1_0$-FePt material are permanent magnet or bias layer for spin electronic devices.

1.3 Applications

1.3.1 Overview

Till now, magnetic Fe-based nanomaterials had found its applications in wide range of fields. Bimetallic ferrous alloy FeX (X= Mn, Co, Ni, Zn, Pt, etc) with various magnetic properties had been studied for the use in data storage, medicinal imaging, magnetic ampllifiers, chemical sensing, magnetic resonance imaging contrast agents, targeted drug delivery carriers and so on. [72-74] Similarly, Magnetic Ferrites, MFe_2O_4 (M = Fe, Mn, Cu, Zn, Ni, Co, Mg, etc.), had been used in almost all fields by virtue of their interesting electrical and magnetic properties. They are used in transformer cores, antenna rods, memory chips, high density magnetic recording media, permanent magnets, transducers, activators microwave and computer technology and so on. [75, 76]Additionally, The nanocrystalline ferrites had been studied for use in new fields like magnetically guided drug delivery, magnetic resonance imaging (MRI), catalyst, humidity and gas sensors, magnetic fluids etc. [77, 78]

To further understand the applications of magnetic Fe-based nanomaterial, we will present a detail study of their two most important uses: biomedicine and microwave applications.

1.3.2 Biomedicine application

The biomedical application of magnetic Fe-based materials, mainly ferrous alloy and ferrites nanoparticles, could be classified in terms of the application inside (in vivo) or outside (in vitro) the body. The vivo applications could be further grouped in therapeutic (hyperthermia and drug delivery) and diagnostic like magnetic resonance imaging (MRI). For vitro applications, the main use of magnetic nanoparticles is in diagnostic (separation/selection).[79]

Magnetic nanoparticles have been regarded as an effective carrier to deliver anti-cancer drugs to the designated location such as cancerous tissues. The external magnetic field allow the drugs that are entrapped, attached, adsorbed, or encapsulated into or onto MNPs to the desired target area, fix them at the local site while the medication is released and act locally. Magnetic ferrite (Fe_3O_4) has been used to guide radionuclides to vivo liver tissue in rats. [80] Therapeutic applications are feasible by further conjugation with other medicals.

The ferrites, FeCo, FePt and other Fe-based nanomaterials with high imaging contrast effects now had been used for diagnosis of cancer in different organs such as the liver, brain, spine and musculoskeletal systems. For example, FeCo nanoparticles had been reported with ultra-high R1 and R2 relativities. (The definition of R1 and R2 is given by the relation rate of solution with and without contrast agent) Mesenchyme stem cells are able to internalize these nanoparticles, showing high T2-contrast enhancement (T2 transverse relaxation time is used to quantify the rate of the decay of the magnetization

ithin the xy plane.) in MRI and long-lasting T1-contrast enhancement for vascular MRI in rabbits was also achieved. (Spin-lattice relaxation T1 and spin-spin relaxation T2 describe the gain and loss of magnetization in the z-direction and x,y-direction respectively) [81]

Hyperthermia is a therapeutic procedure that is based on the fact that the cancer and healthy cells show signs of apoptosis at temperatures above 41–42˚C. [82–84] Thermal energy from hysteresis loss of magnetic nanoparticles by Neel and Brownian relaxation can be used in hyperthermia. As shown in Figure 1. 9, [85] The Brownian relaxation the of the nanoparticle rotates because of the magnetic torque arising from the misalignment of external field and magnetic moment, the orientation of magnetic moment is fixed with respective to the field. On the other hand, in Néel relaxation, magnetic moment rotates when the nanoparticle is stationary. Several ferrites MFe_2O_4 (M = Fe, Mn, Zn, Co, etc.) as well as ferrous alloys (FeCo, FeNi) nanoparticles had been investigated for use for hyperthermia.

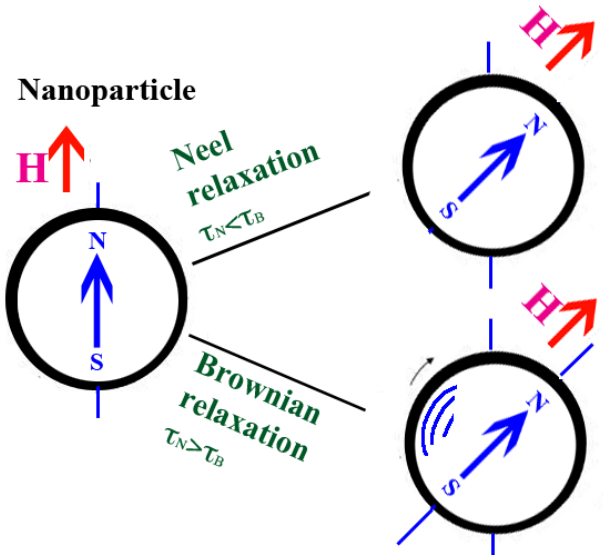

Figure 1. 9. Illustration of Néel and Brownian relaxation of magnetic material. [85]

1.3.3 Microwave application

With the developments of electronic, telecommunication and radar technologies, magnetic materials for high-frequency applications are growing importance. For high-frequency applications, ferrite components are extensively employed for their high specific resistance, remarkable flexibility in tailoring the magnetic properties and ease of preparation. [86] Although metallic ferrous alloys with very thin laminations offer the benefit of higher polarization, they can only be applied in the low frequencies range where the losses caused by the skin effect are not too severe. [87] Thus, to allow the total penetration of electromagnetic fields, ferrites as nonconductive oxides usually are chosen for use in high-frequency applications such as telecommunications and radar systems. Microwave technology requires frequencies and bandwidths up to 100 GHz, at such high frequency, the traditional way of transmit electrical energy can not work because the electric energy is radiated (power loss) via electromagnetic wave. At high frequency, the domain walls are unable to follow the fields and absorption of microwave power takes place by spin dynamics. The frequency dependent permeability is crucial for the microwave performance. The permeability μ is a complex parameter that is composed by a real part and imaginary part. It is given as: [88]

$$\mu = \mu_0 \mu_r = \mu_0 (\mu_r' - \mu_r'') \quad (1.1)$$

Where μ_0 equal to the permeability of free space and the μ_r relative permeability, μ_r' and μ_r'' are the real part and imaginary part. For most metals used as conductors for microwave applications, the relative permeability μ_r

=1. The typical permeability spectrum of ferromagnetic material is shown below (Figure 1. 10 [89])

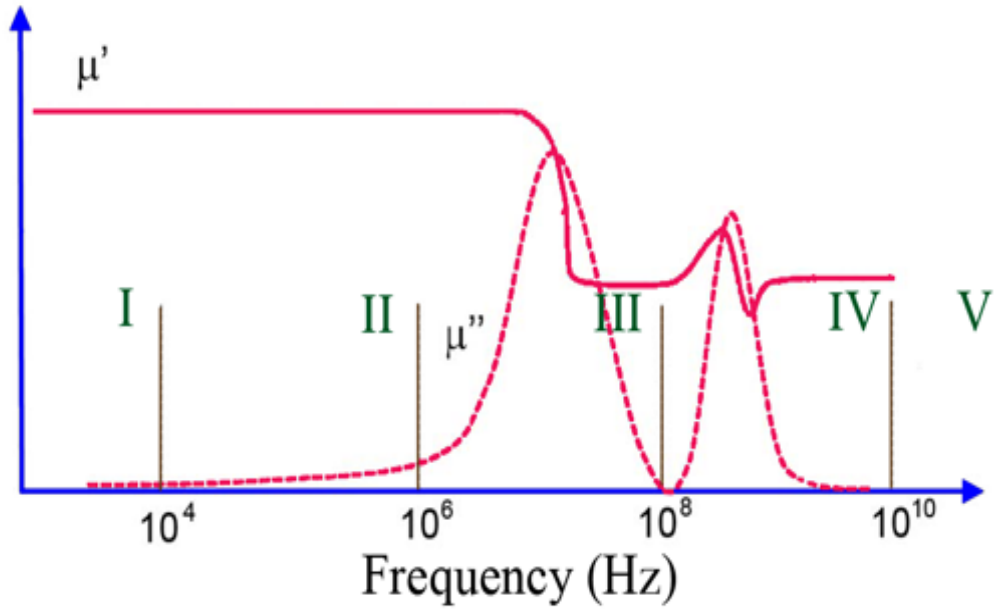

Figure 1. 10 Illustration of Frequency dependent permeability spectrum of ferromagnetic material. Note that the eddy current loss is neglected. [89]

The spectrum of the ferromagnetic materials is divided into 5 regions. In the I region, where frequency <10^4 Hz (low frequency band), μ_r' is constant and μ_r'' almost zero. II region is the band in the frequency between 10^4-10^6 Hz, in this mid frequency band, the magnetic internal friction peak; dimensional resonance and magnetomechanical-coupled resonance are possible to be observed from the pattern. [89] At the region of higher frequency (10^6-10^8 Hz), domain wall resonance and relaxation dominate. The microwave band is in the range from 10^8-10^{10} Hz, natural resonance dominates and resonant peak can be found in μ_r'' curve. When the frequency above 10^{10} Hz, the main contributor is the internal exchange field. For our study, we focus on the microwave

frequency band IV, where the nature resonance is the main contributor. The resonance frequency of materials is of great significance as it indicates the upper limit of working frequency. If the frequency over the resonance frequency, the material will become useless as the relative permeability drops rapidly.

In practical use of ferrites for microwave applications, the most frequent use is usually from 3GHz to 30GHz. [90] The loss of absorption of microwaves energy by ferrites involves with defects and the anisotropy field distribution as well as the electrical conduction. At high frequencies, the dominant cause of energy loss is the electrical conduction, thus, the resistivity of the ferrites should be given the first consideration.

1.4 Motivations and objectives

As mentioned before, the active search for Fe-based nanomaterials that benefit for different applications is under way. The hot issues and challenges in this research community include:

(1) The nano-scale particles with high saturation magnetization are expected to be superior, as they are favored for the application in biomedicine, like, hyperthermia and magnetic resonance imaging (MRI) medium agent. Therefore, metal oxides and transition metals with high saturation magnetization have been the focus of recent fundamental and technological studies. For example, Fe_3O_4 nanoparticles have been used for biomedicine over 40 years as it has very good compatibility and ease to functionalize. [90] In addition, the FeCo alloy nanoparticles were of

interest for their highest saturation magnetization under ambient conditions. However, some synthesis protocols reported for ferrous alloys nanoparticles fabrication involved either an expensive, toxic and explosive iron organometallic compound or under a highly reducing protection environment such as H_2 or using a toxic reducing agent. Therefore, it is crucial for exploring of a safe and clean method.

(2) It is well known that the morphology of nanoparticles is very crucial for their performance in different applications. In this way, a lot of study had been focus on the effects of surfactants, reducing agents and temperature on morphology and properties of nanoparticles. However, the effect of external magnetic field on shapes and properties of nanoparticles has not been widely investigated. The advantage of controlling magnetic nanoparticle growth with external magnetic field is that there is no chemical contamination and it can induce magnetic anisotropy to the synthesized nanoparticles. Thus, it is meaningful to investigate the influences of external magnetic field on the morphology and properties of magnetic nanoparticles.

(3) A lot of iron-based spinel oxides appear as versatile because of their complex structure. This versatile material could be used as spintronics as a conductive electrode in magnetic tunnel junctions or as a spin-filtering insulating barrier in spin-filter. Some magnetic oxides like EuO had been studied for use in insulating barriers in spin filters devices, however, because of the low Tc of the material, the working temperature is only as

low as several kelvins. Thus, the spinel ferrite is a promising candidate. Though some spinel ferrites such as $NiFe_2O_4$, $CoFe_2O_4$ had been studied to use for magnetic insulating barriers in spin filters devices, [92] the studies have not been very intensive. There are still much remains to be explored concerning their properties and potential applications.

(4) Furthermore, till now, most film growth techniques used for deposition of ferrite and ferrous alloy films are physical and chemical vapor deposition. It had been reported that physical and chemical vapor deposition could deposit high-quality and epitaxial ferrite films. However, as vacuum is frequently required, their high cost limits their application. In addition, these techniques are limited to the fabrication of thicker magnetic films in order of submicron and micron meter. Thus, solution-based film deposition methods had been used for growth of films with comparable quality. It had been studied that within reasonable control, solution-based methods can produce films with good structure and quality of epitaxy. [93] However, most ferrite films fabricated by solution-based methods have rough surface and weak adhesion, restricting them to achieve full industrial potential. Most importantly, a general and facile method for broadly deposition of different ferrites has not been demonstrated, which inspires the continuous and systematic exploration.

The overall purpose of this project was to develop the fabrication method and investigate the properties of ferrites and ferrous alloy such as Fe_3O_4, FeCo and FePt in both the nanoparticle and film forms, as well as explore some

promising uses of magnetic Fe-based nanomaterial for biomedicine, power and other applications.

The specific objectives were

(1) A systematic study on synthesis of magnetic ferrites materials via thermal decomposition technique. Fe_3O_4 nanoparticle and films as the typical ferrites was investigated as the starting work in Chapter 3 and 4. Specifically, the microstructure and fundamental properties of Fe_3O_4 nanoparticle prepared by thermal decomposition were explored by introduction of external magnetic field and change of preparation conditions, such as, reaction temperature, holding time and so on. Most importantly, in order to overcome the limitation of traditional solution-based deposition methods, we developed a universal and facile wet chemical strategy to deposit thick epitaxial Fe_3O_4 and (Co, Ni, Mn and Zn) ferrites with excellent surface and interface morphology.

(2) Besides ferrites, ferrous alloys as another important class of Fe-based nanomaterial were investigated in later part of work. Typical Fe-3d ferrous alloy, FeCo nanoparticle was fabricated through a safe and clean fabrication process and this process was proven also capable to produce Fe_3O_4 and Co nanoparticles. In addition. The facile wet chemical method developed for deposition of ferrites in earlier work was extended to fabricate FeCo film. A further study on ferrous alloys was focused on the typical Fe-5d alloy, FePt. Similar to that of FeCo,

FePt nanoparticles and films were synthesized via chemical route. In Chapter 5 and 6, we gained a deep understanding of the relation between the growth condition, compositions, microstructure and the magnetic properties of FeCo and FePt alloys.

(3) An exploratory study on potential applications of as-synthesized Fe-based nanoparticles and films. This study focuses on biomedicine applications for Fe-based nanoparticles. In particular, the influence of magnetic-field-induced shape change on hyperthermia properties of Fe_3O_4 nanoparticles and the biocompatibility of monodispersed FeCo nanoparticles were investigated. Moreover, epitaxial thick Fe_3O_4 films were studied for their high frequency and power applications. $L1_0$-FePt film, with the tailored magnetic properties, showed promising use for data storage.

REFERENCES:

[1] J. Garcia, G. Subias, J. Phys.: Condens. Matter. **2004**, 16, 145.

[2] M. D. Opdyke, E.T. Channell, Magnetic Stratigraphy, Channell Academic Press, USA **1996**.

[3] W. S. Michael, Groundbreaking Scientific Experiments, Inventions, and Discoveries of the 19th Century, Greenwood Publishing Group, USA **2003**.

[4] W. Gao, N. M. Sammes, An Introduction to Electronic and Ionic Materials, world scientific publishing co.pte.ltd, USA **1999**.

[5] A. Goldman, Handbook of Modern Ferromagnetic Materials, Springer Science & Business Medi Germany, **1999**.

[6] S. Chikazumi, Physics of Ferromagnetism, Clarendon Press, UK, **1997**.

[7] D. S. Mathew, R. S. Juang, Chem. Eng. J. **2007**,129,51.

[8] R. D. Rawlings, Materials Science and Engineering Vol 2, Materials Science and Engineering Vol 2, Eolls publications, Abu Dhabi, **2009**.

[9] Y. X. Lu, J. S. Claydon, E. Ahmad, Y. B. Xu, M. Ali, B. J. Hickey, S. M. Thompson, J. A. D. Matthew and K. Wilson, J. Appl. Phys. **2005**, 97, 10C313.

[10] G. Hu, Y. Suzuki, Phys. Rev. Lett. **2002**, 89, 276601.

[11] L. B. Zhao, W. B. Mi, E. Y. Jiang H. L. Bai, Appl. Phys. Lett. **2007**, 91, 052113.

[12] D. Tripathy, A. O. Adeyeye, S. Shannigrahi , Phys. Rev. B **2007**, 7, 012403.

[13] P. Ruden, Nat Mater. **2011**, 10, 8.

[14] I. Sharifi, H. Shokrollahi, S. Amiri, J. Magn. Magn. Mater. **2012**, 324, 903.

[15] A. Jordan, R. Scholz, P. Wust, H. Schirra, S. Thomas, H. Schmidt, R. Felix, J. Magn. Magn. Mater. **1999**, 194, 185.

[16] L. Zhang, H. Gu, X. Wang, Magn. Magn. Mater. **2007**, 311, 228.

[17] H. Hermawan, H, Alamdari, D. Mantovani, D. Dubé. Powder Metall. **2008**, 51, 38.

[18] S. Rana, A. Gallo, R.S. Srivastava, R.D.K. Misr, Acta Biomater. **2007**, 3, 233.

[19] N. Sanpo, C. C. Berndt, C. Wen, J. Wang, Acta Biomater. **2012**, 9, 5830.

[20] A.K. Subramani, K. Kondo, M. Tada, M. Abe, M. Yoshimura, N. Mater Chem Phys, **2010**, 123, 16.

[21] F. G. Brockman, IEEE, Electrical Eng. **1949**, 68, 1077.

[22] K. Praveena, K. Sadhana, S. Bharadwaj, S.R. Murthy, J. Magn. Magn. Mater. **2009**, 321, 2433.

[23] B. K. Kuanr, V. Veerakumar, A.V. Kuanr, K. Lingam, S. R. Mishra, R. E. Camley, Z. Celinski, J. Appl. Phys. **2012**, 111, 07B542.

[24] R.Valenzuel, Physics Research International. **2012**, 2012, 591839.

[25] D. Nicholls, The Chemistry of Iron, Cobalt and Nickel Comprehensive Inorganic Chemistry, Oxford, Eng. : Pergamon, UK **1973**.

[26] W. Pepperhoff, M. Acet, Constitution and Magnetism of Iron and its Alloys, Springer Science & Business Media, USA **2001**.

[27] A. K. Arora, Ritu, Research Journal of Chemical Sciences, **2013**, 3, 18.

[28] François Cardarelli, Materials handbook, Springer Science & Business Media, Germany **2008**.

[29] J. Stöhr, H. C. Siegmann, From Fundamentals to Nanoscale Dynamics, Springer-Verlag Berlin Heidelberg, USA **2006**.

[30] K. Hilpert, Chemistry of inorganic vapors, Springer-Verlag Berlin Heidelberg, USA **1990**.

[31] E.C. Snelling, Soft ferrites properties and applciations, buttworth and co. ltd., London, **1988**.

[32] J. G. Koh, J Korean Phys Soc, **2004**, 44, 1504.

[33] A. Goldman, Modern ferrite technology, Van Nostarand Reinhold, New York **1990**.

[34] A. Tiwari, A. Tiwar, Bioengineered Nanomaterials, CRC Press, USA **2013**.

[35] S. Noppakun, Solution Precursor Plasma Spray System, Springer International Publishing, USA **2014**.

[36] G. Alexander, Superconductors - New Developments, InTech, Croatia, **2015**.

[37] D. Carta, M. F. Casula, G. Mountjoy, A. Corrias, Phys Chem Chem Phys. **2008**, 10, 3108

[38] R.Y. Hong, T.T. Pan, Y.P. Han, H.Z. Lib, J. Ding, Sijin Han, J. Magn. Magn. Mater. **2007**, 310, 37.

[39] E. G. R. Putra, B. S. Seong, E. Shin, A. Ikram, S. A. Ani, Darminto, J Phys: Conference Series **2010**, 247, 012028.

[40] N. D. Kandpal, N. Sah, R. Loshali, R. Joshi, J. Prasad, K. Pandey, S. Sharma, Particul Sci Technol, **2013**, 31, 474.

[41] P. Raveendran, J. Fu, S.L. Wallen, J. Am. Chem. Soc. **2003**, 125, 13940.

[42] L.Y. Zhang, Y.F. Zhang, J. Magn. Magn. Mater. **2009**, 321, L15.

[43] A. Homola, M. Lorenz, C. Mastrangelo, T. Tilbury, IEEE Trans. Magn. **2003**, 22, 716.

[44]O. D. Jayakumar, R. Ganguly, A. K. Tyagi, D. K. Chandrasekharan, C. K. Nair CK. J Nanosci Nanotechnol. **2009**, 9, 6344.

[45] G. Yuan, Y. J. Yuan, K. Xu, Q. Luo, Int J Mol Sci. **2014,** 15, 18776.

[46] J. D. Meyers, T. Doane, C. Burda, J. P. Basilion, Nanomedicine, **2013**, 8, 123.

[47] M. Chariaou, L. R. Lee, J. Kind, I. G. Rubio, A. Komeili, A. U. Gehrin, Biophys. J. **201**5, 108, 1268

[48] F. Walz, J. Phys.: Condens. **2002**, 14, R285.

[49] M. Izumi, T. F. Koetzle, G. Shirane, S. Chikazumi, M. Matsui, S. Todo , Acta Crystallogr. Sect. B: Struc. Sci., **1982**, 38, 2121.

[50] P. A. Miles, W. B. Westphal, V. A. Hippel, Rev. Mod. Phys, **1957**, 29, 279.

[51]J.P, Shepherd, J. W. Koenitzer, R. Aragon, C. J. sandberg, J. M. Homig, Rev. Mod. Phys, **1985**, 31, 1107.

[52] E.J.W. verwey, Nature **1939**, 144, 327.

[53] R. Arag´on, D. J. Buttrey, J. P. Shepherd, J. M. Honig, Phys. Rev. B **198**5, 31, 430.

[54] R. Arag´on, R. J. Rasmussen, J. P. Shepherd, J. W. Koenitzer, J. M. Honig, J. Magn. Magn. Mater. **1985**, 54, 1335.

[55] J. P. Shepherd, J. W. Koenitzer, R. Arag´on, J. Spalek, J. M. Honig. Phys. Rev. B, **1991**, 43, 8461.

[56] F. Claudia, F, Gerhard H, Spintronics, From Materials to Devices, Springer Netherlands, USA **2013**.

[57] G. Schmid, Nanoparticles: From Theory to Application, Wiley-VCH Verlag GmbH & Co. KGaA, Germany, **2004**.

[58] J. E. Goldman, R. Smoluchowski, Phys. Rev. **1949**, 75, 310.

[59] C. Kuhrt, L. Schultz, J. Appl. Phys.**1993**, 73, 6588.

[60] T, Sourmail, Prog Mater Sci. **2005**, 50, 816.

[61] C. W. Chen, J. Appl. Phys. **1961**, 32, 348S.

[62] D. W. Clegg, R. A. Buckley, Metal Sci. J. **1973**, 7, 48.

[63] J. E. Goldman, R. Smoluchowski, Phys. Rev.**1949**, 75, 310.

[64] Severino P. C. Marques, Briefs in Applied Sciences and Technology, Springer, Germany, **2012**.

[65] S.V. Halilov, R. Feder, Solid State Commun. **1993**, 88, 749.

[66] L.J. Qiu, J. Ding, A.O. Adeyeye , J. H Yin, J. S. Chen, S. Goolaup, N. Singh, *IEEE Trans Magn*. **2007**, **43,** 2157.

[67] H. Yun, J.W. Cai, Appl Phys Lett. **2005**, 87, 032504.

[68] S.C. Chen, P.C. Kuo, S.T. Kuo, A.C. Sun, C.T. Lie, C. Y. Chou, *Mater Sci Eng.* **2003**, **B98,** 244.

[69] B. D. Terris, D. Weller, L. Folks, J.E.E. Baglin, A .J. Kellock, H. Rothuizen, P. Vettiger, J Appl Phys. **2000**, 87, 7004.

[70] T. Hasegawa, W. Pei, T. Wang, Y. Fu, T. Washiya, H. Saito, S. Ishio, Acta Mater **2008**, 56, 1564.

[71] D. Weller, H. Brandle, G. Gorman, C. J. Lin, H. Notrays, Appl. Phys. Lett. **1992**, 62, 2726.

[72] X. Sun, Y. Huang, D. E Nikles. Int J Nanotechnol, **2004**, 1, 328.

[73] T. Adisorn, Applications of Nanomaterials in Sensors and Diagnostics, Springer, Germany, **2013**.

[74] J. R. Davis, Nickel, Cobalt, and Their Alloys, ASM International, **USA**, 2000.

[75] A. Verma, T.C. Goel, R.G. Mendiratta, R.G. Gupta, J. Magn. Magn. Mater. **1999**, 192, 271.

[76] H. Waqus, A.H. Quresghi, J. ThermAnaly. Calori. **2009**, 98, 355.

[77] N. Rezlescu, E, Rezlescu, F. Tudorach, P.D. Popa, J. Opt. Adv. Mater. **2004**, 6, 695.

[78] X. Chu, B. Cheng, J. Hu, H. Qin, M. Jiang, Sensors. Actuat. B **2008**,129, 53.

[79] A. Akbarzadeh, M. Samiei, S. Davaran, Nanoscale Res Lett. **2012**, 7, 144.

[80] C. M. Fu, Y. F. Wang, Y. F. Guo, T. Y. Lin, J. S. Chiu, IEEE Trans. Magn. **2005**, 41, 4120.

[81] W. S. Seo, J. H. Lee, X. M. Sun, Y. Y. Suzuki, D. Mann, Z. Liu, M. Terashima, P. C. Yang, M. V. McConnell, D. G. Nishimura, H. J. Dai, Nat Mater. **2006**, 5, 971.

[82] B. Hildebrandt, P. Wust, O. Ahlers, **2002**, 43, 33.

[83] W. Andra, C.G. Ambly, R. Hergt, J. Magn. Magn. Mater. **1999**, 194, 197.

[84] A. Jordan, R. Scholz, P. Wust, J. Magn. Magn. Mater. **1999**, 201, 413.

[85] B. J. Jeyadevan, Ceram. Soc. Jpn. **2010**, 118, 391.

[86] Z.W. Li, Z.H. Yang, L.B. Kong, Procedia Eng. **2014**, 75, 19.

[87] A. I. Spitsyn, Tech Phys. 2005, 50, 1166.

[88] V. K. Varadan, Microwave Electronics: Measurement and Materials Characterization, Wiley, USA, **2004**.

[89] L. B. Kong, Int. Mater. Rev. **2013**, 58, 203.

[90] M, P, Horvath, J. Magn. Magn. Mater. **2000**, 205, 171.

[91] J. W. Gunn, The Preparation and Characterization of Superparamagnetic Nanoparticles for Biomedical Imaging and Therapeutic Application, ProQuest, USA **2008**.

[92] N. M. Caffrey, D. Fritsch, T. Archer, S. Sanvito, C. Ederer, Phys. Rev. B **2013**, 87, 024419.

[93] L. Fei, M. Naeemi1, G. F. Zou, H. M. Luo, The Chemical Record. **2012**, 13, 85.

Chapter 2 Characterization Techniques

2.1 Structural characterization

In my thesis, a series of characterization had been used for studying properties of as-synthesized samples. Crystallographic structure was studied by X-ray diffraction (XRD) and surface chemical analysis was studied by X-ray Photoelectron Spectroscopy (XPS). Scanning electron microscopy (SEM) and transmission electron microscopy (TEM) were employed for observation of morphology and analysis of microstructure. Energy-dispersive X-ray spectrometer (EDS) was applied for analysis of elements while atomic force microscopy (AFM) for the study of surface topography. The thickness of film was detected by Profilometer. The magnetic properties were studied by vibrating sample magnetometer (VSM) and superconducting quantum interference device (SQUID). The electric properties were studied by Physical Property Measurement System (PPMS). The microwave properties were studied in an APC7 coaxial line mode at room temperature with an Agilent PNA E8363B network analyzer. The magnetic hyperthermia properties of magnetic nanostructures were characterized by a heat induction machine. The fundamental principles and details are described in this chapter.

2.1.1 X-ray diffraction (XRD)

X-ray diffraction (XRD) is the most used techniques for study of crystallographic structure in research. It is a kind of non-destructive analytical technique that is widely used for identify crystalline phase, calculate lattice constants and grain size as well as check the preferred orientation, etc. [1]

The technique of XRD is based on the elastic scattering between the X-rays and a crystalline sample. When the X-ray beams hit an atom, the electrons of atoms absorb the energy and oscillate around their position with the exact same frequency with that of incoming bean. After that, the oscillating electron reradiates X-rays with particular frequency. However in the crystalline structure, the atoms all aligned in an organized order and the scattered X-rays interact constructively in different directions, which result in diffraction pattern on a detector. Brag diffraction was first proposed in 1913 by physicists William Lawrence Bragg and William Henry Bragg that clearly explain the phenomenon of reflection of X-ray of cleavage faces of crystals at certain specific wavelengths and incident angles. [2] The Fundamental principle of XRD is based on Bragg's law as shown in Figure 2.1.

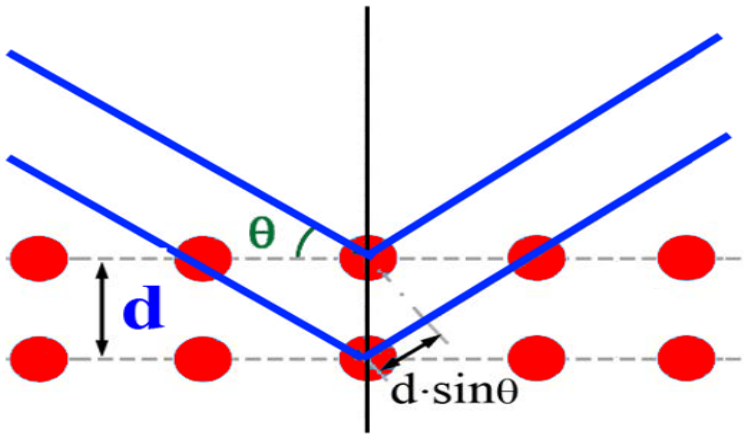

Figure 2. 1. Schematic illustration of Bragg's law.[1]

The crystal is a set of parallel planes with certain distance in bragg's model. The constructive interference occurs when the phase shift is a multiple of 2π. Thus, diffraction occurs if the equation of Bragg's Law is satisfied:

$$2d\sin\theta = n\lambda \qquad (2.\ 1)$$

Where n is an integer corresponding to the order of diffraction, λ is the wavelength of incident X-ray, d is the inter-planar spacing of reflecting planes and θ is the angle of the incidence relative to the reflecting planes.

In our study, a Bruker D8 ADVANCE XRD system with monochromatic and Cu Kα radiation (λ = 1.54056 Å) was used for phase characterization. Crystallographic information was collected using the standard θ-2θ scan. The sample in the test is rotated by the angle of θ while the detector is rotated by 2θ. The phase of material was compared and identified with that of standard database (Joint Committee on Powdered Diffraction Standard (JCPDS)).

In addition, the quality of film texture was studied by the full width at the half maximum (FWHM) of rocking curve, which is conducted by θ scanning at a fixed 2θ angle. Glancing angle scan (GAXRD) is a method that can render the XRD measurement more sensitive to the near surface region of the sample and minimize the substrate contribution on the diffraction response. GAXRD is performed with a parallel monochromatic X-ray beam falls on the sample surface at a fixed low glancing angle so that only few tens of nanometer under the film surface could be detected. In addition, φ-scan tested by Bruker D8 Discover system was used to study the film in-plane alignment.

2.1.2 Scanning electron microscopy (SEM)

The scanning electron microscopy (SEM) is a type of electron microscope that is used to observe the surface of sample through scanning with electron beam in a raster scan pattern. [3] The atoms of observed sample are interacted with the electrons that generate signals containing the surface topography information. The illustration of a typical SEM is shown in Figure 2. 2.

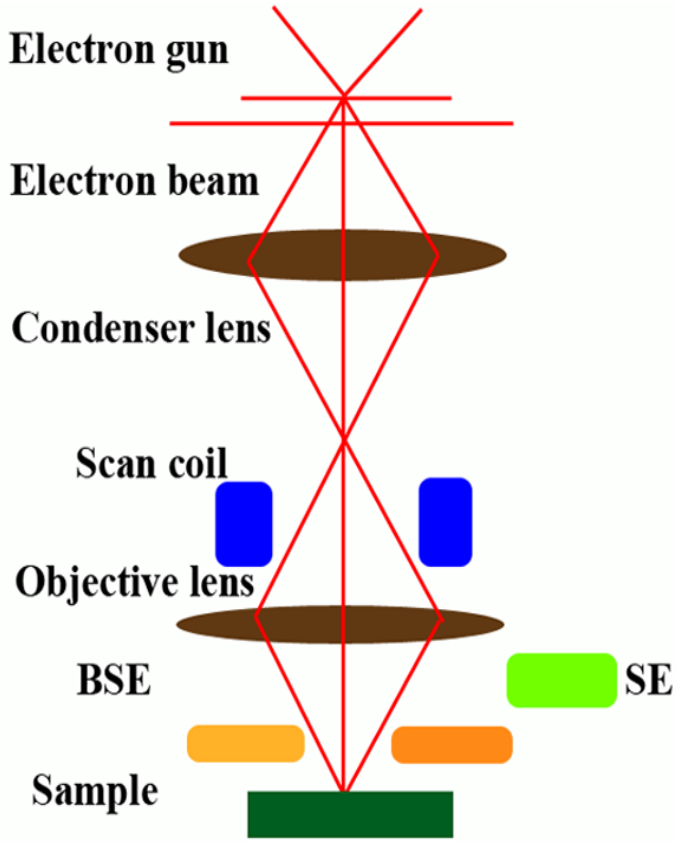

Figure 2. 2. Schematic illustration of SEM.[3]

The electrons are emitted from an electron gun fitted with a cathode and accelerated towards an anode by certain potential. The electron beam with the energy in the range from few hundreds eV to 50 keV is focused to a very fine spot size of 0.4 to 5 nm by condenser lens and objective lens. After that, the

electron beam goes through scanning coil and start scanning the surface of the sample in a raster mode. The atoms of sample interacted with incoming electron beam and eject secondary electrons, backscattered electrons, primary electrons and characteristic X-rays. The ejected electrons are transferred to signals and collected by detected. These signals are displayed as variations in brightness on a monitor after amplified by electronic amplifiers. The pixel that is shown on pc screen is exactly corresponding to the position on the sample. Different signals have different functions; secondary electrons are usually used to observe morphology while back-scattered electrons, reflected from the sample by elastic scattering, can be used to obtain the information like, elements distribution, contrasts of composition in samples with more than one phase. In this thesis, a SEM system Zeiss Supra 40 was used to observe morphology of samples. The beam energy was set to 5 -12 keV and the samples are attached by aluminum tape to avoid charging effect.

2.1.3 Energy-dispersive X-ray spectrometer (EDS)

EDS is measurement that is used to qualitatively and quantitatively analysis element in sample. The information of localized chemical analysis is obtained from X-ray spectrum emitted by a solid sample that is bombarded with a focused beam of electrons. This technique is able to detect the elements from atomic number 4 (Be) to 92 (U), however, the light element with the atomic number less than 10 may not be detected by all instruments. The EDS qualitative analysis is very straightforward and it is based on the analysis of lines from spectrum. Quantitative analysis gives details of concentrations of the elements present and the information from the measurement of intensities

of line for each element and for the elements in calibration standards of known composition. This technique could be used for study of element distribution by scanning the beam in a television-like raster mode, the intensity of selected X-rays is displayed and the element map is produced. In addition, specific mode of EDX can be chosen to gain the information like surface topography or mean atomic number differences from the images. An X-ray spectrometer component is usually attached to the scanning electron microscope (SEM). The SEM-EDS system not only can produce electron image but also element map and point analysis.

In this project, EDS (Cambridge) that is equipped within Philips XL30-FEG SEM system was used for elements analysis. The beam energy was set to 10 ~20 keV. The working distance was 8 mm and collecting time was 60 seconds.

2.1.4 Transmission electron microscopy (TEM)

Among all techniques so far, transmission electron microscopy (TEM) is the most advanced and powerful for the investigation of microstructure of sample. TEM had been used by researchers for studying crystal structure, orientation, composition as well as the dislocations. A typical TEM system is composed of an electron gun, a condenser lens system, objective and intermediate lenses, a sample chamber, projector systems, vacuum systems and a sample holder. The most common TEM have thermionic guns, which can generate accelerating electrons beams with potential range of 100-400 kV, this high-energy electro beam hit on sample with thickness around 100nm. In this process, some electrons pass through the sample directly while others are scattered.

There are two types of images modes that are dependent on the choice of objective apertures in TEM. [4] The schematic illustration of TEM in bright field mode is shown in Figure 2. 3, Bright filed mode is very common method used to create an image and also the most basic one. In bright fields mode, the objective aperture is placed on axis with the transmitted beams, thus, only the transmitted electrons can pass through. In this mode, the contrast formation of image is formed directly by absorption of electrons. The thicker area of sample or regions with higher atomic number will appear dark. Dark field is an imaging mode to observe the diffracted electron beam, different from that of bright field mode, the aperture is positioned off axis from the transmitted beams that only the directed electrons can pass through. In the image gained from this mode, the diffracted beam appears bright and the not diffracted electrons appear dark. Dark field mode is usually used to study crystalline grains and defects. In our study, another type of image mode is often used to observe the very details of sample. This mode is called as high-resolution imaging (HRTEM) where a large objective aperture is used, allowing the pass of both transmitted and diffracted beams. The image obtained from HRTEM is formed with the interference of the diffracted beams with the transmitted beam. The sample that is prepared for the observation on this mode should be less than 10nm to allow more electrons to go through.

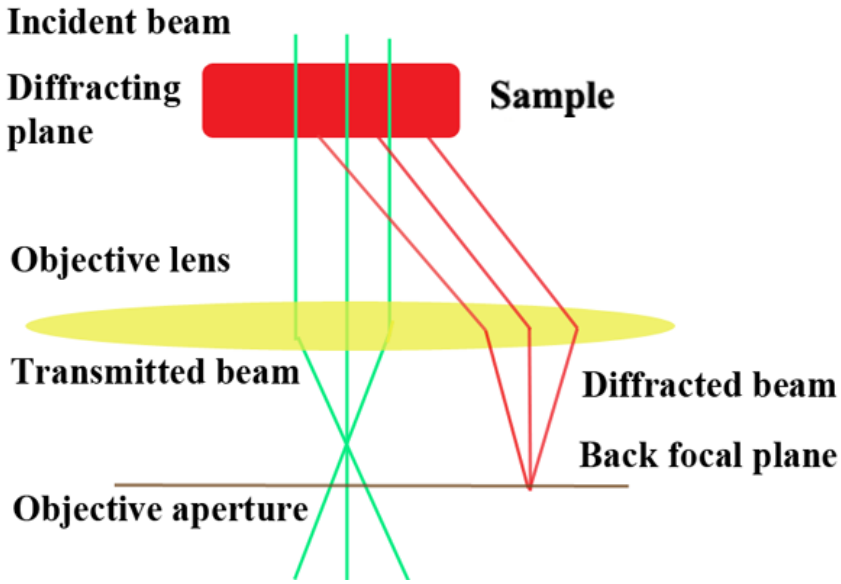

Figure 2. 3. Schematic illustration of TEM (bright field mode).[4]

Besides image mode, TEM also offer the diffraction mode, which can be used to study the crystal structure and lattice parameters of sample. The electron diffraction pattern is obtained on the fluorescent screen, originating from the sample area illuminated by the electron beam. For a single crystalline material, the image on the screen is a series of spots. Each spot refers to a satisfied diffraction condition of the sample's crystal structure. For polycrystalline material, a series of rings will be observed while for a glassy or amorphous material, a series of diffuse halos. According to the diffraction pattern, the inter-planer spacing can be derived using the equation: [4]

$$R = \lambda L / d_{hkl} \qquad (2.2)$$

Where d_{hkl} is the inter-planer distance for a particular set of reflecting planes {hkl}, R is the distance between the diffracted spot and the center spot on the focal plane, λ is the wavelength of the electron beam and L is the distance between the sample and the back focal plane.

In the work, a JEOL 3010 TEM was used to study the crystalline. The operating voltage is 300 kV. Nanoparticle samples are prepared by drying on a copper grid while film samples are treated with a mechanical polishing followed by an ion milling to perform final stage thinning. The Bravman-Sinclair method is used to prepare cross-sectional specimens.

2.1.5 Atomic force microscope (AFM)

Atomic force microscope (AFM) is one kind of scanning probe microscopes (SPM) for determining the surface topography of specimens at sub-nanometer resolution. The AFM operates by measuring atomic, Van der Waals force, chemical bonding, capillary force electrostatic force and magnetic force, etc, between sample and probe. [5] As sketched in Figure 2. 4, the probe mounted on soft cantilever is as sharp tip usually with 3-6 um tall and pyramid with 15-40 nm end radius. The probe interacts with the surface of sample and the force generated deflected the cantilever. The vertical and lateral deflection of the cantilever can be measured by the optical lever via reflection of laser beam. The reflected laser beam strikes a position-sensitive photo-detector with four-segment photo-detector. The generated electric signal is sent to a feedback loop to monitor and adjust distance to maintain a constant tip-sample interaction force during sample scanning. The obtained information then converted to image that reveal topography of sample.

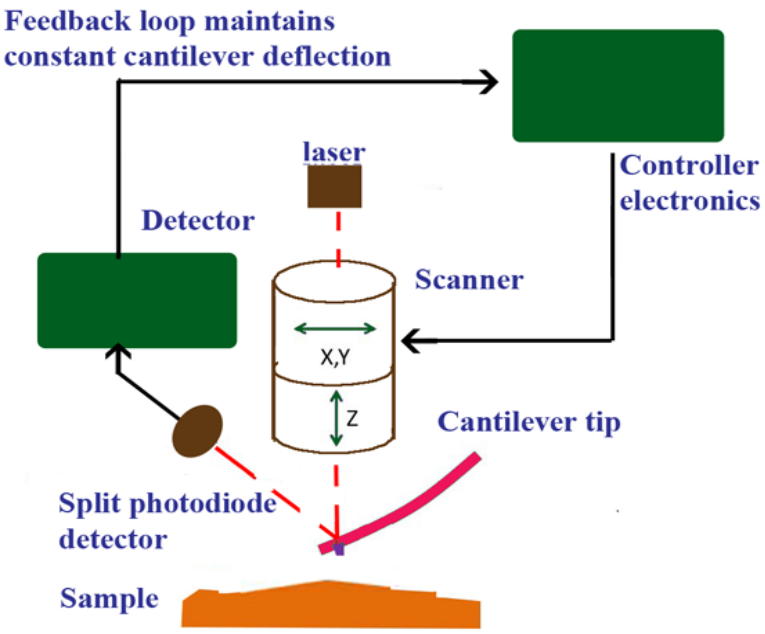

Figure 2. 4. Schematic illustration of AFM. [5]

In contact mode, AFM use feedback to regulate the force on the sample. The AFM not only measures the force on the sample but also regulates it, allowing acquisition of images at very low forces. The feedback loop consists of the tube scanner that controls the height of the tip; the cantilever and optical lever, which measures the local height of the sample; and a feedback circuit that attempts to keep the cantilever deflection constant by adjusting the voltage applied to the scanner. A well-constructed feedback loop is essential to microscope performance.

For the surface analysis, there are three basic image modes, contact mode, tapping mode and non-contact mode. In contact mode, AFM not only measure the force but also use feedback to regulate the force, allowing acquisition of images at low forces. This mode may cause some damage on surface of very soft materials. In tapping mode, the cantilever oscillates near its resonance

frequency. As the name suggests, the tip only slightly tap the surface of sample then its oscillation decrease. This mode eliminates the shear force and is preferred for measurement of soft sample as it cause less damage and produce higher image resolution. In non-contact mode, the cantilever oscillates at a frequency higher than its resonance frequency. This mode is capable for the test of liquid.

2.1.6 X-ray photoelectron spectroscopy (XPS)

XPS (X-ray photoelectron spectroscopy) is a non-destructive technique that can be used to study the elements composition, electronic state of the elements and empirical formula of a material. [6] A typical XPS system is composed of an X-ray source, an ultra-high vacuum stainless steel chamber, an energy analyzer, an electron collection lens, an electron detector system and a sample stage. The XPS is conducted by irradiating the sample surface with a soft (low energy) X-ray. This soft monoenergetic X-ray excites the electrons of the atoms and these electrons will be emitted from the atom as a photoelectron if their binding energy is lower than that of X-ray energy. Only the photoelectrons at very outer surface in the range from 10-100 Angstroms are able to escape from the surface for surface analysis technique due to the small mean free path of electrons in solids. The XPS spectrum is obtained by measuring the kinetic energy and the number of emitted electrons.

The kinetic energy (KE) can be can be measured as: [6]

$$KE = h\nu - BE - \varphi s \qquad (2.3)$$

Where $h\nu$ is the energy of photons, BE is the binding energy of the atomic orbital from which the electron escapes and φs is the work function of spectrometer. A typical XPS spectrum consists of a series of peaks

corresponding to the binding energies of the photoelectrons that produce these peaks. From XPS spectrum, we can gain direct information of element species as each element has its own characteristic peak. The quantitate analysis of element could be achieved by normalization and correction of each XPS signal with its relative sensitivity factor. The chemical states of element is corresponding to the position in the XPS spectra.

In this work, chemical states of iron were investigated by X-ray photoelectron spectroscopy (XPS, ESCA LAB 220i-XL spectrometer). The energy source was a non-monochromatic magnesium X-rays corresponding to a photon energy of 1253.6 eV. The total energy resolution was 900 meV. The XPS spectra were fitted by XPS peak 4.1 software.

2.1.7 Profilometer

The thicknesses of films are measured by profilometer. The profilometer measures the surface topography with a stylus that moves laterally across the sample surface with a constant force. The fluctuation of stylus caused by the change of height of sample surface generates an analog signal, which could be converted into a digital signal. The digital signal is recorded as a function of position and the surface parameters are calculated by specific software. A typical profilometer can measure small vertical features ranging from 10 nanometres to 1 millimetre.

In our study, a KLA-Tencor P-12EX Disk Profiler was used. It scans with a stationary stylus and a moving sample stage. The scan speed is in the range from 1 um/sec to 25 mm/sec.

2.2 Magnetic property characterization

2.2.1 Vibrating sample magnetometer (VSM)

Vibrating sample magnetometer (VSM) is a most commonly used technique to measure the magnetic properties of the sample. The measurements could be performed on solids, powders, single crystals, thin films, nanostructures and liquids and in the temperature form 4k to 1273k. The working principle of VSM is based on Faraday's law, [7] which states that induced electromotive force in any closed electrical circuit when there is a change of magnetic flux through the circuit.

$$V(t) = - C \cdot d\Phi / dt \qquad (2.4)$$

Where C is a constant. A schematic illustration of VSM system is shown in Figure 2. 5.

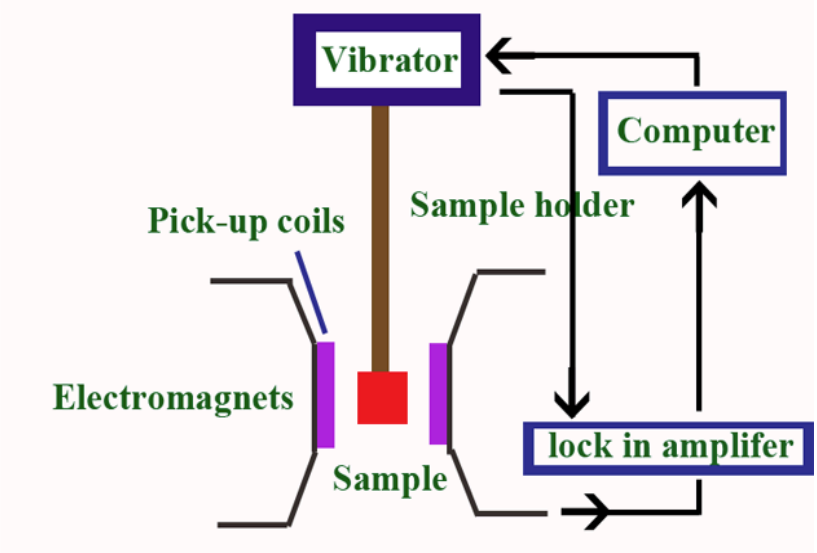

Figure 2. 5. Schematic illustration of VSM.

In the measurement setup, a magnetic sample is positioned in around two pickup coils. The oscillator gives sinusoidal signal that is translated by the transducer assembly into vertical vibration. Sample is fixed on a non-magnetic

sample holder is placed in the middle of two electromagnets, vibrating with a given frequency and amplitude. The stationary pickup coils are mounted on the poles of the electromagnet with the symmetry center coincides with the magnetic center of the sample. The induced signal in the pick-up coil is proportional to magnetic moment of sample, but independent on the external applied magnetic field. The lock-in amplifier measures the electrical signal and transfer to magnetic moment of sample. The hysteresis loop is drawn by plotting the magnetic field strength H against the magnetic induction B.

In this project, VSM (Lakeshore, Model 7404) was used to measure the magnetic properties of sample at room temperature. The calibration of equipment by Ni foil is conducted before the sample measurement. The sample was mounted on the holder with a Teflon tape.

2.2.2 Superconducting quantum interface device (SQUID)

A superconducting quantum interference device (SQUID) is a highly sensitive magnetometer used to measure extremely small magnetic fields. It consists of two superconducting rings separated by thin insulating layers (Figure 2. 6)

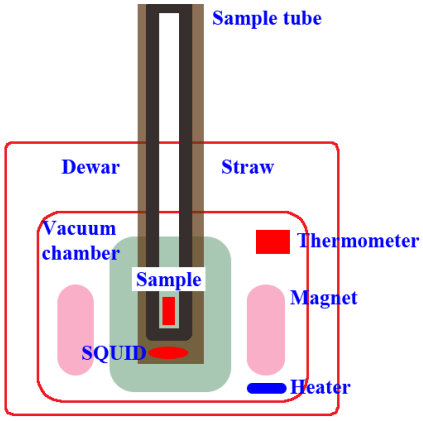

Figure 2. 6. A schematic diagram of SQUID system.

This technique is based on the Josephson effect [8] (superconductor-insulator-superconductor junction) and on the magnetic flux quantization in ring. The device is extremely sensitive to magnetic fields and is capable of detecting magnetic moment in the range of 10^{-6}–10^{-8} emu, enabling very precise magnetic measurements. In addition, SQUID system allows very accurate control of temperature in the range from 2 to 400 K. Thus, the great sensitivity of SQUID make it widely used in the fields where the strong magnetomerts are needed, for example, physics, archaeology, and geology.

In this project, a superconducting quantum interference device (SQUID, MPMS, Quantum design, USA) was used for examination of magnetic properties of samples. The measurements include hysteresis loops, zero-field-cooled (ZFC) and field cooled (FC) magnetization curves. Both ZFC and FC are temperature dependent by which we can study the magnetic behaviors of sample at various temperatures. In the ZFC mode, the sample is first cooled in zero field to the desired temperature, then selected the magnetic field is applied and the magnetization is measured in the warming up process. In the FC process, the sample is cooled down at selected magnetic field and the magnetization of sample is recorded during warming process. The sample in 5×5 mm is mounted on sample holder provided by Quantum Design. The magnet was reset before measurement to remove the remnant magnetic field trapped in the superconducting coils. The data collected is corrected by subtracting the contributions from the substrate and holder.

2.3 Electric property characterization

2.3.1 Physical property measurement system (PPMS)

The physical property measurement system (PPMS) is multi-functional equipment instrument offering the options for measuring a large variety of physical properties. The basic setup of PPMS is consisted of dewar with the superconducting magnet, pump for evacuating the sample chamber, power source and a lock-in amplifier. A schematic diagram of PPMS sample chamber is shown in Figure 2. 7. [9] Typical PPMS contains a number of different experimental technologies and can detect simultaneous thermal, magnetometry and electro-transport properties of materials by equipped with a temperature controller, magnetometer, AC transport and resistivity probe as well as a number of optical and surface microscopes.

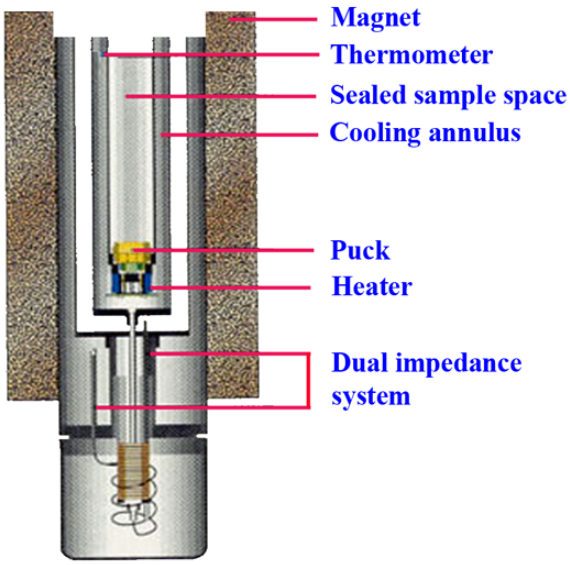

Figure 2. 7. A schematic diagram of PPMS sample chamber. [9]

The measurements of PPMS can conduct include AC Transport (AC Resistivity, Hall Coefficient, I-V Curve, Critical Current for superconductors),

DC Resistivity, and Heat Capacity for small samples as a function of magnetic field strength, pressure and temperature. The PPMS machine is controlled by user-friendly software that can control and monitor environment aspects (excitation voltage, frequency, and current) in the experiment. Most of the experimental options can be programmed in the temperature form 1.9 – 400 K with applied magnetic fields up to 9 T.

The samples that is cut to around 2mm x 2mm are inserted in the sample holder which contains pre-wired electronics to measure the functional properties. The sample chamber is vacuumed to 5Å~10^{-5} Torr in order to avoid oxidization.

2.4 Magnetic hyperthermia

The basic principle of magnetic hyperthermia is based on the usage of heat generated form magnetic nanoparticles under alternating magnetic field to kill the tumor cells. As shown in the Figure 2. 8, magnetic hyperthermia system is composed with AC power supplier, cupper coil and a temperature measurement system. The AC magnetic field generated from AC power supplier transfer the energy to the sample that is placed in the coil, generating heat through relaxation. The change of temperature caused by the heat produced is recorded by thermometer.

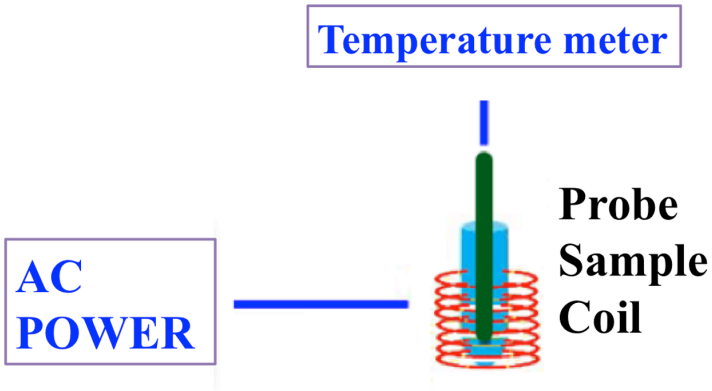

Figure 2. 8. A schematic diagram of magnetic hyperthermia system.

In this thesis, a magnetic hyperthermia system (Shenzhen Shuangping, SPG-10-II) was used to test the heating performance of nanoparticles. Specific absorption rate (SAR) value is used to evaluate the heat dissipation efficiency and the calculation of SAR value is given by: [10]

$$SAR=C\frac{\Delta T}{\Delta t}\frac{1}{m} \qquad (2.5)$$

Where, C is the specific heat of water (4.18 J/g °C), $\frac{\Delta T}{\Delta t}$ donates the initial slope of the time-dependent temperature curve. m is weight fraction of magnetic element.

2.5 PNA network analyzer

A vector network analyzer is an instrument used to measure the magnitude and phase characteristics of networks, amplifiers, components, and antennas. This analyzer can compare the incident signal with the transmitted signal or reflected signal. [11] A typical PNA network analyzer system is composed by built-in swept signal generator, a test set, a tuned receivers and display. Figure 2. 9 shows a generalized PNA network analyzer block diagram.

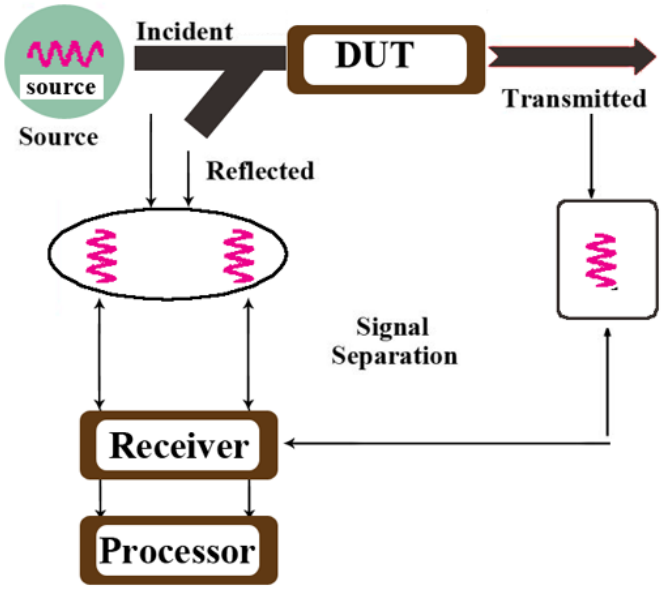

Figure 2. 9. A schematic diagram of PNA Network Analyzer.

In this thesis, the microwave measurement is carried out using PNA Network (Agilent PNA 8363B). The complex permeability (μ_r_=μ'+jμ'') and permittivity ($\varepsilon_r = \varepsilon'+j\varepsilon''$) of the composites were measured over the frequency range of 100 to 1300 MHz.

2.6 Evaluation of electrochemical properties

The electrochemical characteristics of materials are evaluated by a three-electrode cell system with cyclic voltammetry (CV) technique at room temperature. A schematic diagram of three-electrode cell system is shown in Figure 2. 10.

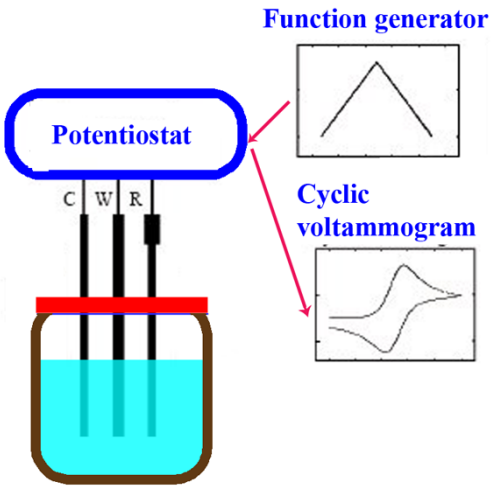

Figure 2. 10. A schematic diagram of three-electrode cell system.

Cyclic voltammetry is a potentiodynamic electrochemical measurement. This technique is used to obtain information on the thermodynamics of redox processes and the kinetics of heterogeneous electron-transfer reactions. [12] The electrochemical properties of a redox system could tell form the characteristic shapes of the voltammetric waves and their position on the potential scale.

In this thesis, a platinum sheet and a saturated $Hg/HgCl_2$ electrode were used as the counter and reference electrodes respectively. The working electrode is the film we deposited and it was fixed with a clamp. Cyclic voltammograms were recorded in the potential range between -1.2V and 0V at scan rates from 10mV/s to 50mV/s.

2.7 Fabrication techniques

2.7.1 Vapor-based techniques

As of today, a variety of different methods have been developed to grow magnetic Fe-based nanomaterials. Basically, these methods can be classified into vapor-based techniques and solution-based techniques.

For deposition of Fe-based films, vapor-based methods are common techniques used and most of them involve high vacuum systems, such as sputter deposition, pulse-laser deposition (PLD), molecular-beam epitaxy (MBE) and chemical vapor deposition (CVD). [13-17] Many works had been reported that vapor-based techniques could deposit ferrous alloy and ferrites with excellent interface and surface morphology. The disadvantage of these procedures is the high cost which restricts their potential application. [18]

2.7.2 Solution-based techniques

There had been a variety of synthesis methods reported to fabricate Fe-based nanoparticles including perception, micro emulsion mechanical milling in organic liquids, vapor phase deposition, hydrothermal synthesis under high pressure and polyol reduction techniques. [19-24] However, among all techniques developed for the synthesis of magnetic Fe-based nanoparticles, thermal decomposition as a solution-based wet chemical technique is one of the most common methods to fabricate monodisperse nanoparticles. Metal precursor and surfactant are added in heated solution, the nanoparticle will nucleate and grow at a higher reaction temperature. The size and the composition of as-synthesized nanoparticle are dependent on the reaction time, temperature, surfactant and so on. Nearly all metallic ferrous alloys and

ferrites had been reported synthesized through thermal decomposition. Synthesis of nanoparticles by the thermal decomposition gives relatively uniform, small size, single crystal and ferrofluid particles. Take iron oxide nanoparticles as example, thermal decomposition of the precursor can form pure iron nanoparticles at first, followed by the oxidation of Fe nanoparticle in air atmosphere. The formation of different iron oxide phases is controlled by use of precursor and the solvent or oxidizing reagent.

Apart from synthesis of nanoparticle, solution-based techniques can also be used to fabricate films. Typical solution-based techniques for ferrites and ferrous alloy include sol gel techniques, electroplating, and hydrothermal methods. [25-27] Compared with vapor-based methods, solution-based techniques are more cost-effective but their disadvantages include poor morphology, adhesion as well as limitation for thick film fabrication.

REFERENCES:

[1] C. Suryanarayana, M. Grant Norton, X-Ray Diffraction: A Practical Approach, USA **1998**.

[2] M. Eckert, Acta Cryst. **2012**, A68, 30.

[3] P. J. Goodhew, J. Humphreys, R. Beanland, Electron Microscopy and Analysis, CRC Press,USA **2000**.

[4] D. B. Williams, C. B. Carter, Transmission Electron Microscopy, A Textbook for Materials Science, Vol. 1: Basics, Plenum Press, New York and London **1996**.

[5] P. Eaton, P. West, Atomic Force Microscopy, OUP Oxford, UK **2010.**

[6] H. R. Verma, Atomic and Nuclear Analytical Methods XRF, Mössbauer, XPS, NAA and B63Ion-Beam Spectroscopic Techniques, Springer Berlin Heidelberg, USA **2007.**

[7] A. Niazi, P. Poddar, A. K. Rastogi, current science, **2000**, 79, 99.

[8] T. Ryhänen, H. Seppa, R. Ilmoniemi, J. Knuutila, J. Low Temp. Phys. **1989**, 76, 287.

[9] Y. J. Hong, Magnetic and Transport Properties of Oxide Thin Films, ProQuest, USA **2007**.

[10] M. ma, Y. Wu, J. Zhou, Y. K, Sun, Y, Zhang, N, Gu, J. Magn. Magn. Mater. **2004**, 268, 33.

[11] R. Collier, D. Skinner, Microwave Measurements, 3rd Edition, Institution of Engineering and Technology, UK **2007**.

[12] J. Heinze, Angew. Chem. Int. Ed. Eng. **1984**, 23, 831.

[13] L. adity, A, Srivastav, S. K. Sahoo, P. Das, C. Mukherjee, A, Misra, V. R. Reddy, R. S. Shinde, A, Gupta, S, Prasad, I, Samajdar, R.V. Nandedkar, N. Venkataramani J Nanosci Nanotechnol. **2008**, 8, 4135.

[14] A.P. Caricato, M. Fernández, Z. Frait, D. Fraitova, S. Luby, A. Luches, E. Majkova, G. Majni, R. Malych, P. Mengucci, Applied PhysA, **2004**, 79, 1251.

[15] J. B. Moussy, J. Phys. D: Appl. Phys. **2013**, 46, 143001.

[16] H. S. Jung, W. D. Doyle, S. Matsunum, J. Appl. Phys. **2003**, 93, 6462.

[17] A.G. Fitzgerald, R. Engin, Thin Solid Films, **1974**, 20, 317.

[18] B. Liu, T. Sun, J. Q. He, V. P. Dravid, ACS Nano **2010**, 4, 6836.

[19] N. Ballot, F. Schoenstein, S. Mercone, T. Chauveau, O. Brinza, N. Jouini, J Alloy Compd, **2012**, 536, S381.

[20] A.K. Giri, E.M. Kirkpatrick, P. Moongkhamklang, S. A. Majetich, V.G. Harris. Appl. Phys. Lett. **2002**, 80, 2341.

[21] M. Gheisari, M. Mozaffari, M. Acet, J. Amighian. J. Magn. Magn. Mater. **2008**, 320, 2618.

[22]H. Itoh, T. Sugimoto. J. Colloid Interface Sci. **2003**, 265, 283.

[23]Z. Jing, S. Wu. Mater. Lett. **2004**, 58, 3637.

[24] Q. Chen, Z.J. Zhang. Appl. Phys. Lett. **1998**, 73, 3156.

[25] Y. Okazaki. Y. Ohya, Y. Yanase, S. Magnetics, IEEE Trans. **2006**, 42, 2891.

[26] T. A. Sorenson, S. A. Morton, G. D. Waddill, J. A. Switzer, Am. Chem. Soc. **2002**, 124, 7604.

[27] S. H. Yu, M. Yoshimura, Chem. Mater. **2000**, 12, 3805.

Chapter 3 Magnetic-field-directed synthesis of Fe_3O_4 Nanoparticles

3.1 Introduction

As mentioned in chapter 1, Magnetic Fe-based nanoparticle have attracted great attention owing to its diverse biomedical applications in cancer therapy. [1,2] Therein, magnetite (Fe_3O_4) nanoparticles (NPs) are of particular interest as a result of their morphology-dependent physical and chemical properties. [3-5] Many biomedical applications, such as magnetic hyperthermia, in vivo magnetic resonance imaging (MRI) and drug delivery, require Fe_3O_4 NPs with designated shapes. [6-7] As a result, controlling the shape and size of magnetic nanoparticles has attracted enormous interests. [8] Most recently, significant effort has been made to investigate shape effect on hyperthermia performance of Fe_3O_4 NPs, which drives the development of shape controllable synthesis of Fe_3O_4 NPs. [9,10]

Numerous methods have been reported to synthesize Fe_3O_4 NPs including thermal decomposition, [11] co-precipitation, [12] hydrothermal growth, [13] electrochemical synthesis [14] and so on. Among them, thermal decomposition is demonstrated to be the most effective in shape control of Fe_3O_4 NPs. [15] Bateer *et al.* utilized polyisobutene succimide (PIBSI) to control the shapes of cubic, cuboctahedral and octahedral Fe_3O_4 NPs in thermal decomposition process. [16] Amara *et al.* synthesized Fe_3O_4 nanocubes and nanospheres

via adjusting annealing time during decomposing mixtures of ferrocene and polyvinylpyrrolidone (PVP). [17] However, previous studies only focused on small NPs (<50 nm). [16,17] Controlling the shape of large Fe_3O_4 NPs (>200 nm) still remains a challenge.

Besides factors such as surfactants, reducing agents and temperature, magnetic field is also known to be able to influence morphology of Fe_3O_4 NPs in hydrothermal [18] and co-precipitation [19-21] synthesis. More importantly, magnetic field causes no chemical contamination and can induce magnetic anisotropy to the synthesized NPs. However, the effect of external magnetic field on shapes and properties of Fe_3O_4 NPs in thermal decomposition process has not been investigated according to our best knowledge.

In this chapter, effect of magnetic field on Fe_3O_4 nanocubes (250 nm), nanocuboctahedrons (250 nm) and nanooctahedrons (80 nm) were investigated. Fe_3O_4 nanocubes and nanocuboctahedrons of 250 nm were obtained via applying 500 Oe and 0 Oe magnetic field respectively. Their magnetic properties were further studied both experimentally and via first-principles calculation. Moreover, the obtained NPs were coated with chitosan and well dispersed in water for hyperthermia measurement. Lastly, the magnetic hyperthermia performance of Fe_3O_4 nanocubes and nanocuboctahedrons were compared and discussed.

3.2 Experimental

3.2.1 Chemicals

Benzyl ether (≥98%), oleic acid (≥99%), iron (III) acetylacetonate (≥97.0%) were purchased from Sigma-Aldrich. Hexane (95%) and chloroform (99.9%) were obtained from Fisher Scientific and used as solvents for dispersion of as-synthesized NPs. Chitosan (low molecular weight) was purchased from Sigma-Aldrich for coating on Fe_3O_4 NPs. All chemicals used for synthesis of Fe_3O_4 NPs in this work were used without further purification.

3.2.2 Synthesis

Fe_3O_4 NPs were synthesized by thermal decomposition route. In a typical process, 10 mmol iron (III) acetylacetonate was dissolved in 20 mL benzyl ether containing in a 3-neck flask. 12 mmol oleic acid was further added into the solution as surfactant and reducing agent. The mixture was then sonicated for 15 min to ensure uniformity of the reaction solution. The 3-neck flask was placed under a static magnetic field generated by two permanent magnets as shown in Figure. 1(a). Distance between the two magnets was carefully adjusted to set the magnetic field strength to be 500 Oe. The reaction solution was then heated up to 170℃ for 15 min and finally to 280 ℃ for another 30 min. The heating rate in above processes was controlled to be 15℃/min. After reaction, the black mixture was cooled down to room temperature naturally. During the whole process, the reaction solution was protected under a flow of nitrogen to prevent oxidation of the products. Large Fe_3O_4 NPs (250 nm) were then separated using a permanent magnet. The final product was washed for three times using a mixture of ethanol and

hexane (volume ratio of 3:1) under sonication and finally dried at room temperature for 48h. Small Fe_3O_4 NPs (80 nm) were obtained by elongating the heating time at 170℃ to 1h with all other conditions fixed. Fe_3O_4 NPs synthesized without magnetic field were also prepared by conducting the above synthesis process without the two permanent magnets.

3.2.3 Characterization

The morphology of the as-prepared product was examined by field-emission scanning electron microscopy (FESEM; Zeiss Supra 40). Elemental information of the samples was analysed by energy-dispersive X-ray spectroscopy (EDX; Attachment of FESEM). Chemical states analysis of sample elements was performed by X-ray photoelectron spectroscopy (XPS; Kratos AXIS Ultra DLD). The shape and size of as-prepared NPs were determined by transmission electron microscopy (TEM; JEOL-3010 at 300kV). The crystal structure of the synthesized product was characterized by powder X-ray diffractometry (XRD; Bruker D8 Advanced Diffractometer System) with a Cu Ka (1.5418 Å) source. The magnetic properties were characterized by vibrating sample magnetometer (VSM; LakeShore Model 7407) and superconducting quantum interface design (SQUID; MPMS 3).

3.2.4 Magnetic hyperthermia study

The as-prepared hydrophobic Fe_3O_4 nanocubes and nanocuboctahedrons were firstly transferred to hydrophilic phase by coating chitosan as surfactant on surface of the NPs. Typically, 10 mg Fe_3O_4 nanocubes/nanocuboctahedrons was dispersed into 1 mL chloroform

followed by addition of chitosan (100 mg, 10 mL). The mixture was shaking in vortex for 4h under ambient conditions. After that, the remaining chloroform was evaporated at 60℃ for 1h. The obtained solution was centrifuged at 5000 rpm for 6 min. By removing the supernatant, the resulted precipitate was collected and dispersed in water for further hyperthermia measurement.

For hyperthermia measurement, 2 mL water-dispersed Fe_3O_4 solution was contained in a plastic holder and placed within a water-cooled copper coil driven by Inductelec A generator (Shenzhen Magtech Company Limited, China, SPG-10AB-II). The heating behaviour of the sample was studied at field strength of 560 Oe with applied frequency of 366 kHz. The ambient temperature was 28℃. The temperature of the sample was modulated by a fibre optical thermometry unit (LuxtronMD600). The specific absorption rate (SAR) and intrinsic loss power (ILP) of the sample were calculated by the following equations. [22]

$$\mathrm{SAR} = \mathrm{C}\frac{\Delta \mathrm{T}}{\Delta \mathrm{t}}\frac{1}{\mathrm{m_{Fe}}} \tag{3.1}$$

$$\mathrm{ILP} = \frac{\mathrm{SAR}}{\mathrm{H^2 f}} \tag{3.2}$$

Where C is the specific heat of the medium ($\mathrm{C} = 4.18\,\mathrm{J}\cdot\mathrm{g}^{-1}\cdot{}^{\circ}\mathrm{C}^{-1}$), $\frac{\Delta \mathrm{T}}{\Delta \mathrm{t}}$ is the maximum slope of the time-temperature curve and m_{Fe} is the weight fraction of the magnetic element in the sample, H and f are applied magnetic field strength and frequency respectively. Iron concentration of samples was measured by ICP-OES analysis using a Perkin-Elmer Dualview Optima 5300 DV ICP-OES.

3.2.5 First-principles calculations

First-principles calculations were performed using Vienna ab initio simulation package (VASP) based on density functional theory (DFT). [23] Electron-ion interaction was modelled by projector augmented wave (PAW) potentials.[24] Exchange and correlation effects for structural relaxation were approximated by generalized gradient approximation (GGA) [25] with Perdew-Burke-Ernzerhof (PBE). [26] The cutoff energy was set to be 400 eV in all calculations for plane-wave basis restriction. K-points were sampled under Monkhorst-Pack for Brillouin-zone integration. [27] For (001) surface model, $(\sqrt{2}\times\sqrt{2})$R45º surface unit cell and 11 atomic layers with the same top and bottom terminations were used. Similarly, for (111) surface model, 2×2 surface unit cell and 11 atomic layers with the same top and bottom terminations were used. For both models, three topmost surface layers on both top and bottom terminations are relaxed with all other atoms being fixed to simulate bulk. The forces acting on all relaxed atoms <0.05 eV/Å are reached for ionic relaxation and self-consistency accuracy of 10^{-4} eV for electronic loops. Surface magnetic anisotropy was calculated by non-collinear calculations via considering spin-orbital coupling using the algorithm implanted in VASP by Hobbs *et al*. [28] For all non-collinear calculations, self-consistency accuracy of 10^{-6} eV is reached for electronic convergence.

The most stable surface termination of Fe_3O_4 (001) and (111) were selected for study on surface magnetic anisotropy. Extensive work has been done to evaluate stability of different Fe_3O_4 surface terminations in literature. Pentcheva *et al.* concluded (001)-Fe_{oct}-termination is the most stable for (001)

surface according to DFT calculation and thermodynamic analysis. [29] By using spin-density functional theory, Grillo *et al.* reported (111)-Fe_{tet1}-O_1-termination is the most energetically favored for (111) surface.[30] As a result, (001)-Fe_{oct}- and (111)-Fe_{tet1}-O_1-surface model were built for further study on magnetic anisotropy. Energy $E_\perp$ when applying magnetic field perpendicular to surface was calculated by aligning magnetic dipole out of surface. Similarly, energy $E_\parallel$ when applying magnetic field parallel to surface was obtained by aligning magnetic dipole in surface. Several in-surface directions of magnetic dipole were investigated. The direction of magnetic dipole with the lowest $E_\parallel$ was finally determined for (001) and (111) surface model respectively. Surface magnetic anisotropy K_S is further obtained using the equation $K_S = \frac{E_\perp - E_\parallel}{2A}$ for each model, where A is surface area of model on each side.

3.3 Results and Discussion

3.3.1 Effect of external magnetic field

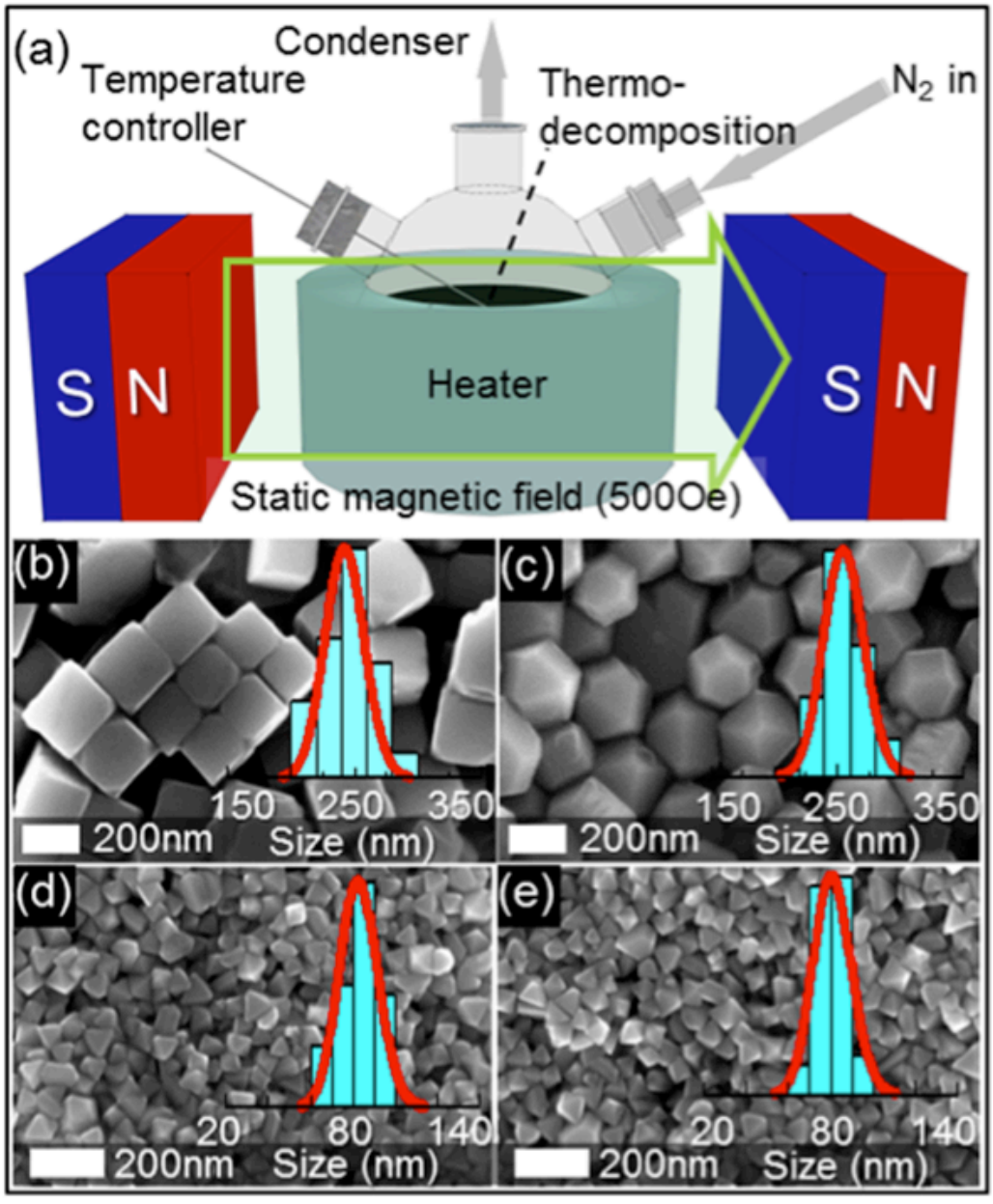

Figure. 3. 1. (a) Schematic diagram of experimental setup of magnetic-field-directed synthesis of Fe_3O_4 NPs, (b) and (c) SEM images of 250 nm Fe_3O_4 nanocubes (field assisted) and nanocuboctahedrons (no magnetic field) respectively, (d) and (e) SEM images of 80 nm Fe_3O_4 nanooctahedrons synthesized with and without magnetic field respectively.

Large Fe_3O_4 NPs were synthesized via thermal decomposition with and without applying magnetic field, whose SEM images were shown in Figure 3.1(b) and (c) respectively. It can be seen that the samples are of good uniformity in both shape and size. The size distribution of NPs synthesized with and without applying magnetic field is close with each other. The average sizes of the two samples are measured to be 250 nm. Under a static magnetic field of 500Oe, Fe_3O_4 nanocubes form in sharp contrast with the nanocuboctahedrons if no magnetic field is present. The phenomenon suggests that magnetic field is effective to transform Fe_3O_4 nanocuboctahedrons into nanocubes. To further explore the influence of magnetic field on Fe_3O_4 NPs, we purposely elongated the heating time at 170℃ to 1h and obtained NPs of 80 nm. The SEM images of the 80 nm samples synthesized with and without applying magnetic field were shown in Figure 3. 1(d) and (e) respectively. It can be seen that both samples are octahedral regardless of presenting magnetic field. It is worthwhile to note that a higher magnetic field of 900 Oe was still found to be ineffective on tuning the shape of 80 nm Fe_3O_4 nanooctahedrons. It implies that magnetic field has negligible effect on Fe_3O_4 nanooctahedrons. The above findings suggest that Fe_3O_4 nanocuboctahedrons experience more significant interaction with magnetic field than nanooctahedrons.

3.3.2 Structural characterization

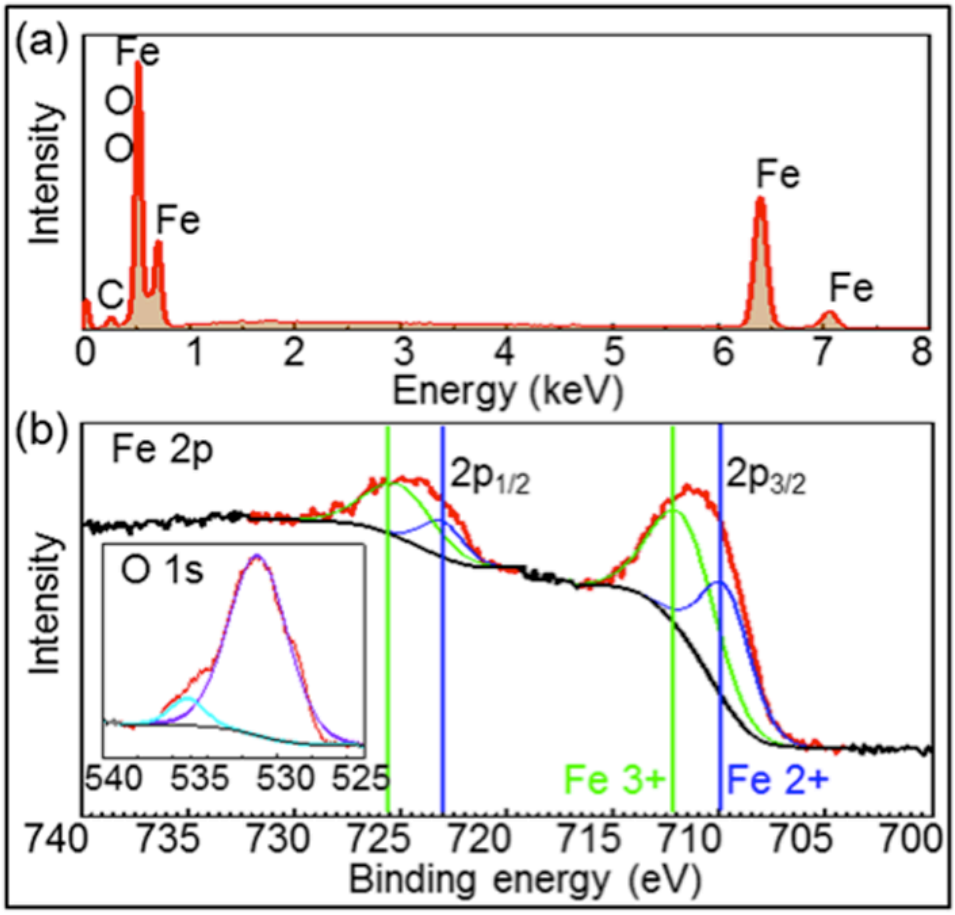

Figure 3. 2. (a) EDX spectrum and (b) XPS Fe 2p spectrum of as-prepared 250 nm Fe_3O_4 nanocubes. Inset in (b) XPS O1s spectrum of the sample.

EDX analysis was further conducted to obtain elemental information of the samples. A typical EDX spectrum (250 nm Fe_3O_4 nanocubes) is demonstrated in Figure 3.2(a). The elements detected in all samples are Fe, O and C suggesting that our samples are free of contamination by other metal oxides. Moreover, XPS was employed to analyse chemical states of Fe and O for the nanocubes as shown in Figure 3.2(b). No satellite can be observed around the binding energy of 715.5 eV for FeO and 719.0 eV for γ-Fe_2O_3, excluding the existence of FeO or γ-Fe_2O_3 in

our samples. [31] Characteristic Fe 2p peak at 706.6 eV for metallic Fe is not detected. It ruled out the presence of Fe cluster. [32] Furthermore, Fe $2p_{1/2}$ and Fe $2p_{3/2}$ peaks were fitted for Fe^{3+} (green) and Fe^{2+} (blue). The ratio between Fe^{3+} and Fe^{2+} was determined to be 2.06:1 confirming the Fe_3O_4 phase is pure. [33] XPS O1s spectrum is shown in inset of Figure 3.2(b).

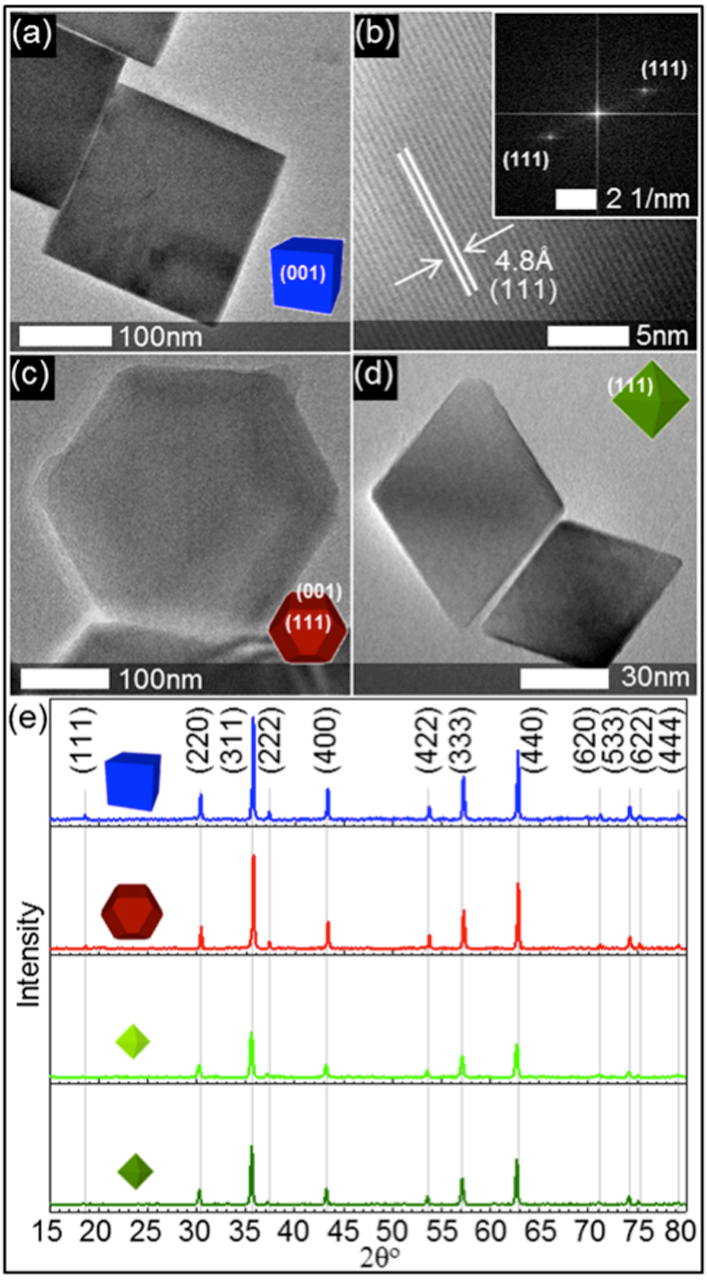

Figure 3. 3. (a), (c) and (d) TEM images and schematic drawings of as-prepared Fe_3O_4 nanocubes, nanocuboctahedrons and nanooctahedrons respectively, (b) HR-TEM image of Fe_3O_4 nanocubes; Inset in (b) Fourier transform electron diffraction (ED) image of the corresponding HR-TEM image, (e) XRD spectra of Fe_3O_4 nanocubes (blue), nanocuboctahedrons (red), nanooctahedrons synthesized with (light green) and without (dark green) magnetic field.

To have a close look at the shapes of synthesized Fe_3O_4 NPs, TEM images of different samples were further taken as seen in Figure 3.3 (a), 3(c) and 3(d), which are nanocubes, nanocuboctahedrons and nanooctahedrons respectively. The shapes of different samples from TEM images are in good agreement with SEM images and the size of Fe_3O_4 NPs also matches well with SEM measurement. Moreover, high-resolution TEM ima image of Fe_3O_4 nanocubes is shown in Figure 3. 3(b). The lattice spacing is measured to be 4.8 Å which is determined to be Fe_3O_4 (111) plane. The corresponding Fourier transform electron diffraction image of HR-TEM is shown in the inset of Figure 3. 3(b). Only one pair of diffraction plane can be observed indicting good crystallinity of the sample. The crystal structure of Fe_3O_4 samples were further characterized by XRD as seen in Figure 3. 3(e). Positions and relative intensities of diffraction peaks for all samples match well with the standard Fe_3O_4 diffraction data (JCPDS no. 88-0135). [34] No α-Fe_2O_3, FeO or metallic Fe was detected. It is noticed that large NPs (250 nm, blue and red) have obviously stronger peak intensity than that of small NPs (80 nm, light and dark green).

3.3.3 Magnetic properties

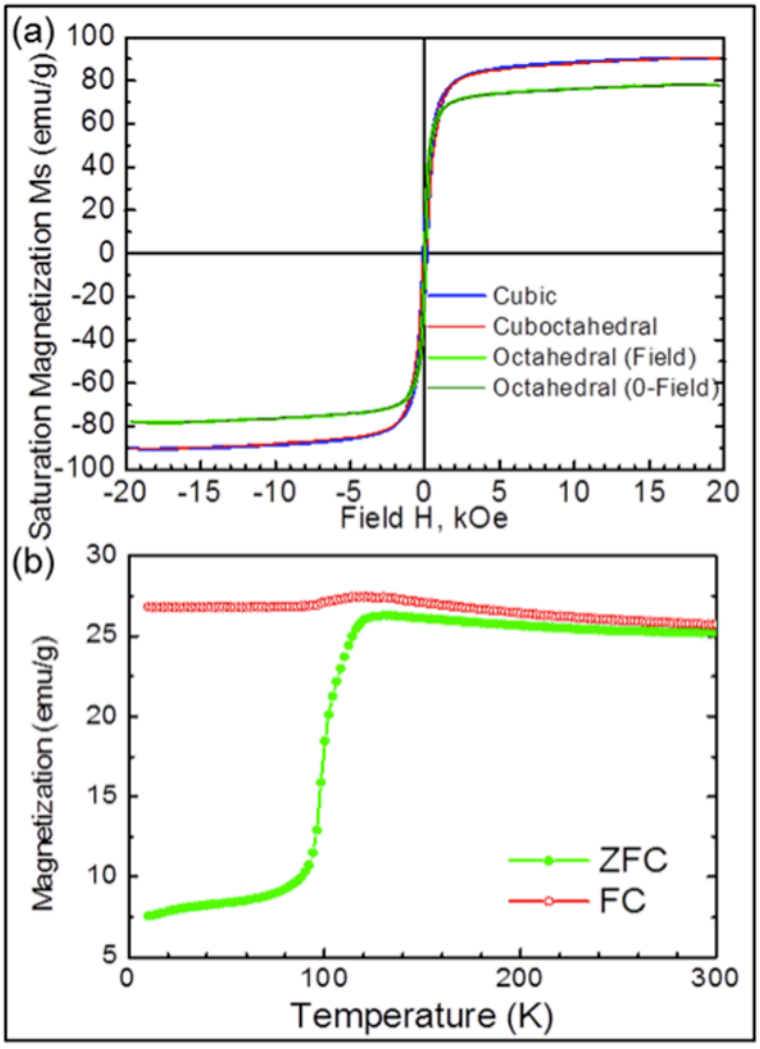

Figure 3. 4. (a) Magnetic hysteresis loops of the Fe_3O_4 nanocube (250 nm), nanocuboctahedron (250 nm), and nanooctahedron (80 nm), (b) Zero-field-cooling (ZFC) and field-cooling (FC) curves of the 250 nm Fe_3O_4 nanocubes.

The magnetic properties of the above dry-powder samples were further studied using VSM as shown by the hysteresis loops in Figure. 3.4 (a). It can be seen that both Fe_3O_4 nanocubes (blue) and nanocuboctahedrons (red) of 250 nm have saturation magnetization (Ms) of 90 emu/g which is close to that of bulk Fe_3O_4 (92 emu/g). Interestingly, Fe_3O_4 nanooctahedrons of 80 nm synthesized with (light green) and without

(dark green) applying magnetic field have significantly lower Ms of 78 emu/g. Furthermore, the magnetization of nanocubes was also measured as a function of temperature in conditions of zero-field-cooling (ZFC) and field-cooling (FC). In a typical ZFC measurement, the sample was firstly cooled down to 10K without applying external magnetic field. The magnetization was then measured while raising the temperature to 300K. In FC measurement, the sample was cooled to 10K under an applying external magnetic field of 500 Oe. After that, the magnetization measurement was taken as temperature was rising to 300K. In this study, both ZFC and FC measurements were taken under a magnetic field of 500 Oe. Figure 3.4(b) shows the ZFC-FC curves of 250 nm Fe_3O_4 nanocubes. A clear and sharp Verwey transition was observed at ~110 K, which is a characteristic magnetic feature of Fe_3O_4 and hence confirming the phase of Fe_3O_4. [33]

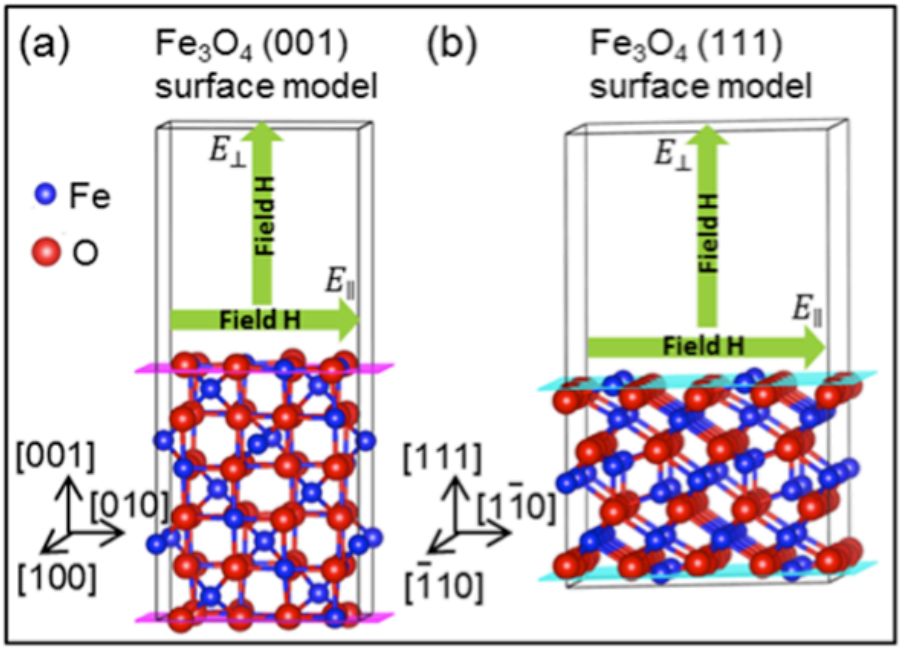

Figure 3. 5. (a) and (b) Fe_3O_4 (001) and (111) surface models, respectively. The corresponding surface magnetic anisotropy K_S(001)

and $K_S(111)$ are calculated by aligning magnetic dipole in and out of surface for each model.

To understand the influence of magnetic field on the shapes of synthesized NPs, the 250 nm nanocubes and nanocuboctahedrons are compared in detail. It can be seen in Figure 3.3 (a) that all surfaces of nanocubes are all (001) plane of Fe_3O_4 according to Wulff construction. While for nanocuboctahedrons as seen in Figure 3.3 (c), six of the surfaces are (001) plane and eight are (111) plane. [36] Thus, as another point of view, the change in shape from nanocuboctahedron to nanocube is the formation of (001) plane from (111) plane. Therefore, the magnetic properties of (001) and (111) surfaces can be crucial in the interaction between magnetic field and NPs. As a result, first-principles calculation was performed to investigate the magnetic anisotropy of (001) and (111) surfaces. [37] The most stable (001) and (111) surfaces of Fe_3O_4 were firstly chosen for study as seen in Figure 3.5 (a) and 3.5 (b) respectively. The surface magnetic anisotropy K_S was evaluated by firstly calculating the energies of surface model when magnetic dipole is aligning in surface ($E_{\parallel}$) and out of surface ($E_{\perp}$). K_S is further obtained using the equation $K_S = \frac{E_{\perp} - E_{\parallel}}{2A}$, where A is surface area of model on each side. The obtained magnetic anisotropy of (001) surface ($K_S(001)$) and (111) surface ($K_S(111)$) are both positive, indicating that both two Fe_3O_4 surfaces have in-plane magnetic anisotropy. $K_S(001)$ is calculated to be ~0.37 erg/cm^2 which is more than double of $K_S(111)$ (~0.18 erg/cm^2). It reveals that (001) surface has a significantly higher magnetic anisotropy than (111) surface. Thus, it can be possible that an external magnetic

field of a fixed direction induces formation of high-anisotropy (001) surface from low-anisotropy (111) surface. Consequently, the formation of (001) surface under a static magnetic field might be one of the reasons for promoting the formation of nanocube. Furthermore, as reported by Martinez-Boubeta, high surface magnetic anisotropy of NPs results in enhanced magnetic hyperthermia performance. [6] As a result, a detailed comparative study of magnetic hyperthermia performance on nanocubes and nanocuboctahedrons was carried out in the later part.

3.3.4 Hyperthermia properties

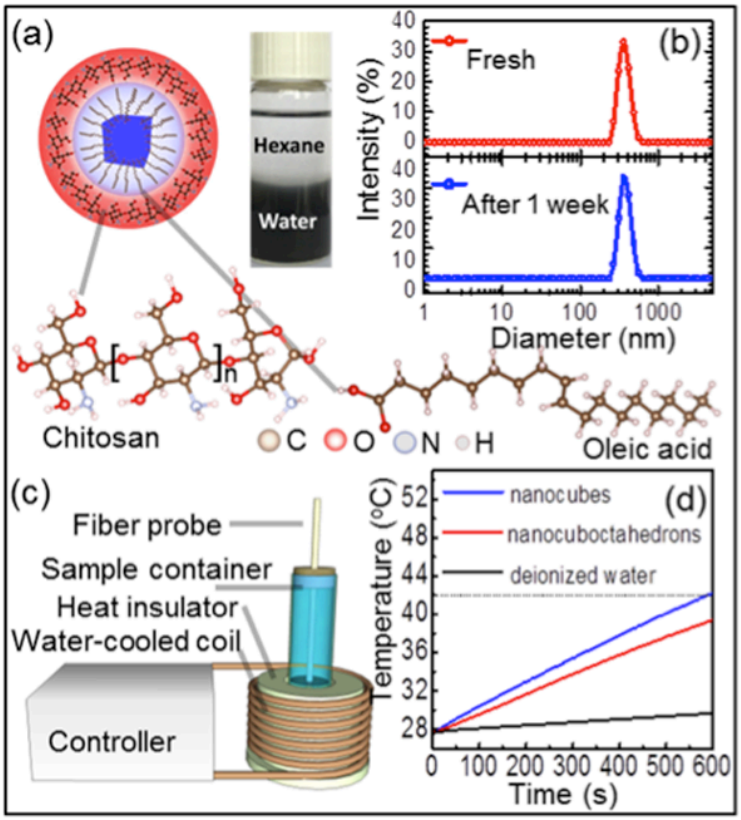

Figure 3. 6. (a) Left: schematic diagram of Fe_3O_4 nanocubes coated with chitosan, Right: well-dispersed chitosan-coated nanocubes in water, (b) Dynamic light scattering (DLS) plots of chitosan-coated nanocubes dispersed in water; Red: fresh sample; Blue: sample dispersed in water for a week, (c)

Schematic diagram of magnetic hyperthermia measurement system, (d) Hyperthermia temperature-time dependence curves for Fe_3O_4 nanocubes (blue) and nanocuboctahedrons (red) with equal Fe concentration and deionized water (black).

As reported in literature, toxicity of iron oxide NPs decreases with increasing particle size from nano-meter (<100 nm) to micron-meter range. [38,39] Könczöl *et al.* reported that larger magnetite particles induced less genotoxicity. [40] Zhu *et al.* found that submicron-sized iron oxide particles (280 nm) generated less toxic effect than nano-sized particles (22 nm). [33719.0 eV for γ-Fe_2O_3,] [41] Therefore, we further studied magnetic hyperthermia performance of 250 nm Fe_3O_4 nanocubes and nanocuboctahedrons. The as-prepared NPs were hydrophobic due to attached oleic acid molecules on the surface, thus they need to be transferred into hydrophilic phase to be water-dispersible for hyperthermia measurement and application. We thus coated an additional layer of biocompatible chitosan with the hydrophobic side connected to oleic acid and hydrophilic side exposed out as seen in Figure 3.6(a). The coated NPs could be well dispersed in water and maintained uniform for a week as shown by the photo in Figure 3.6(a) and their dynamic light scattering (DLS) plots in Figure 3.6(b). The hyperthermia performance of the solutions was further tested by a hyperthermia measurement set-up shown in the schematic diagram in Figure 3.6(c). The resulted temperature-time dependent curves in Figure 3. 6(d) demonstrate that Fe_3O_4 nanocubes have higher heating rate than nanocuboctahedrons and can reach 42^oC in 600s. Moreover, SAR values of the nanocubes and nanocuboctahedrons were calculated, which are 1250 W/g and 800 W/g respectively. The corresponding ILP values are 1.7 nH·m^2/kg and 1.09

$nH \cdot m^2/kg$ respectively. It can be seen that ILP value of nanocubes is 56% higher than that of nanocuboctahedrons. The improved hyperthermia performance of nanocubes may be attributed to increased (001) surfaces magnetic anisotropy of cubic particles with respect to (111) surfaces of cuboctahedral ones. [6] The SAR and ILP values suggest that the 250 nm Fe_3O_4 nanocubes have excellent heating capability, which is comparable to the performance of superparamagnetic Fe_3O_4 NPs reported in literature. [42] Thereby, the large Fe_3O_4 nanocubes demonstrate potential applications in magnetic hyperthermia therapy.

3.4 Conclusions

In conclusion, we successfully employed a static magnetic field of 500 Oe to manipulate the shapes and surfaces of Fe_3O_4 NPs synthesized via thermal decomposition route. The static magnetic field induced formation of Fe_3O_4 nanocubes (250 nm) in sharp contrast with nanocuboctahedrons if no magnetic field was present. Fe_3O_4 nanooctahedrons (80 nm) were also obtained by adjusting the pre-heating time of reaction precursor. We demonstrated that the magnetic-field-directed synthesis was effective for Fe_3O_4 nanocuboctahedrons and had negligible effect on nanooctahedrons. This phenomenon may be because that Fe_3O_4 nanocuboctahedrons have higher saturation magnetization or higher magnetic anisotropy. A comprehensive study was carried out to examine the size, shape, magnetism, crystal structure, elemental and chemical information of the synthesized samples. Furthermore, first-principles calculation reveals that surface magnetic anisotropy of Fe_3O_4 (001) surface is double that of (111) surface which

may be crucial for interaction between magnetic field and NPs. Moreover, the hyperthermia performance of large NPs was investigated. The NPs were successfully transferred into hydrophilic phase by coating of chitosan. The hyperthermia heating rate, SAR and ILP values of Fe_3O_4 nanocubes synthesized under magnetic field were significantly higher than those of nanocuboctahedrons obtained without applying magnetic field. The better hyperthermia performance of cubic particles might be due to higher magnetic anisotropy of (001) surfaces. In short, this work may pave the way for future development of magnet-field synthesis and biomedical applications of Fe_3O_4 NPs.

REFERENCES:

[1] R. Weissleder, M. Nahrendorf, M. J. Pittet, Nat. Mater. **2014**, 13, 125.

[2] X. L. Liu, H. M. Fan, J. B. Yi, Y. Yang, E. S. G. Choo, J. M. Xue, D. D. Fan , J. Ding, J. Mater. Chem. **2012**, 22, 8235.

[3] Y. Yang, Y. Yang, W. Xiao, J. Ding, J. Appl. Phys. **2014**, 115, 17A521.

[4] Y. Yang, X.-L. Liu, J.-B. Yi, Y. Yang, H.-M. Fan, J. Ding, J. Appl. Phys. **2012**, 111, 044303.

[5] Y. Yang, X. Liu, Y. Yang, W. Xiao, Z. Li, D. Xue, F. Li, J. Ding, J. Mater. Chem. C, **2013**, 1, 2875.

[6] C. Martinez-Boubeta, K. Simeonidis, A. Makridis, M. Angelakeris, O. Iglesias, P. Guardia, A. Cabot, L. Yedra, S. Estrade, F. Peiro, Z. Saghi, P. A. Midgley, I. Conde-Leboran, D. Serantes, D. Baldomir, Sci. Rep. **2013**, 3, 1652.

[7] J. Fang, P. Chandrasekharan, X.-L. Liu, Y. Yang, Y.-B. Lv, C.-T. Yang, J. Ding, Biomaterials **2014**, 35, 1636.

[8] X. H. Huang, Z. Y. Zhan, X. Wang, Z. Zhang, G. Z. Xing, D. L. Guo, D. P. Leusink, L. X. Zheng, T. Wu, Appl. Phys. Lett. **2010**, 97, 203112.

[9] C. Hofmann, I. Rusakova, T. Ould-Ely, D. Prieto-Centurión, K. B. Hartman, A. T. Kelly, A. Lüttge, K. H. Whitmire, Adv. Funct. Mater. **2008**, 18, 1661.

[10] P. Guardia, A. Labarta, X. Batlle, J. Phys. Chem. C **2010**, 115, 390.

[11] L. Li, Y. Yang, J. Ding and J. Xue, Chem. Mater. **2010**, 22, 3183.

[12] I. Nyirő-Kósa, A. Rečnik, M. Pósfai, J. Nanopart. Res. **2012**, 14, 1.

[13] Z. J. Zhang, X. Y. Chen, B. N. Wang, C. W. Shi, J. Cryst. Growth **2008**, 310, 5453.

[14] S. Franger, P. Berthet, J. Berthon, J. Solid State Electro. **2004**, 8, 218.

[15] C. H. Ho, C.-P. Tsai, C.-C. Chung, C.-Y. Tsai, F.-R. Chen, H.-J. Lin, C. H. Lai, Chem. Mater. **2011**, 23, 1753.

[16] B. Bateer, C. Tian, Y. Qu, S. Du, T. Tan, R. Wang, G. Tian, H. Fu, CrystEngComm **2013**, 15, 3366.

[17] D. Amara, J. Grinblat, S. Margel, J. Mater. Chem. **2012**, 22, 2188.

[18] M. Wu, Y. Xiong, Y. Jia, H. Niu, H. Qi, J. Ye, Q. Chen, Chem. Phys. Lett. **2005**, 401, 374.

[19] D. Hu, Y. Wang, Q. Song, Particuology **2009**, 7, 363.

[20] G. Nabiyouni, M. Julaee, D. Ghanbari, P. C. Aliabadi, N. Safaie, J. Ind. Eng. Chem. **2014**, 21, 599.

[21] R. Y. Hong, T. T. Pan, Y. P. Han, H. Z. Li, J. Ding, S. Han, J. Magn. Magn. Mater. **2007**, 310, 37.

[22] M. Kallumadil, M. Tada, T. Nakagawa, M. Abe, P. Southern, Q. A. Pankhurst, J. Magn. Magn. Mater. **2009**, 321, 1509.

[23] G. Kresse, J. Furthmüller, Phys. Rev. B **1996**, 54, 11169.

[24] P. E. Blöchl, Phys. Rev. B **1994**, 50, 17953.

[25] J. P. Perdew, J. A. Chevary, S. H. Vosko, K. A. Jackson, M. R. Pederson, D. J. Singh,C. Fiolhais, Phys. Rev. B **1992**, 46, 6671.

[26] J. P. Perdew, K. Burke, M. Ernzerhof, Phys. Rev. Lett. **1996**, 77, 3865.

[27] H. J. Monkhorst, J. D. Pack, Phys. Rev. B. **1976**, 13, 5188.

[28] D. Hobbs, G. Kresse, J. Hafner, Phys. Rev. B, **2000**, 62, 11556.

[29] R. Pentcheva, F. Wendler, H. L. Meyerheim, W. Moritz, N. Jedrecy , M. Scheffler, Phys. Rev. Lett. **2005**, 94, 126101.

[30] M. E. Grillo, M. W. Finnis, W. Ranke, Phys. Rev. B, **2008**, 77, 075407.

[31] T. Fujii, F. M. F. de Groot, G. A. Sawatzky, F. C. Voogt, T. Hibma, K. Okada, Phys. Rev. B **1999**, 59, 3195.

[32] M. C. Biesinger, B. P. Payne, A. P. Grosvenor, L. W. M. Lau, A. R. Gerson, R. S. C. Smart, Appl. Surf. Sci. **2011**, 257, 2717.

[33] X. L. Huang, Y. Yang, J. Ding, Acta Mater. **2013**, 61, 548.

[34] Y. Yang, X. Liu, Y. Lv, T. S. Herng, X. Xu, W. Xia, T. Zhang, J. Fang, W. Xiao, J. Ding, Adv. Funct. Mater. **2014**, 25, 812.

[35] M. P. Morales, S. Veintemillas-Verdaguer, M. I. Montero, C. J. Serna, A. Roig, L. Casas, B. Martínez, F. Sandiumenge, Chem. Mater. **1999**, 11, 3058.

[36] M. Jamet, W. Wernsdorfer, C. Thirion, V. Dupuis, P. Mélinon, A. Pérez, D. Mailly, Phys. Rev. B **2004**, 69, 024401.

[37] F. Bødker, S. Mørup, S. Linderoth, Phys. Rev. Lett. **1994**, 72, 282.

[38] B. A. Katsnelson, T. D. Degtyareva, I. I. Minigalieva, L. I. Privalova, S. V. Kuzmin, O. S. Yeremenko, E. P. Kireyeva, M. P. Sutunkova, I. I. Valamina, M. Y. Khodos, A. N. Kozitsina, V. Y. Shur, V. A. Vazhenin, A. P. Potapov, M. V. Morozova, Int. J. Toxicol. **2011**, 30, 59.

[39] B. Katsnelson, L. I. Privalova, S. V. Kuzmin, T. D. Degtyareva, M. P. Sutunkova, O. S. Yeremenko, I. A. Minigalieva, E. P. Kireyeva, M. Y. Khodos, A. N. Kozitsina, N. A. Malakhova, J. A. Glazyrina, V. Y. Shur, E. I. Shishkin and E. V. Nikolaeva, Int. J. Occup. Env. Heal., **2010**, 16, 508.

[40] M. Könczöl, S. Ebeling, E. Goldenberg, F. Treude, R. Gminski, R. Gieré, B. Grobéty, B. Rothen-Rutishauser, I. Merfort, V. Mersch-Sundermann, Chem. Res. Toxicol. **2011**, 24, 1460.

[41] M.-T. Zhu, W.-Y. Feng, B. Wang, T.-C. Wang, Y.-Q. Gu, M. Wang, Y. Wang, H. Ouyang, Y.-L. Zhao, Z.-F. Chai, Toxicology **2008**, 247, 102.

[42] A. Hervault, N. T. K. Thanh, Nanoscale **2014**, 6, 11553.

Chapter 4 A facile solution-based method for epitaxial growth of Fe_3O_4 and other ferrite films

4.1 Introduction

In Chapter 3, Magnetic-field-directed synthesis of Fe_3O_4 nanoparticle and its hyperthermia properties had been demonstrated. In this chapter, we study the properties and applications of magnetic Fe_3O_4 in film form along with its ferrites counterparts.

Spinel magnetic ferrites in form of Fe $(Fe, M)_2O_4$ with M = Mn, Ni, Zn and Co have been intensively used in many engineering applications such as generator, motor, transformer, conductor etc. [1-6] Apart from their chemical stability and economy, their high resistivity is of particular importance for many high-frequency applications [7-11] whereas reduction of eddy current is crucial. Recently, thick spinel ferrite films have attracted increasing attention because of their great potentials in energy harvester, inductor on chip for power efficiency and MEMS devices. [12-19] Most film growth techniques used for deposition of ferrite films are physical and chemical vapor deposition, such as sputtering, [20-23] pulse laser deposition (PLD), [24-27] molecular-beam epitaxity (MBE) [28-31] and chemical vapor deposition (CVD). [32-35] High-quality and epitaxial ferrite films have been reported by physical and chemical vapor deposition techniques. However, as vacuum is frequently required for these physical and chemical vapor techniques, their high cost restricts their potential applications. [36] Besides, these techniques are not suitable for fabrication of thicker magnetic films in order of submicron and micron meter.

Wet chemical routes have been widely used for the fabrication of thick oxide films (including spinel ferrites). [37-40] However, post heat-treatment is frequently required for the formation of the required phase(s). Their relatively poor adhesion can limit applications. These films usually have an isotropic crystallographic nature, which sometimes is not favorable for the optimization of magnetic properties (for example for ideal remanence, coercivity and magnetic anisotropy).

Based on the above discussion, solution-based film deposition methods had been investigated for epitaxial growth of thicker ferrite films with comparable quality. Compared with extensively reports on epitaxial growth of ferrite films through vapor-based techniques, there have been a few reports of fabrication of epitaxial ferrite films by solution-based techniques. Successful examples include the growth of epitaxial Fe_3O_4 film through electrodeposition, [41] deposition of epitaxial $CoFe_2O_4$ by sol-gel and multiferroic $BiFeO_3$ by hydrothermal. [42,43] However, high temperature treatment for crystallization is still needed for most solution-based methods. The post-annealing may result in interdiffusion and relatively rough surface. [44] Besides, good adhesion between coating and substrate is still a challenge for solution-based methods, but it is required for most industrial applications.

In this chapter, we have successfully developed a facile approach towards the epitaxial growth of thick ferrite films based on thermal decomposition. For example, thick epitaxial Fe_3O_4 films with smooth surface and strong adhesion have been fabricated on MgO different single crystal substrates with and

without Fe_3O_4 seed layers. Hard magnetic cobalt ferrite (H_C =1450Oe) and soft magnetic nickel and manganese ferrite with high resistivity ($\rho > 1\times10^4 \Omega.\,cm$) have been grown via thermal co-decomposition of 2-3 precursors.

4.2 Experimental

4.2.1 Chemicals

Different chemical precursors $Fe(acac)_3$ (97%), $Co(acac)_2$ (97%), $Mn(acac)_2$ (97%), $Ni(acac)_2$(95%), $Al(acac)_3$(99%), $Zn(acac)_2.xH_2O$, oleic acid (OA), Benzyl ether 98%, were purchased from Sigma-Aldrich. All the reagents were analytical grade and were used without further purification.

4.2.2 Deposition of ferrites film

For Fe_3O_4 films, substrate was placed at a three-neck flask, then desired proportions of $Fe(acac)_3$, oleic acid (OA) and Benzyl ether were loaded inside. After the set of magnetic bar in flask, the mixture was dehydrated at 180 °C for 10 mins under a flow of argon and then quickly heated to 280 °C for 20 mins. At the refluxing temperature, it was found that the solution turned from red into muddy black. After the black solvent was cooled to room temperature, the substrate was removed from the flask and washed 3 times with hexane in solicitor. The as-deposited Fe_3O_4 films were characterized by different measurements. The preparation of (Co, Ni, Mn and Zn) ferrites films were performed using co-decomposition by adding desired proportion of the corresponding precursors together with $Fe(acac)_3$ in the three-neck flask before reaction. The different ferrite films were obtained through a similar procedure as for the pure Fe_3O_4 films.

Single crystal MgO substrates with orientations of (111), (110) and (100) were used. In addition, Fe_3O_4 can be also deposited on Si substrate with a thin Fe_3O_4 seed layer with a typical thickness of 30 nm.

4.2.3 Characterization

The crystallographic structure of the obtained films was examined using a X-ray diffractometer system with Cu Kα. λ = 1.5418 Å (Bruker D8, Karlsruhe, Germany). X-Ray photoelectron spectroscopy (XPS; VGESCALAB 200i-XL) was used in the study of the film composition and ionic states. Transmission electron microscopy (TEM) images were obtained with a JEOL 2010 microscope at an acceleration voltage of 200 kV. Energy dispersive spectroscopy (EDS) attached with the SEM and TEM was used for elemental analysis. Magnetic properties were detected by vibrating sample magnetometer (VSM: Lakeshore, Mode 665) and superconducting quantum interference device (SQUID; Quantum Design, MPMS, XL-5). The electrical properties were investigated using Hall effect system (HL5500PC, BIO-RAD) by four-point probe method and Physical Property Measurement System PPMS (PPMS; The Quantum Design PPMS EverCool-II). The relative complex permeability of sample was determined from the scattering parameters measured by a network analyzer (Agilent Technologies E8363B). The optical properties were characterized by photoluminescence spectroscopy with a He–Cd laser (325 nm) as the source of excitation.

4.3 Investigation on Fe_3O_4 film

4.3.1 Structure characterization

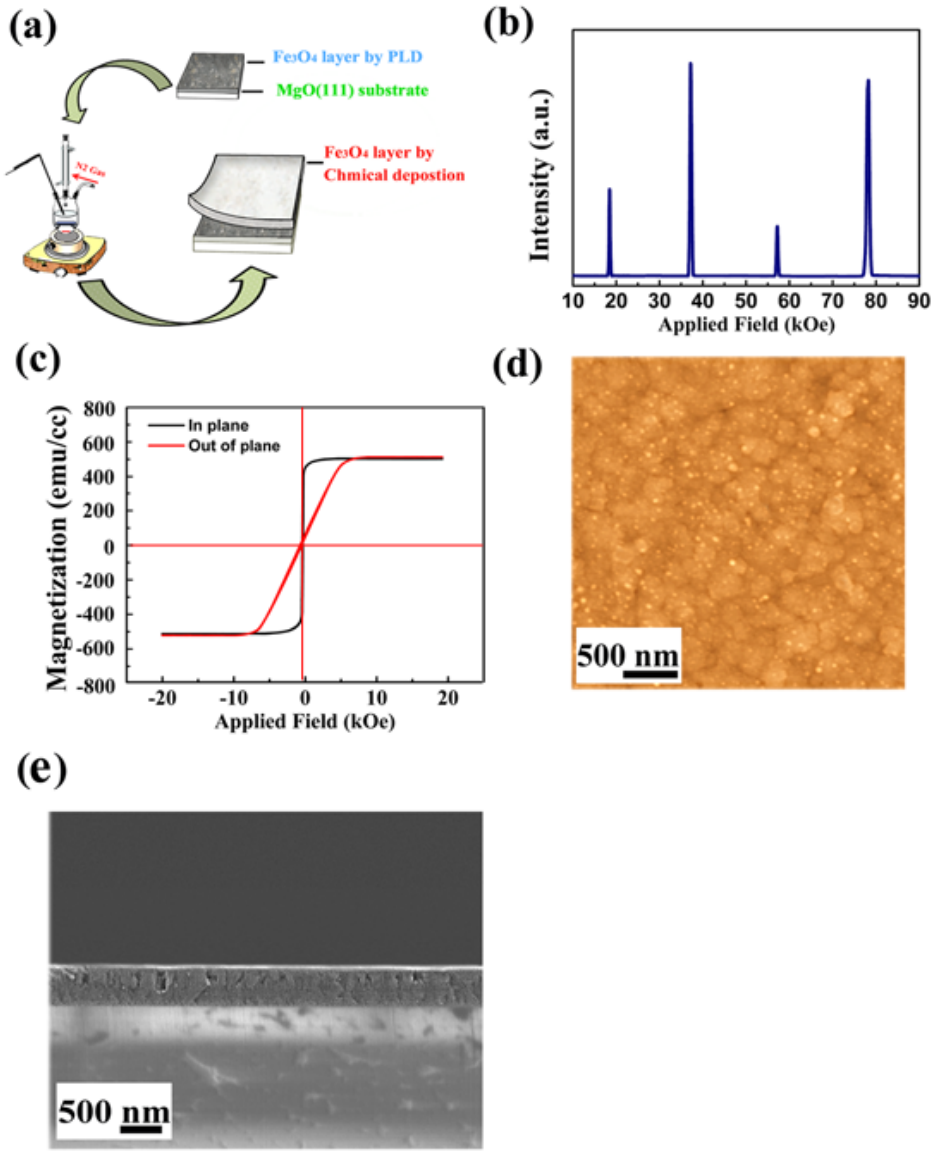

Figure 4. 1. (a) A schematic diagram of deposition of Fe_3O_4 on Si Substrate, (b) X-ray diffraction θ-2θ scans of Fe_3O_4 film on Si Substrate, (c) The in-plane and out-of-plane hysteresis loops of Fe_3O_4 film, (d) Typical surface AFM image, (e) Cross-section of SEM micrograph of 0.5um Fe_3O_4 film.

As reported in our previous publication, [45] ZnO can be grown on ZnO seed layer by hydrothermal process. In this work, our first exploration was the

deposition of Fe_3O_4 on Fe_3O_4 seed layer on Si substrate by thermal decomposition. The fabrication procedure is illustrated in Figure 4.1 (a). The 20 nm Fe_3O_4 seed layer has a (111) texture after deposition by pulsed laser deposition (PLD). Figure 4.1(b) shows the XRD plot of the as-deposited Fe_3O_4 film after thermal decomposition. The XRD peaks in the pattern are corresponding to Fe_3O_4 {111} family, indicating the highly (111) oriented growth (JCPDS 79–0417 file). From the inserted rocking curves, the full width at half maximum (FWHM) of the Fe_3O_4 (222) peak is small of 0.14, indicating the excellent crystallographic quality. The magnetic properties of as-deposited Fe_3O_4 film were studied by VSM. From Figure 4.1(c), the as-deposited Fe_3O_4 film has a coercivity (H_c) below 30 Oe and saturation magnetization (M_s) of 512 emu/cc. In-plane and out-of-plane hysteresis loops have shown that the Fe_3O_4 film needs a relatively higher in-plane magnetic field for saturation due to shape anisotropy. The magnetic measurements showed a good soft magnetic behavior of as-deposited Fe_3O_4 film and the saturation magnetization (Ms) for the synthesized Fe_3O_4 film is slightly higher than bulk value (477 emu/cc). Figure 4.1(d) is a typical surface AFM image of the Fe_3O_4 film; it clearly shows that the film is actually a Fe_3O_4 with very smooth surface. The roughness average (Ra) from the AFM measurement is Ra=1.82 nm, lower than most value reported in the literature using the solution-based techniques. [46-49] The thickness of film could be tuned by adjusting amount of reaction time, the Fe_3O_4 film with thickness from 60 nm to 0.5 um was fabricated in our study and the SEM image of sample in 0.5 um from cross-section view is displayed in Figure 4.1(e).

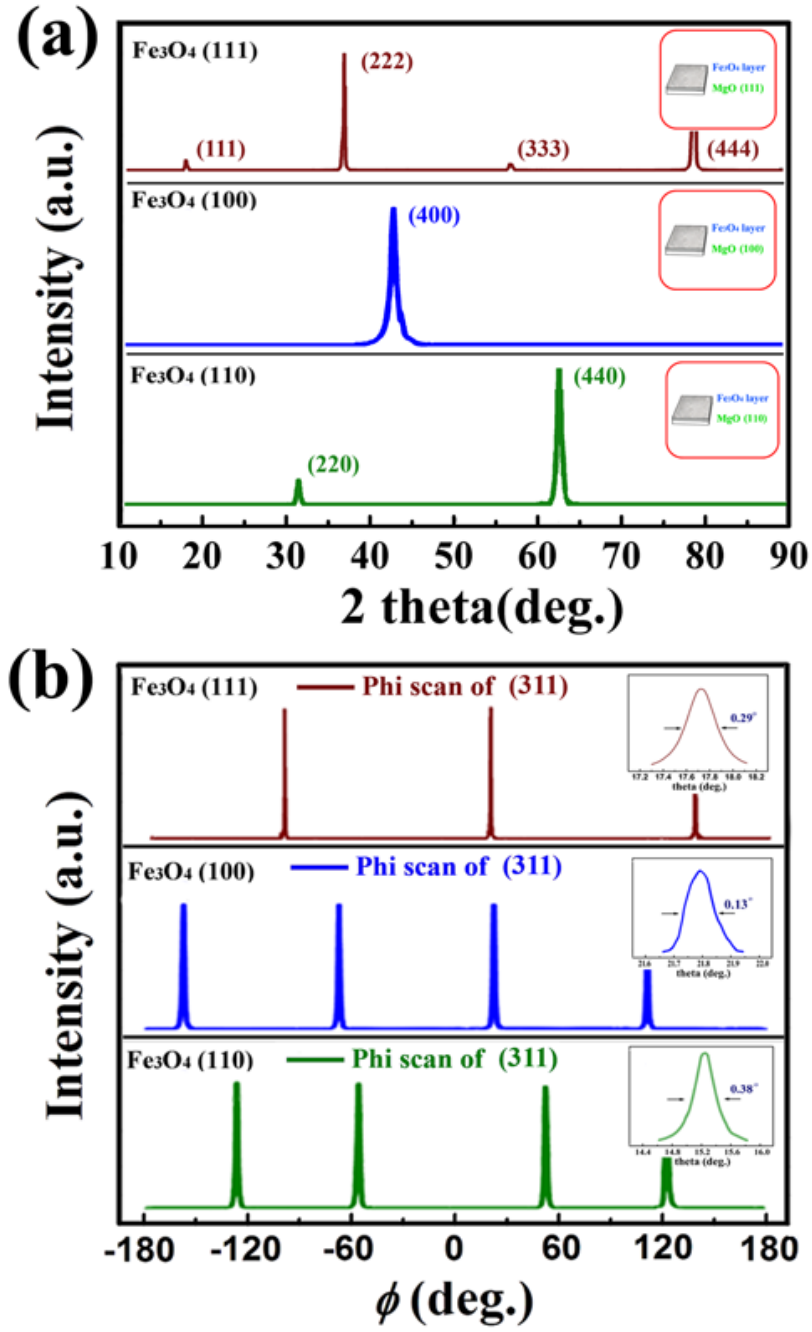

Figure 4. 2. (a) X-ray diffraction θ-2θ scan of Fe_3O_4 film on MgO(111), MgO(100) and MgO(110) substrate, (b) X-ray diffraction φ scan of Fe_3O_4 film on MgO(111), MgO(100) and MgO(110) Substrate. Inset shows the rocking curve.

As reported previously, [50] Fe_3O_4 has an excellent crystallographic matching with MgO, and high-quality epitaxial Fe_3O_4 films can be gown on MgO substrate by physical and chemical vapor deposition techniques. In this work,

we further explored the possibility of growth of Fe_3O_4 directly on MgO substrate. In our experiment, we found that the Fe_3O_4 film can grow on MgO substrate without Fe_3O_4 seed layer. From XRD plots (Figure 4. 2(a)), the Fe_3O_4 film deposited on MgO(111), MgO(100) or MgO (110) substrates have excellent epitaxial growth. The epitaxial crystallographic relationship between Fe_3O_4 and MgO was further studied by φ scans. As shown in Figure 4. 2(b), the φ scans performed on Fe_3O_4 (311) plane shows threefold symmetry, fourfold symmetry and non-symmetry patterns for Fe_3O_4 (111), Fe_3O_4 (100) and Fe_3O_4 (110) films respectively, indicating epitaxial growth of Fe_3O_4 on MgO. The inserts of Figure 4. 2(b) are the rocking curves of Fe_3O_4 (222) peak from Fe_3O_4 (111) film, Fe_3O_4 (400) peak from Fe_3O_4 (100) film and Fe_3O_4 (220) peak from Fe_3O_4 (110) film. The measured full width at half maximum (FWHM) was 0.29°, 0.18°, and 0.38°, respectively, confirming the good epitaxial alignment of Fe_3O_4 on the MgO substrates.

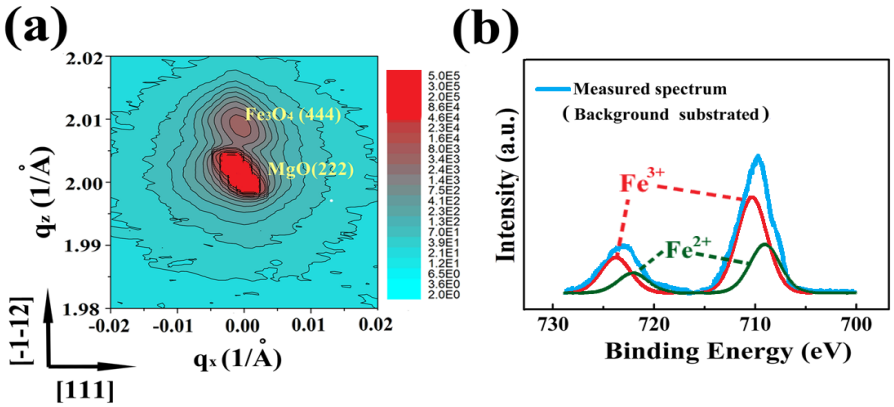

Figure 4. 3. (a) Reciprocal space mapping of the (111) Fe_3O_4 film, (b) Fe 2p core level of XPS spectra.

In order to further understand the epitaxial nature of as-deposited Fe_3O_4 films, the Fe_3O_4 (111) film was chosen and evaluated by reciprocal space mapping (RSM). Two well-resolved peaks corresponding to MgO (222) and Fe_3O_4 (444) are clearly shown in the map (Figure 4.3(a)), which reveals strong epitaxial crystallographic relationship between Fe_3O_4 and MgO (111) substrate. In addition, the centers of diffraction peaks of MgO (222) and Fe_3O_4 (444) align well along the same axis. This observation suggests (111) axis-oriented Fe_3O_4 was coherently grown on the MgO substrate. The typical XPS spectrum of the Fe 2p core level is displayed in Figure 4.3b. The binding energies of Fe $2p_{3/2}$ and Fe $2p_{1/2}$ are located at 710 eV and 723 eV respectively, which are consistent with the values reported previously. [51,52] The fitting procedure yields a Fe^{3+} and Fe^{2+} ratio of (1.9 ± 0.1) and this value agree well with that expected for Fe_3O_4 ($Fe^{2+}Fe_2^{3+}O_4$). Thus, the XPS results confirm the spinel of Fe_3O_4 phase.

4.3.2 Magnetic and electrical properties

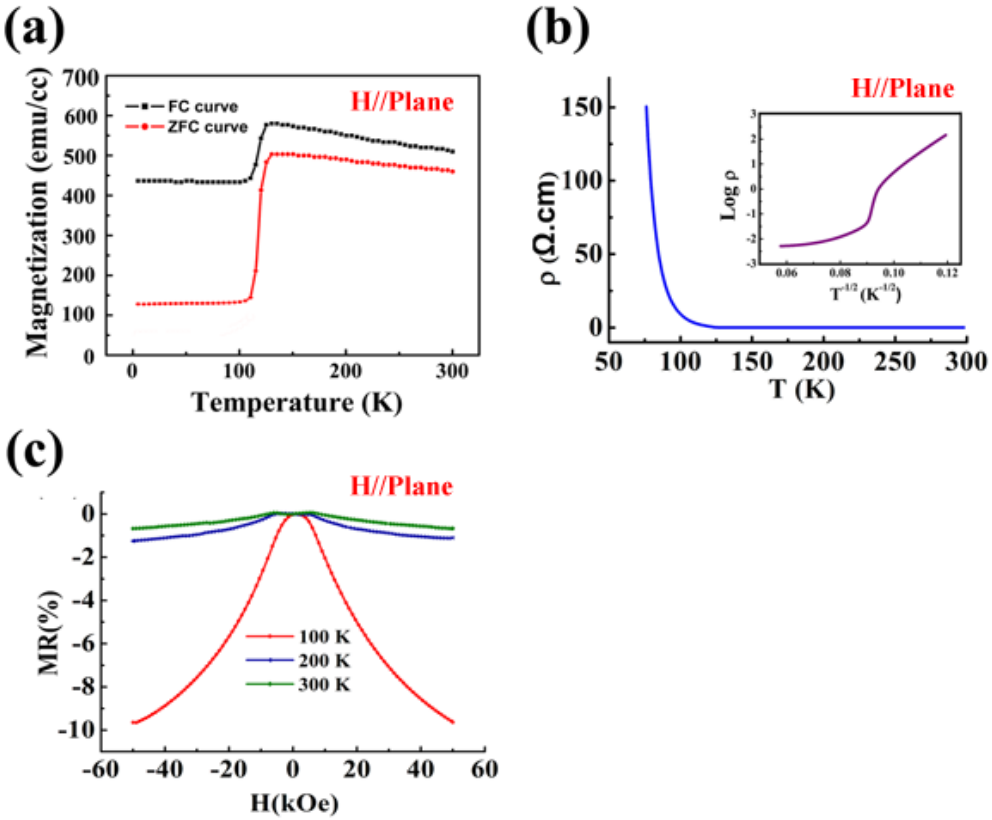

Figure 4. 4. (a) FC and ZFC curve of the (111) Fe_3O_4 film, (b) Resistivity (ρ) vs. Temperature (T) for (111) Fe_3O_4 film while the insert shows the curve of log ρ vs. $T^{-1/2}$, (c) Magnetoresistance MR curves as a function of temperature for (111) Fe_3O_4 film with H parallel to the plane of the film.

The magnetic properties of epitaxial Fe_3O_4 films on MgO substrates were studied by VSM. The results are similar to those as measured for Fe_3O_4 films on Fe_3O_4 seed layer on Si substrate as shown in Figure 4.1. More detailed studies were carried out for the (111) Fe_3O_4 film on MgO (111) substrate as shown in Figure 4.4. The ZFC/FC curves under a constant magnetic field of 500 Oe parallel to the film plane are shown in Figure 4.4 a. A saturation magnetization of M_s = 512emu/cc was measured at 300K. The rapid decrease

of magnetization at 122K shows the Verwey transition, which is consistent with that of bulk value, as expected for spinel Fe_3O_4. [53,54]

The resistivity value at room temperature for the Fe_3O_4 (111) film was measured to be $5.2\times10^{-3}\Omega.cm$, which is close to the bulk value ($4\times10^{-3}\Omega.cm$).[55] Figure 4.4b exhibits the temperature dependence of resistivity of the (111) Fe_3O_4 film. The Verwey transition is found to be 122K as a significant increase in resistivity by two orders as shown in the inset of Figure 4b. Figure 4.4c is the magnetoresistance (MR) curves as function of temperature with magnetic fields parallel to the film plane. At 300K, the MR is around -0.8%, this value decreases slightly and reaches around -1.2% at 200K. Further lower the temperature down to 100K, MR decreases sharply to -10.5% due to the discontinues changes in the thermodynamic quantities (enthalpy and entropy) at Verwey transition temperature which had been discussed in the literature [56]

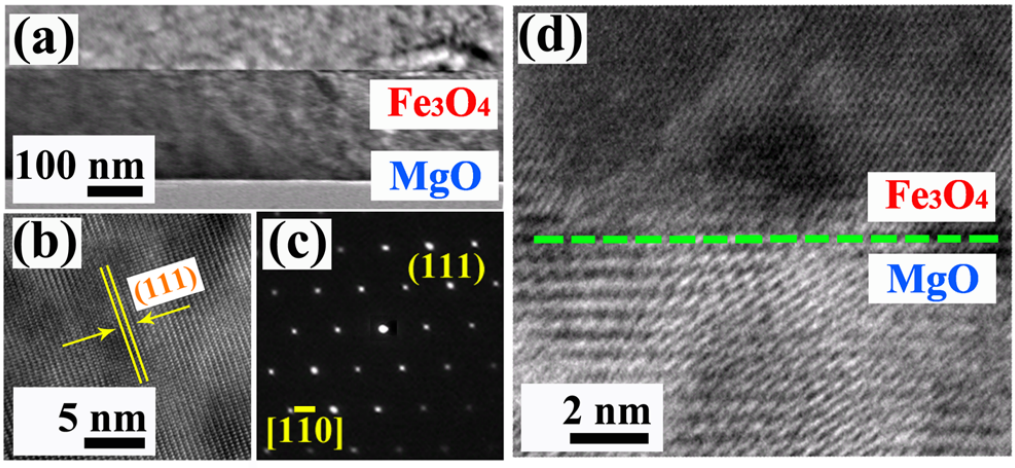

Figure 4. 5. (a) Cross-section of TEM micrograph of (111) Fe_3O_4 film, (b) Magnified TEM image from (111) Fe_3O_4 layer, (c) SADPs taken from (111) Fe_3O_4, (d) HRTEM image viewing around (111) Fe_3O_4/(111) MgO interface.

Figure 4. 5(a) is a bright field cross-section TEM image of Fe_3O_4 film on MgO substrate. The thickness measured from the image is 203nm. The interface and surface of the whole stack is flat, and contrast is uniform through the whole film, indicating a high-quality epitaxial growth of the Fe_3O_4 film. From the TEM image as shown in Figure 4. 5(b), the lattice fringe observed from Fe_3O_4 layer is consistent to the fcc-Fe_3O_4 (111) plane. The corresponding selected area diffraction pattern (SADP) is shown in Figure 4. 5(c). The high resolution TEM image demonstrates a smooth interfacial features between Fe_3O_4 films and the MgO substrate (the green dash line indicates the interface). From the image (Figure 4. 5(d)), we can observe the good lattices in both sides of the interface and no intermediate layers are found in the interfacial region, indicating a chemically clear interface. The dark contrast around the interfacial region implies the lattice strain from the misfit dislocation (δ), which is around 3% calculated using the equation 4.1: [57]

$$\delta = \frac{2(d_1 - d_2)}{d_1 + d_2} \tag{4.1}$$

whereas d_1 and d_2 denote lattice parameter of the Fe_3O_4 and MgO substrate, respectively.

4.3.3 Patterning of Fe_3O_4 film

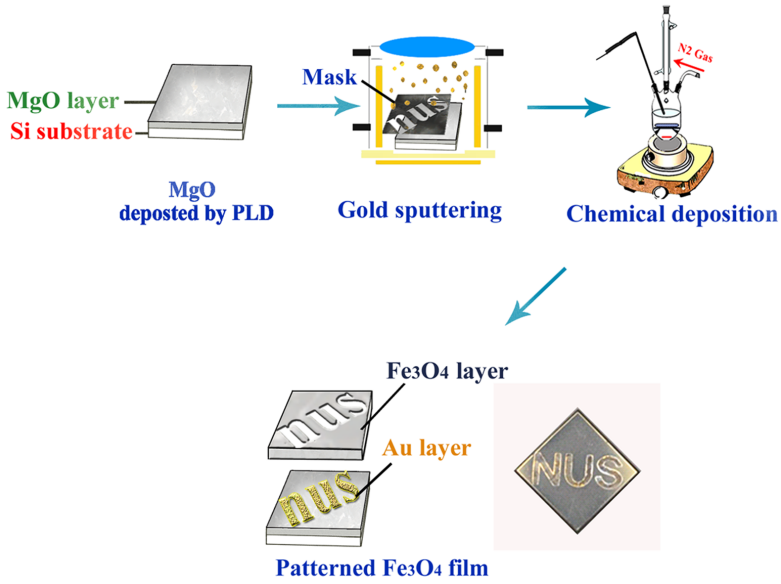

Figure 4. 6. A schematic diagram of process for patterning Fe_3O_4 film by simple masking.

Thick spinel films are promising candidates for engineering applications, such as energy harvester, inductor on chip and MEMS. [12-19] Many of these applications require silicon-technology compatible fabrication process. In this work, we have tested the growth of thick ferrite films on silicon substrate. In addition, it is necessary to develop suitable techniques for patterning for device fabrication. The details of developed patterning process are depicted in the schematic diagram in Figure 4. 6. The Si substrate with a size of (10 mm×10 mm) was deposited with a 50 nm layer of MgO with (111) texture. A patterned gold thin film was sputtered with a patterned mask with NUS logo, as shown in Figure 4. 6. The patterned substrate with NUS logo was placed in the flask and 0.5 um Fe_3O_4 film was deposited by chemical solution-based method. The

XRD result shows the (111) orientation. From the photo displayed in Figure 4. 6, the simple work demonstrates that the as-deposited Fe_3O_4 film could be easily patterned with desired pattern by simple route with mask with a good patterning quality.

4.3.4 Microwave and supercapacitor application

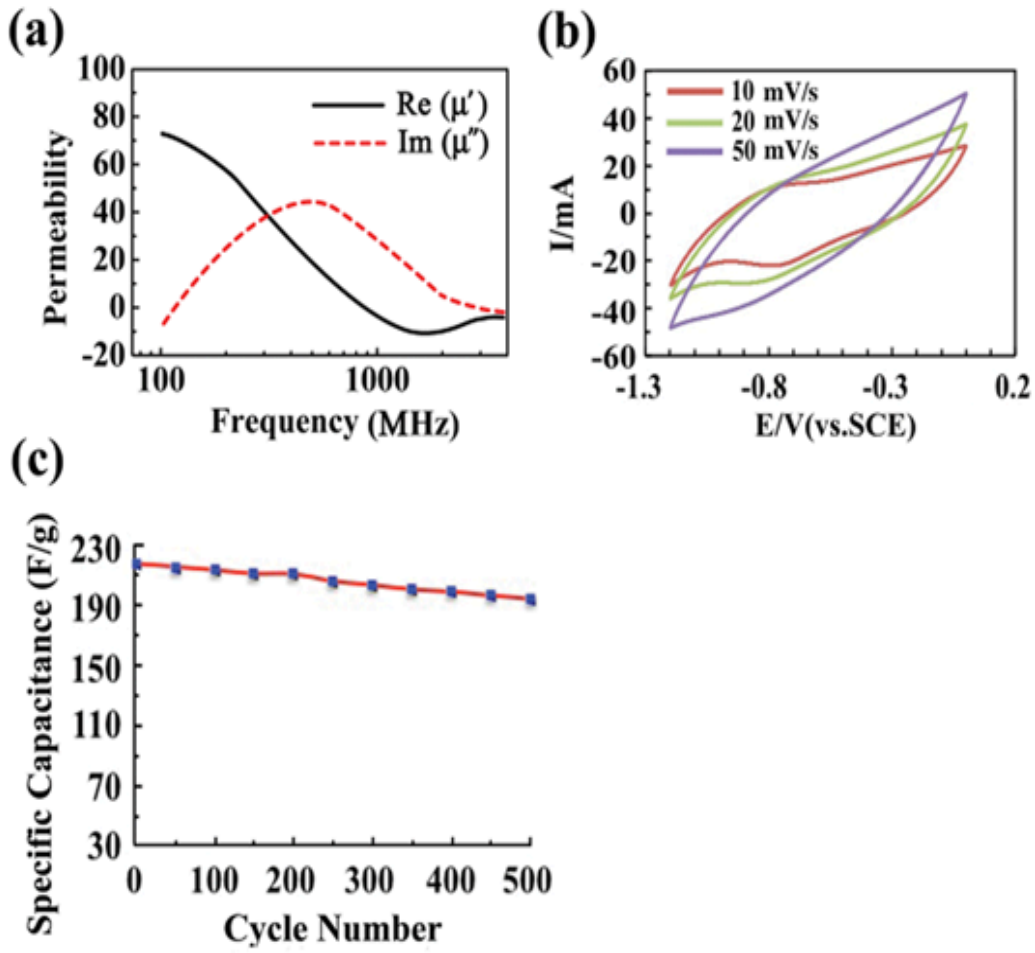

Figure 4. 7. (a) Relative complex permeability real part $\mu'$and imaginary part $\mu''$of the (111) Fe_3O_4 film, (b) The cyclic voltammograms of (111) Fe_3O_4 film electrode at different scanning rates, (c) Cycle life of the Fe_3O_4 film at 12 mA in 1 mol/L Na_2SO_3 solution.

The good quality and epitaxial nature of our thick Fe_3O_4 film deposited by the new technique inspired us to look into its practical applications. Recently, the electromagnetic interference problem has become more important because of the fast development of wireless telecommunications, local area network and high frequency devices. As a result, microwave absorbers as a solution have attracted a great research interests. [58-61] It had been reported that Fe_3O_4 is an excellent absorber of microwave radiation at frequency between 0.5-10 GHz through the process of ferromagnetic resonance. [62] To obtain the microwave absorption properties, we measured the complex permittivity of (111) Fe_3O_4 on MgO substrate by microwave vector network analyzer in the frequency range from 100 to 1300 MHz. From the Figure 4. 7(a), at resonance, the real permeability μ'exhibit the initial value $\mu'_{(h=o)}$ around 73 at 100 MHz. The permeability spectra exhibits a relaxation type as μ' decreases sharply to -11 till 1050 MHz. Moreover, the imaginary part of permeability μ'' curve reveals a broad nature resonance peak, ranging from 100 MHz to 1100 MHz with the resonance frequency about 500 MHz. Thus, the as-deposited Fe_3O_4 illustrates high relaxation losses at low frequency, showing great potential in microwave applications.

Another important application of Fe_3O_4 is supercapacitor. [63-65] Fe_3O_4 thick film with patterned structure is promising as MEMS supercapacitors. Till now, among various transition-metal oxides, oxides of manganese (Mn), nickel (Ni), cobalt (Co), and vanadium (V) have been intensively studied as electrode materials of supercapacitor. In this work, we have tested the (111) Fe_3O_4 thick film electrode for use in supercapacitor. The specific capacitance (C_{sp}) is

defined as equation 4.2 and the interfacial capacitance (C_i) is defined as equation 4.3, [66]

$$C_{sp} = \frac{It}{\Delta Vm} \quad (4.2)$$

$$C_i = \frac{It}{\Delta VA} \quad (4.3)$$

Where I, t, V, m, A are the constant (A), discharge time (s), potential deviation (V), the weight of active materials (g) and A (cm^2) is the area of active material dipped in the electrolyte, respectively.

Figure 4. 7(b) shows the CV curves of Fe_3O_4 electrode in 1M Na_2SO_3 electrolytes. The as-deposited (111) Fe_3O_4 film exhibits a maximum C_{sp} of 213.3 F/g and C_i of 0.16 $F.cm^{-2}$ at 10mV/s between -1.2V and 0V. Supercapacitive properties of Fe_3O_4 films have been studied previously. For example, S.Y. Wang reported the value of C_{sp} 170 F/g in Na_2SO_3 electrolyte for thin film Fe_3O_4 electrodes, [67] Jie Chen et al. reported a C_{sp} of 118.2 F/g in Na_2SO_3 electrolyte for Fe_3O_4 deposited by hydrothermal method. [68] Ruizhi Li reported a C_i of 0.005 $F.cm^{-2}$ in Na_2SO_3 electrolyte for Fe_3O_4 film. [69] The relatively higher specific capacitance and interfacial capacitance of Fe_3O_4 film in our investigation may be due to its good epitaxial nature and relatively high conductivity, resulting in high power density and corresponding high energy density at high rate. [70] In addition, the service life of the Fe_3O_4 film was examined by cycle test. From Figure 4. 7(c), approximately 86.49% of capacitance was remained after 500 cycles, suggesting that the Fe_3O_4 film has the promising application in the electrode of MEMS supercapacitor.

4.4 Investigation on different ferrites film

4.4.1 Magnetic and electrical properties

Spinel ferrites have been found very important uses in industry and other fields. It is well known that Co-ferrite can exhibit hard magnetic behavior, while Ni- and Mn-ferrite can have excellent soft magnetic properties and high resistivity which is required for microwave application because of reduction of eddy current loss. [71-72] In this work, we have studied if different spinel compounds can be realized using the novel fabrication technique and if epitaxy can be maintained.

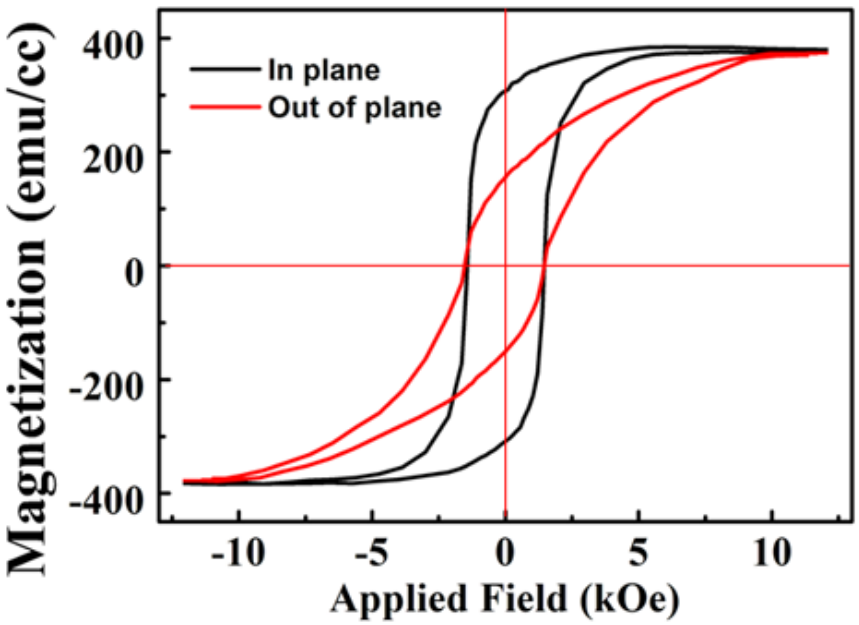

Figure 4. 8. The in-plane and out-of-plane hysteresis loops of $FeCo_2O_4$ film.

	Fe_3O_4	$NiFe_2O_4$	$ZnFe_2O_4$	$MnFe_2O_4$
Ms (emu/cc)	**512**	**495**	**545**	**542**
ρ (Ω·cm)	**5.3×10^{-3}**	**1.6×10^{4}**	**7.2×10^{-2}**	**15**
	$CoFe_2O_4$	**$(Ni,Zn)Fe_2O_4$**	**$(Mn,Zn)Fe_2O_4$**	
Ms (emu/cc)	**380**	**470**	**543**	
ρ (Ω·cm)	**1.3×10^{4}**	**1.4×10^{4}**	**22**	

Table 4. 1. Magnetic parameters and Resistivity values of Fe_3O_4 and other ferrites films.

In this work, we have successfully fabricated different spinel ferrites, including Ni-ferrite, Mn-ferrite, Co-ferrite and Zn-ferrite, as shown in Table 4. 1. Co-ferrite ($CoFe_2O_4$) is a hard ferrite. As shown in Figure 4. 8, the epitaxial Co-ferrite has shown a perpendicular anisotropy with coercivity of 1.5 kOe and a relatively high perpendicular remanence ratio, showing its potential for hard magnetic applications. Enhanced magnetization has been reported by Zn-ferrite. [73] Zn-ferrite thick films prepared by the thermal decomposition method also showed relatively high magnetization of 545 emu/g (corresponding to 0.68 Tesla). In addition, resistivity has been increased from

$5.3x10^{-3}$ Ω·cm to $7.2x10^{-2}$ Ω·cm, showing the potential for soft magnetic applications. Our structural characterization showed that all these thick films in Table 4. 1 have high-quality epitaxy.

As metal-based soft magnets possess high permeability, spinel ferrite soft magnets are mainly used in high-frequency areas (such as microwave magnets). [74-75] For such applications, high resistivity is desired. As it can be seen in Table 4. 1, Mn-ferrite possessed a resistivity of 15 Ω·cm which is much higher than that of Fe_3O_4 ($5.3x10^{-3}$ Ω·cm). Ni-ferrite is expected to have a much higher resistivity. Our thick Ni-ferrite film possessed a resistivity of 1.6 $x10^4$ Ω·cm, which is similar to those reported to bulk Ni-ferrite. [76] It is to note that our Ni-ferrite film has a high saturation magnetization of 495 emu/cc (corresponding to 0.62 Tesla), which is significantly higher than that expected for bulk Ni-ferrite (0.5 Tesla). [77] In this work, we have found out that our Ni-ferrite film can possess a high resistivity (comparable to that of bulk Ni-ferrite), and maintain the saturation magnetization over 0.6 Tesla. This behavior is very promising for commercial application, as high magnetization microwave magnet. The physical origin of high magnetization needs to be further investigated in the near future.

4.5. Conclusions

In summary, we have successfully developed a fabrication process method for epitaxial growth of thick magnetic ferrite films through a simple and economic wet-chemical thermal decomposition. High quality epitaxial Fe_3O_4 thick films have been deposited on MgO, or Fe_3O_4 and MgO seed layer on silicon substrate. Based on the fact that Fe_3O_4 cannot grow on Au, patterned Fe_3O_4 structure can be obtained after Au patterning. The Fe_3O_4 films have shown good properties for microwave and supercapacitor electrode. Different ferrite thick films have been successfully deposited through co-decomposition. Relatively high coercivity has been obtained for Co-ferrite films. High resistivity and enhanced saturation magnetization have been achieved for Ni-ferrite showing its great potential as novel microwave magnets.

REFERENCES:

[1] P. Sebayang, M. Masbah, R. T. Siregar, T. B. Walyo, Adv. Nat. Sci: Nanosci. Nanotechnol. **2011**, 2, 045016.

[2] C. A. Stergiou, V. Zaspalis, CERAM INT. **2015**, 41, 4798.

[3] A. Shahvarpour, C. Caloz, IEEE MTT-S International. **2009**, 09, 25.

[4] D. D. Pollock, Physical Properties of Materials for Engineers, CRC Press, USA **1993**.

[5] H. L. Cai, J. Zhan, C. Yang, X. Chen, Y. Yang, B. Y.Chi, A. Wang, T. L. Ren. J, Nano Mat. **2013**, 2013, 01.

[6] K. Praveena, K. Sadhana, S. Bharadwaj, S.R. Murthy, J. Magn. Magn. Mater. **2009**, 321, 2433.

[7] M. W. Mukhtar, M. Irfan, I. Ahmad, I Ali, M. N. Akhtar, M. A. Khan, G. Abbas, M. U. Rana, A. Ali, M. Ahmad, J. Magn. Magn. Mater. **2015**, 381, 173.

[8] V. G. Harris, A. Geiler, Y. Chen, S. D. Yoon, M. Wuc, A. Yang, Z. H. Chen, P. Hea, P. V. Parimia, X. Zuo, C. E. Pattonc, M. Abee, O. Acher, C. Vittoria, J. Magn. Magn. Mater. **2009**, 321, 2035.

[9] A. Verma, D. C. Dube, J. Am. Ceram. Soc. **2015**, 88, 519.

[10] T. Nakamura, J. Appl. Phys. **2000**, 88, 348.

[11] M. P. Horvath, J. Magn. Magn. Mater. **2000**, 215, 17.

[12] T. S. Chin, J. Magn. Magn. Mater. **2000**, 209, 75.

[13] D. P. Arnold, N. Wang, J. Microelectromech. Sys. **2009**, 18, 1255.

[14] O. Gutfleisch, M. A. Willard, E. Brück, C. H. Chen, S. G. Sankar, J. P. Liu. Adv. Mater. **2011**, 23, 821.

[15] K. Park, S. Xu, Y. Liu, G. T. Hwang, S. L. Kang, Z. L. Wang, K. J. Lee, Nano Lett. **2010**, 10, 4939.

[16] G. Srinivasan, Annu. Rev. Mater. Res. **2010**, 40, 153.

[17] Y. I. Rozenberga, V. Krylovc, G. Belitskya, Y. S. Diamanda, J. Magn. Magn. Mater. **2006**, 305, 357.

[18] M. Sugimoto, J. Am. Ceram. **1999**, 82, 269.

[19] A. G Chynoweth, Science **1976**, 20, 724.

[20] S. Capraro, J. P. Chatelon, H. Joisten, M. Le Berre, B. Bayard, D. Barbier, J. J. Rousseau, J. Appl. Phys. **2003**, 93, 9898.

[21] C. Gatel, E. Snoeck, V. Serin, A. R. Fert, Eur. Phys. J. B. **2005**, 45, 157.

[22] M. Foerster, M. Iliev, N. Dix, X. Martí, M. Barchuk, F. Sánchez, J. Fontcuberta, Adv. Funct. Mater. **2012**, 22, 4344.

[23] G. Catalan, J. F. Scott, Adv. Mater. **2009**, 21, 2463.

[24] A. Bollero, M. Ziese, R. Höhne, H.C. Semmelhack, U. Köhler, A. Setzer, P. Esquinazi, J. Magn. Magn. Mater. **2005**, 285, 279.

[25] Gagan Dixit, J. P. Singh, R.C. Srivastava, H.M. Agrawa, R.J. Chaudhary, Adv. Mat. Lett. **2012**, 3, 21.

[26] R. Nechache, C. Harnagea, S. Li, L. Cardenas, W. Huang, J. Chakrabartty, F. Rosei, Nature Photon. **2015**, 9, 61.

[27] X. Gao, L. F. Liu, B. Birajdar, M. Ziese, W. Lee, M. Alexe, D. Hesse, Adv. Funct. Mater. **2009**, 19, 3450.

[28] H. C. Wu, O. Mauit, C. Ó. Coileáin, A. Syrlybekov, A. Khalid, A. Mouti, M. Abid, H. Z. Zhang, M. Abid, Igor. V. Shvets. Thin Solid Films, **2004**, 459, 187.

[29] Y. X. Lu, J. S. Claydon, Y. B. Xu, S. M. Thompson, K. Wilson, G. vanderLaan, Phys. Rev. B. **2004**, 70, 233304.

[30] S.K. Arora, R.G.S. Sofin, A. Nolan, I.V. Shvets, J. Magn. Magn. Mater. **2005**, 286, 463.

[31] D. M. Lind, S. D. Berry, G. Chern, H. Mathias, L. R. Testardi, Phys. Rev. B. **1992**, 45, 1838.

[32] A.G. Fitzgerald, T.G. May. Thin Solid Films, **1976**, 35, 201.

[33] R. Dattaa, B. Loukyaa, N. Lic, A. Guptac. J. Cryst. Growth. **2012**, 345, 44.

[34] H. Itoh, T. Uemura, H. Yamaguchi, S. Naka, J. Mater. Sci. **1989**, 24, 3549.

[35] A.G. Fitzgerald, R. Engin. Thin Solid Films, **1974**, 20, 317.

[36] Q. X. Jia, T. M. McCleskey, A. K. Burrell, Y. Lin, G. E. Collis, H. Wang, A. D. Li, S. R. Foltyn, Nature Mater. **2004**, 03, 529.

[37] J.Wang, V. A. Pamidi, K. R. Rogers, Anal. Chem. **1998**, 70, 1171.

[38] A. Huang, A. D. Handoko, K. L. Goh, P. K. Pallathadkaa, S. Shannigrahi, CrystEngComm. **2010,**12, 3806.

[39] A. Ghasemia, A. Morisako, X.X. Liu, J. Magn. Magn. Mater. **2008**, 320, 2300.

[40] M. Sedlář, V. Matějec, T. Grygar, J. Kadlecová. CERAM INT. 2**000**, 26, 507.

[41] T. A. Sorenson, S. A. Morton, G. D. Waddill, A. Switzer, J. Am. Chem. Soc. **2002**, 124, 7604.

[42] S. M. Baber, Q. Lin, G. Zou, N. Haberkorn, S. A. Baily, H. Wang, Z. X. Bi, H. Yang, S. G. Deng, M. E. Hawley, L. Civale, E. Bauer, T. M. McCleskey, A. K. Burrell, Q. X. Jia, H. M. Luo, J. Phys. Chem. C. **2011**, 115, 25338.

[43] H. Y. Si, W. L. Lub, J. S. Chen, G. M. Chow, X. G. Suna, J. Zhaoa, J. Alloy. Compd. **2013**, 577, 44.

[44] L. Fei, M. Naeemi, G. F. Zou, H. M. Luo, Chem. Rec. **2013**, 13, 85.

[45] T. Li, H. M. Fan, J. B. Yi, T. S. Herng, Y. W. Ma, X. L. Huang, J. M. Xue, J. Ding, J. Mater. Chem. **2010**, 20, 5756.

[46] Ala'eddin A. Saif, N. Ramli, P. Poopalan, Jordan. J. Phys. **2010**, 3, 61.

[47] J. X. Liu, D. Z. Yang, F. Shi, Y. J. Cai, Thin Solid Films, **2003**, 429, 225.

[48] J. Sengupta, R.K. Sahoo, K.K. Bardhan, C.D. Mukherjee, Mater. Lett. **2011**, 65, 2572.

[49] N.J. Tanga, b, W. Zhonga, H.Y. Jianga, X.L. Wua, W. Liua, Y.W. Dua, J. Magn. Magn. Mater. **2004**, 282, 92.

[50] X.L. Huang, Y. Yang, J. Ding, Acta. Materialia. **2013**, 61, 548.

[51] X. B. Liu, H. B. Lu, M. He, L. Wang, H. F. Shi, K, J. Jin, C. Wang, G. Z. Yang, Appl. Phys. **2014**, 47, 105004.

[52] A. Müller, A. Ruff, M. Paul, A. Wetscherek, G. Berner, C. Praetorius, K. Fauth, U. Bauer, M. Przybylski, M. Gorgoi, M. Sing, R. Claessen, Thin Solid Films, **2011**, 520, 368.

[53] X. H. Liu, A. D. Rata, C. F. Chang, A. C. Komarek, and L. H. Tjeng, Phys. Rev. B, **2014**, 90, 125142.

[54] V. I. Anisimov, I. S. Elfimov, N. Hamada, K. Terakura, Phys. Rev. B, **1996**,54, 4387.

[55] R. Prakash, R. J. Choudhary, L. S. Chandra, N Lakshmi, D. M. Phase, J. Phys.: Condens. Matter. **2007,** 19, 486212.

[56] K. B. Paul, Cent Eur J Phys, **2015**, 3, 115.

[57] Y. X. Chen, C. Chen, W. L. Zhou, Z. J. Wang, J. Tang, D. X. Wang, J. M. Daughton, J. Appl. Phys. **2004**, 95, 7282.

[58] M. G. Han, H. P. Lu, L. J. Deng, Appl. Phys. Lett. **2010**, 97, 1925071.

[59] M. G. Han, W. Tang, W. B. Chen, H. Zhou, L. J. Deng, Appl. Phys, **2010**, 107, 09A9581.

[60] J. L. Xie, M. G. Han, L. Chen, R. X. Kuang, L. J. Deng, J. Magn. Magn. Mater. **2007**, 314, 37.

[61] W. B. Chen, M. G. Han, L. J. Deng, Physica B: Condensed Matter. **2010**, 405 1484.

[62] J. L. Kirschvink, Bioelectromagnetics **1996,** 17, 187.

[63] D. H. Guana, Z. Gao, W. L. Yanga, J. Wang, Y. Yuana, B. Wang, M. Zhang, L. H. Liu, Mat Sci Eng B-Solid **2013**, 178, 736.

[64] J. Chen, K. l. Huang, S.Q Liu, Electrochimica Acta. **2009**, 55, 01.

[65] Y.Yong, Y.Yang, X. Wen, D. Jun, J. Appl. Phys. **2014,** 115, 17A521**.**

[66] P.M. Kulal, D.P. Dubal, C.D. Lokhande, V.J. Fulari, J. Alloys Compd. **2011**, 509, 2567.

[67] S.Y. Wang, K.C. Ho, S.L. Kuo, N.L. Wu, J. Electrochem. Soc. **2006**, 152, A75.

[68] J. Chen, K. L. Huang, S.Q. Liu, Electrochimica Acta. **2009**, 55, 01.

[69] R.Z. Li, X. Ren, F. Zhang, C. Du, J. P. Liu, Chem. Commun. **2012**, 48, 5010.

[70] X. Tang, T. R. Jia, T. Zhai, H. Xia, ACS Appl. Mater.Interfaces, **2015**, 7, 27518.

[71] J. M. D. Coey, Magnetism and Magnetic Materials Hardcover, Cambridge University Press, UK **2010**.

[72] R. S. Turtelli, M. Kriegisch, M. Atif , R. Grössinger, Conf. Ser.: Mater. Sci. Eng. **2014,** 06, 012020.

[73] Y, Yang, X. L. Liu, Y.Yang, W. Xiao, Z. W. Li, D. S. Xue, F. S. li, J. Ding, J. Mater. Chem. C, **2013**, 01, 2875.

[74] A.K. Subramani, K. Kondo, M. Tada, M. Abe, M. Yoshimura, N. Matsushita, Mater Chem Phys. **2010**, 123, 16.

[75] S, Noppakun, Solution Precursor Plasma Spray System, Springer International Publishing, USA **2014**.

[76] R. A. McCurrie, Ferromagnetic Materials: Structure and Properties Academic, Academic, New York, **1994**.

[77] U. Lüders, A. Barthélémy, M. Bibes, K. Bouzehouane, S. Fusil, E. Jacquet, J. P. Contour, J. F. Bobo, J. Fontcuberta, A. Fert, Adv. Mater. **2006**, 18, 1733.

Chapter 5 Chemical synthesis of magnetic FeCo nanoparticle and film

In Chapter 3 and 4, magnetic ferrites nanoparticle and film had been investigated on their synthesis method, structures, properties and applications. In this chapter, we turn to another important class of magnetic Fe-based nanomaterial; Ferrous alloy. Specifically, typical Fe-3d metal alloy FeCo will be studied in detail.

5.1 Introduction

Fe-3d transition-metal alloy have been intensively studied by many researchers because of their promising applications in a wide range of areas, including data storage, medical diagnosis and drug delivery. [1-2] Among all Fe-3d transition-metal alloys, FeCo alloy nanoparticles were of interest in this context for their high saturation magnetization which is approximately four times higher than that of iron oxide. [3-5]There is no doubt that such a high magnetization will offer significant advantage of FeCo in many biomedicine utilizations [6-7] and magnetic memory devices. [8-11]

Recently, some synthesis protocols for FeCo nanoparticles had been reported, [12-16] which involved either an expensive, toxic and explosive iron organometallic compound $Fe(CO)_5$ or under a highly reducing protection environment such as H_2 or using a toxic reducing agent such as N_2H_4. It has been reported [3,17,18] that the annealing process can enhance saturation magnetization of FeCo nanoparticles. However, after annealing, the particle size was often larger than 100 nm which restricted them to be used in many

biomedicine applications. For example, the large size particles are likely to cause embolism and in the application of drug delivery, they may be obstructed by endothelial barriers. In addition, most of the synthesis of FeCo thin films have been based on vacuum deposition, including pulse laser deposition (PLD), [19-22] Molecular beam epitaxy (MBE), [23-25] Sputtering [26-30] and so on. However the cost of these techniques is high as the use of high vacuum. Thus, an exploration for alternative method for deposition of FeCo film is necessary.

In this chapter, we have developed a safe and ecofriendly route of synthesizing FeCo alloy nanoparticles. There are no toxic materials involved in the synthesis procedure and no toxic by-products were produced. The whole process is safe. The obtained FeCo nanoparticles were mono-dispersed and size-controlled with high saturation magnetization by optimizing the Fe/Co ratio, concentration of surfactant used and reaction condition. Besides, bcc-FeCo film was deposited on Pt substrate by thermal decomposition and its magnetic properties were investigated.

In this approach, FeO(OH) and Co_3O_4 were chosen as the economic source materials. Oleic acid was used as effective reduction agent and surfactant simultaneously. Oleic acid has been widely employed to synthesize various mono-dispersed oxide and metal nanocrystals [31-37] It has been also demonstrated that oleic acid could behave as a strong reducing agent when the reaction temperature is high enough [38,39] The fabrication procedure for nanoparticle synthesis is showed in Figure 5. 1.

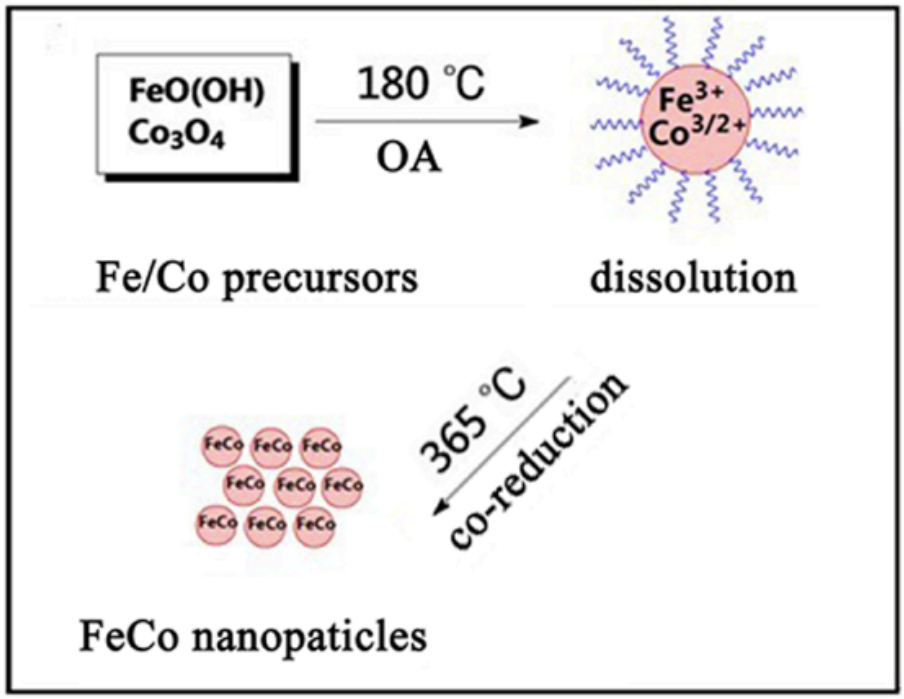

Figure 5. 1. Reaction scheme for the synthesis of FeCo nanoparticles. The iron and cobalt precursors were dissolved at 180°C, then reduced at 365°C to form the FeCo nanocrystals.

5.2 Experimental

5.2.1 Materials and characterization

FeO(OH) (catalyst grade 30-50 mash), oleic acid (OA), TOA (Trioctylamine 98%), poly(isobutylene-alt-maleic anhydride) (PBMA) with molecular weight = 6000 and technical grade 85%, poly(vinylal-cohol) (PVA) with molecular weight = 31000-50000, 1-2 henxadeanediol (technical grade 98%), Tetrehydrafuran (THF 99%) and cobalt(II,III) oxide (Co_3O_4) were purchased from Sigma-Aldrich. Cell counting Kit-8(cck-8) was obtained from DoJunDo. All the reagents were analytical grade and used without further purification.

The crystal phase of the obtained FeCo nanopowders was determined by an advanced diffractometer system (Bruker D8 with Cu Kα 1.5418 Å, Karlsruhe, Germany). Transmission electron microscope (TEM) images were obtained with a JEOL 2010 microscope at an acceleration voltage of 200 kV. Magnetic properties of the obtained nanoparticles were studied by vibrating sample magnetometer (VSM: Lakeshore, Mode 665). The hydrodynamic diameters of the particles were measured by Zetasizer Nano series - Malvern. Energy dispersive spectroscope (EDS) attached with the SEM was used for elemental analysis.

5.2.2 Synthesis of FeCo nanoparticles

Firstly, mixtures of FeO(OH) and Co_3O_4 in desired proportions with suitable amount of solvent TOA (Trioctylamine) were loaded into a three neck flask, and then the mixture was dehydrated at 180°C for 1h under a flow of argon. After that, the solution was quickly heated to 365°C while stirring using a stirring bar and aged for 4 hours. During the process, we observed that the solution containing Fe and Co ions turn rapidly into muddy black when reaching the refluxing temperature. Lastly, the resulting black solution was cooled to room temperature and washed several times with ethanol and hexane followed by centrifugation at 10000 prm. Half of product obtained was dispersed into hexane while the rest was dried overnight for further characterization. The same synthesis procedure was applied for the single precursors FeO(OH) and Co_3O_4 separately, after dehydrated at 180°C, the solution is heated up to 365°C for 4 hours, and then the products were rinsed for characterization.

5.2.3 Phase transfer of hydrophobic FeCo nanoparticles

The hydrophobic FeCo nanoparticles were transferred into aqueous phase according to the reported procedure. [40] At first, PBMA and specific amount of the as-synthesized FeCo particles were dissolved in chloroform individually before we mixed them together. After that, the solution was emulsified with water (10vol excess, 1 wt% PVA as stabilizer) for 5 mins by an ultrasonic homogenizer (SONICS VCX 130PB) at 20 kHz frequency and 60% amplitude. Lastly, transferred the mixture to an open glass beaker and heated it to 50°C with rapid stirring by magnetic bar to allow the chloroform to evaporate. The as-prepared colloids centrifuge at 8000 rpm for 10 min for purification and then redisposed in water/methanol (50: 50) at least two times.

5.2.4 Vitro cytotoxicity

The NIH/3T3 fibroblast cells were used for assessing the cytotoxic effect of the prepared FeCo@PBMA at different concentration .The NIH/3T3 fibroblast cells were grown in DMEM (Dulbecco's Modified Eagle Medium) culture growth medium (10% bovine calf serum) in incubator at 37 °C in a 5% CO_2 humidity environment. The cells with the concentration of 7.5×10^4 cells per mL (0.1 mL) were then transferred to a 96-well cell culture plate (TPP 96) by pipet and incubated again overnight. After that, 20ml of prepared FeCo@PBMA with predetermined concentration was added into each well and moved TPP 96 back to incubator. 24 hours later, 10 mL cell counting kit-8 (CCK-8) was added, following by 4 hour incubation before the cell viability test. Absorbance readings were analyzed spectrophotometrically at 355 nm using a FluoStar Optima microplate reader.

5.2.5 Fabrication of FeCo film

Firstly, substrate was placed at a three-neck flask, then desired proportions of FeO(OH), Co_3O_4 and 1-2 henxdeaediol with suitable amount of TOA solvent and OA were loaded inside. After glass separator and magnetic bar were set, the mixture was dehydrated at 180 °C for 1 hour under a flow of argon and then quickly heated to 300 °C for 3 hours. At the refluxing temperature, it was found that the solution turned into muddy black. After the black solvent was cooled to room temperature, the substrate was took out from the flask and washed 3 times with hexane in sonicator.

5.3 FeCo nanoparticle

5.3.1 Structure and magnetic properties of FeCo and by-products

	Fe/Co molar ratio in metal precursors (FeO(OH)/ Co_3O_4)	Fe/Co molar ratio from EDS analysis	Reaction time	Surfactant (Oleic acid)
Sample 1	Single FeO(OH)	1	4 hours	0.013 mol
Sample 2	6:1	0.86/0.14	4 hours	0.013 mol
Sample 3	6:2	0.73/0.27	4 hours	0.013 mol
Sample 4	6:3	0.68/0.32	4 hours	0.013 mol
Sample 5	6:4	0.57/0.43	4 hours	0.013 mol
Sample 6	6:6	0.48/0.52	4 hours	0.013 mol
Sample 7	6:3	0.66/0.34	4 hours	0.026 mol
Sample 8	Single Co_3O_4	0	2 hours	0.013 mol
Sample 9	Single Co_3O_4	0	3 hours	0.013 mol
Sample 10	Single Co_3O_4	0	4 hours	0.013 mol

Table 5. 1. The Fe/ Co molar ratio of each sample according to the precursor**'**s ratio and EDS analysis as well as their respective reaction conditions.

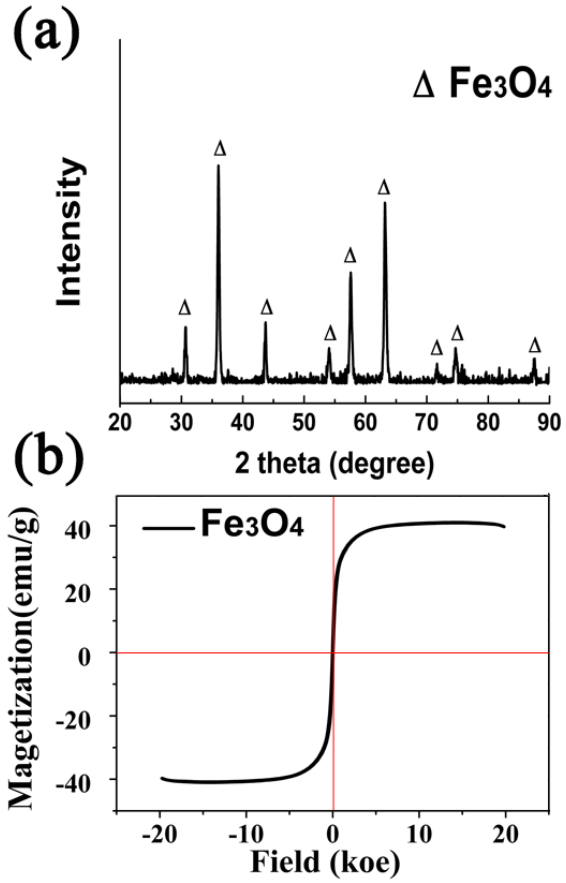

Figure 5. 2. (a) XRD pattern of Sample 1 (Fe_3O_4), (b) Magnetization loops for Sample 1.

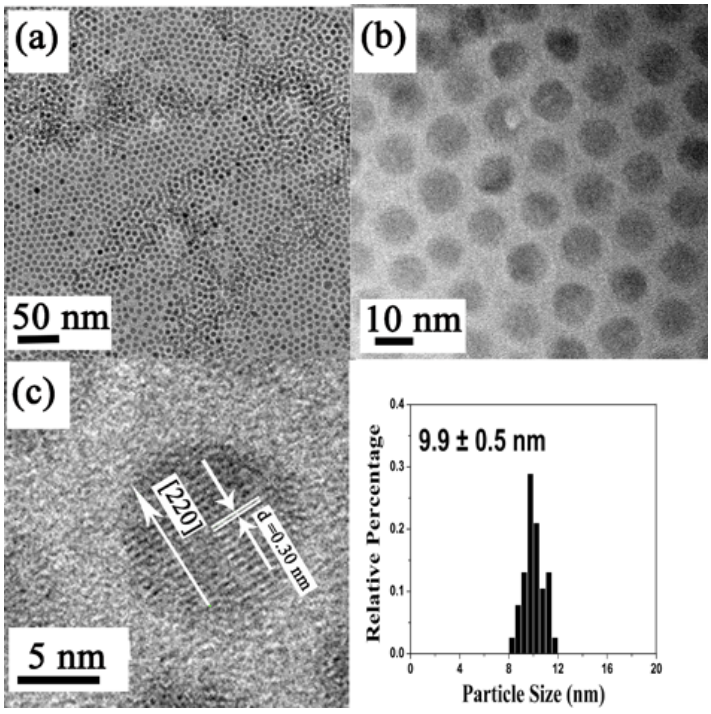

Figure 5. 3. (a) and (b) morphology images of Sample 1 from TEM, (c) The high resolutionTEM image indexed as the [220] plane of Fe_3O_4 and the histogram of size distribution on the right side.

The Sample 1 (Fe_3O_4 nanoparticles) was synthesized with the single precursor FeO(OH). Figure 5. 2(a) showed X-ray diffraction pattern of the resulting product. The sharp peaks matched well with those standard data for Fe_3O_4 (JCPDS 190629). [41] Spherical well-dispersed nanoparticles with average particle size = 10nm were observed in the TEM images (Figure 5. 3(a) and Figure 5. 3(b)) and from the HRTEM image Figure 5. 3(c). The nanostructures were crystalline as the lattice fringes could be clearly observed which responds to the [220] plane systems of spinel-structured Fe_3O_4. The magnetic properties were characterized using VSM at room temperature with saturation magnetization about 40emu/g.

The bcc-FeCo nanoparticles were synthesized by adding Co_3O_4 precursor and Fe/Co ratio was controlled by varying the initial molar ratio of the metal precursors of FeO(OH) and Co_3O_4. The elemental composition of as-synthesized nanoparticles was confirmed with EDS analysis and the results were listed in Table 5.1. The reaction time was four hours because we observed that Co^{2+} that is reduced from Co_3O_4 precursors would convert to CoO phase if the aging time is less than 4 hours.

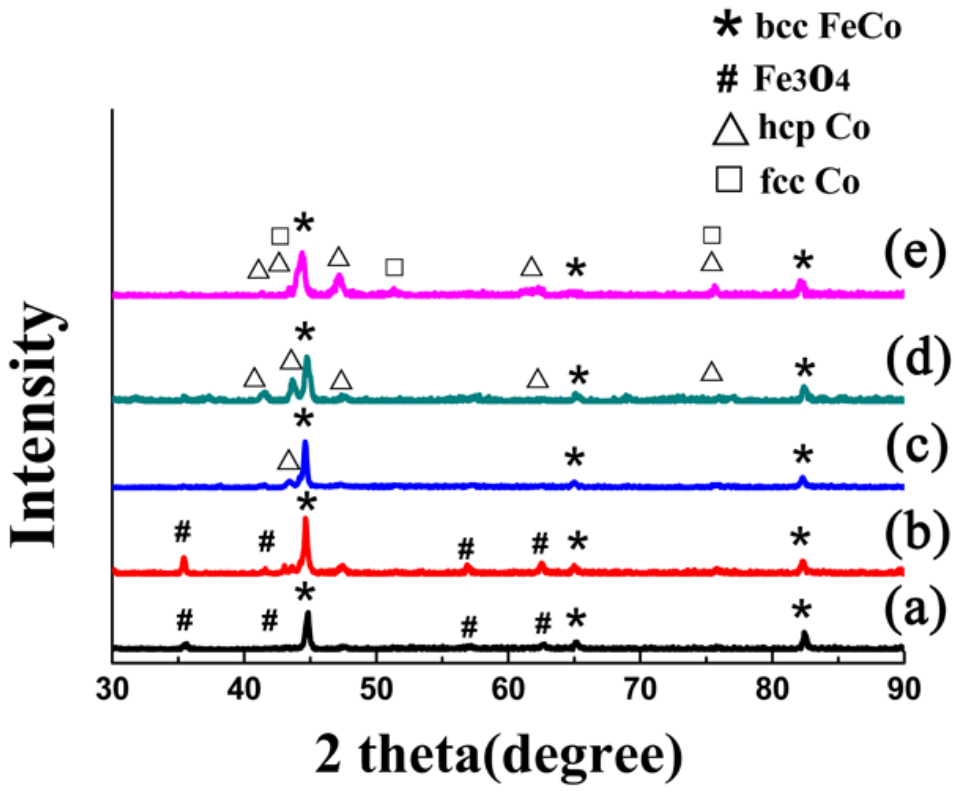

Figure 5. 4. XRD pattern of as-prepared sample with different Fe/Co ratio a 6:1; Sample 2, b 3:1; Sample 3, c 2:1; Sample 4, d 3:2; Sample 5, e 1:1; Sample 6.

XRD patterns of FeCo nanoparticles with different Fe/Co ratios are plotted in Figure 5. 4. In all plots in Figure 5. 4, we observed the bcc-FeCo crystal planes of (110) (200) (211) that are corresponding to the peak indexes at 44.82°, 65.00°, 82.60°(JCPDS card no.000441433). [42] The XRD patterns of Sample 2 and Sample 3（Figure 5. 4(a) and 5. 4(b)） indicated the presence of metallic Fe and Fe_3O_4 peaks. When Fe/Co precursor ratio increased to 2:1 and 3:2, no iron oxide phase was observed. These results imply that the presences of Co ions can promote the reduction of $Fe^{2+, 3+}$ ions into metallic state Fe^0. In terms of the XRD pattern of Sample 5 (Figure 5. 4(d)), hcp- Co peaks appeared and if we further tune the ratio, the coexistence of hcp and fcc- Co

peaks were observed from Sample 6 (Figure 5. 4(e)). However, a small amount of hcp-Co phase is detected in the XRD pattern of Sample 4.

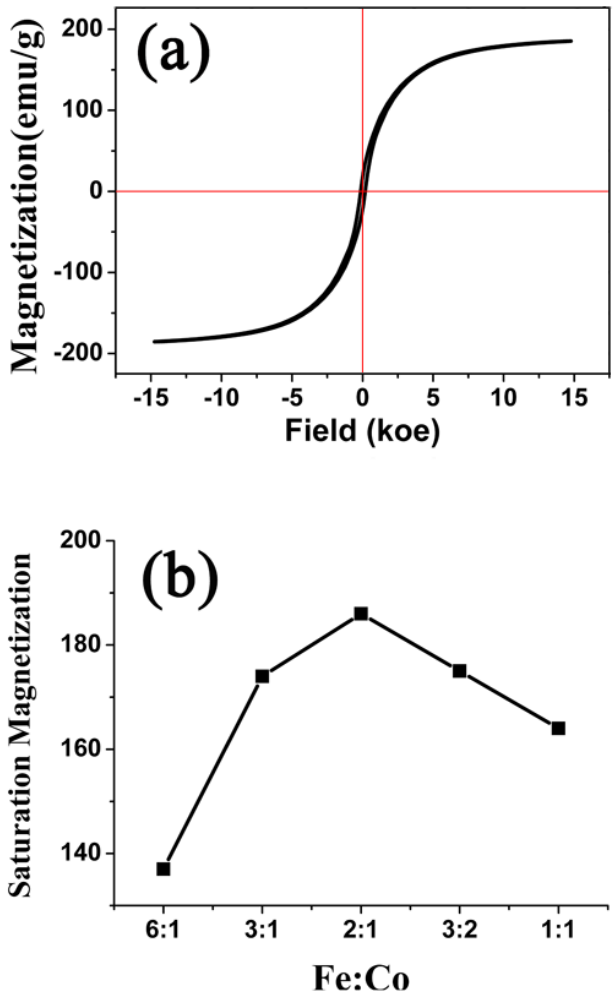

Figure 5. 5. (a) Room temperature M-H loop of Sample 4, (b) The saturation magnetization trend as function of Fe/Co ratio.

Magnetic properties of these particles were composition dependent. From the VSM results (Figure 5. 5(a) and 5. 5(b)), it was illustrated that saturation magnetization is 135emu/g for Sample 2, probably due to the presence of iron oxide phases (Fe_3O_4). Saturation magnetization increased with Co content and reached the maximum of 187 emu/g for Sample 4 with a Fe-Co composition of

$Fe_{0.68}Co_{0.32}$. A further increase in Co concentration led in decrease in saturation magnetization. Sample 6 with a Co concentration of 52% has saturation magnetization to be 165emu/g. As saturation magnetization decreased, we didn't prepare FeCo nanoparticles with even higher Co concentrations. In this work, detailed study was carried out for the optimized sample - Sample 4.

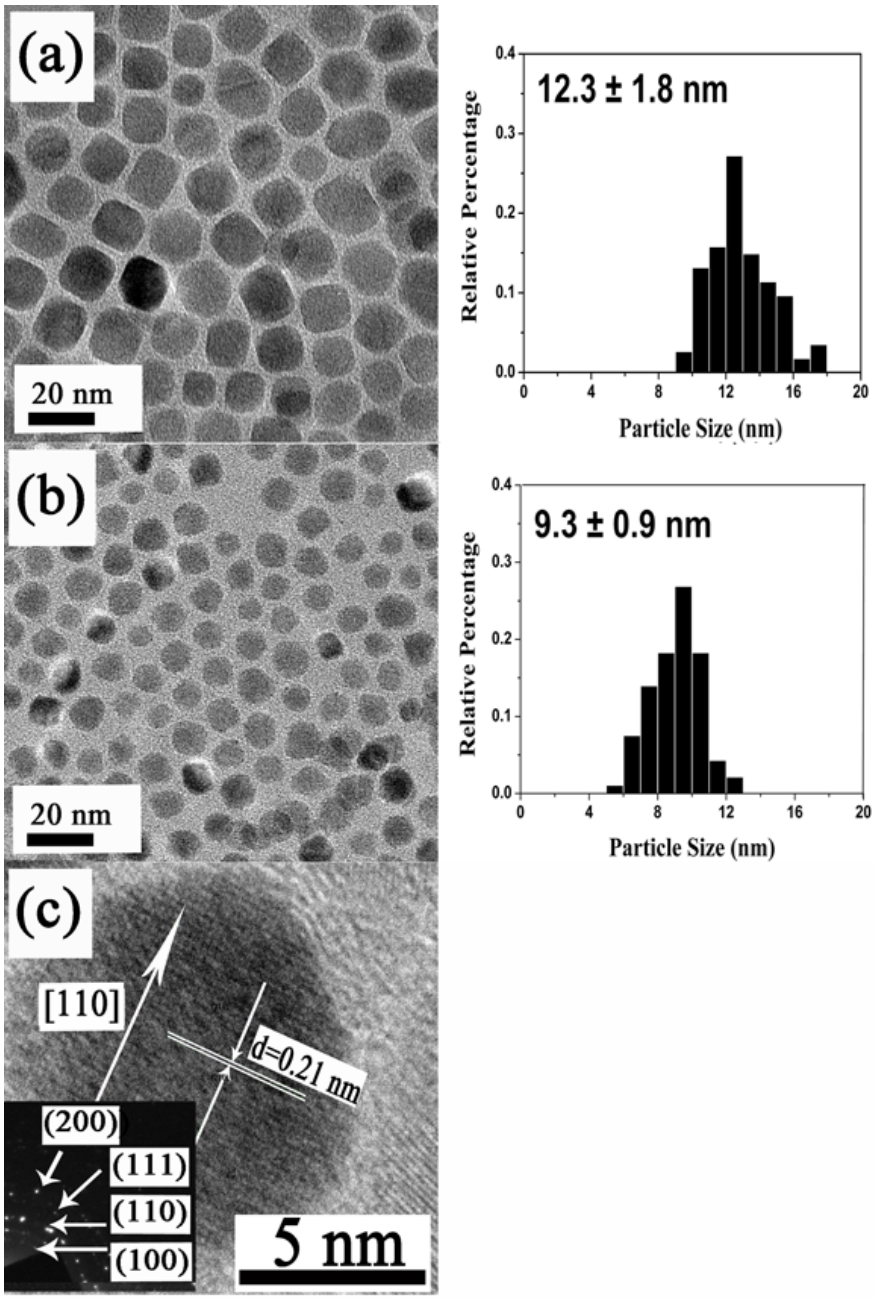

Figure 5. 6. TEM images of FeCo nanoparticles with different size (a) 12.3nm; Sample 4, (b) 9.3nm; Sample 7, the size distribution histograms are on the right side, (c) HRTEM image of the prepared 12.3nm FeCo nanoparticles and inset is an electron diffraction pattern of the selected area, the four rings labeled with miller indices are correspond to the expected FeCo pattern.

The size of nanoparticles was dependent on the amount of oleic acid (OA). From the TEM analysis Figure 5. 6(a) and 5. 6(b), the Sample 4 and Sample 7 were mono-dispersed with an average size of 12.3nm and 9.3nm, respectively. The decrease of the nanoparticle size was the result from the double amount of the surfactant - oleic acid. Saturation magnetization of Sample 7 was nearly 20% less than that of Sample 4. A further increase in oleic acid caused serious aggregate and further decrease in magnetization. The high-resolution TEM (HRTEM) micrograph image (Figure 5. 6(c)) of the Sample 4 revealed the 0.2 nm lattice fringe distance, corresponding to the known value of interplanar spacing for the [110] planes of FeCo alloy, further confirming our XRD results.

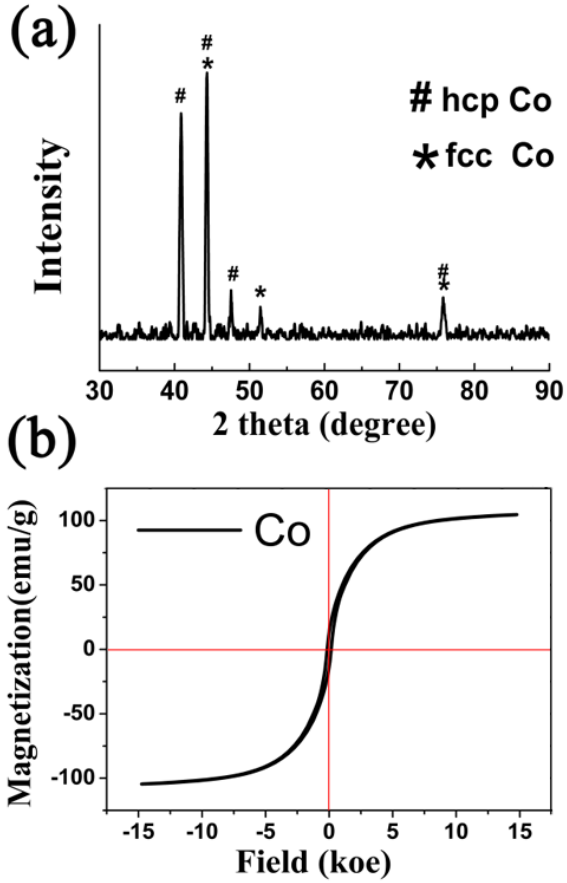

Figure 5. 7. (a) XRD pattern of synthesized mix hcp and fcc-Co; Sample 10, (b) Vibrating sample magnetometer plot.

As discussed previously, we could only obtain Fe_3O_4 if only Fe precursor – FeO(OH) was used. The presence of Co ions can promote reduction of Fe^{2+} and Fe^{3+} into metallic Fe^0. Maximum saturation magnetization was obtained when Co concentration reached 30-35%. A further increase in Co led in reduction of magnetization accompanied by fcc- and hcp-Co. Therefore, it is also interesting to study if only the Co precursor (Co_3O_4) was used as the starting material. As shown in Figure 5. 7(a), fcc and hcp-Co phases were present if Co_3O_4 was used as the only precursor. VSM results (Figure 5. 7(b)) showed that saturation magnetization values (to be 88 emu/g) were much

lower than that of bulk-Co. [43] The composition was further confirmed by the high resolution TEM (Figure 5. 8(e)). HRTEM displayed two different kinds of lattice fringe detected in the particles were consistent with the fcc-Co (111) and (200) planes. The rings observed in electron diffraction pattern matched with both fcc-Co pattern and hcp-Co pattern. The low saturation magnetization of the Sample 10, possibly because of the oxidation during drying process before the VSM test. These nanoneedles may be reactive because of larger surface area.

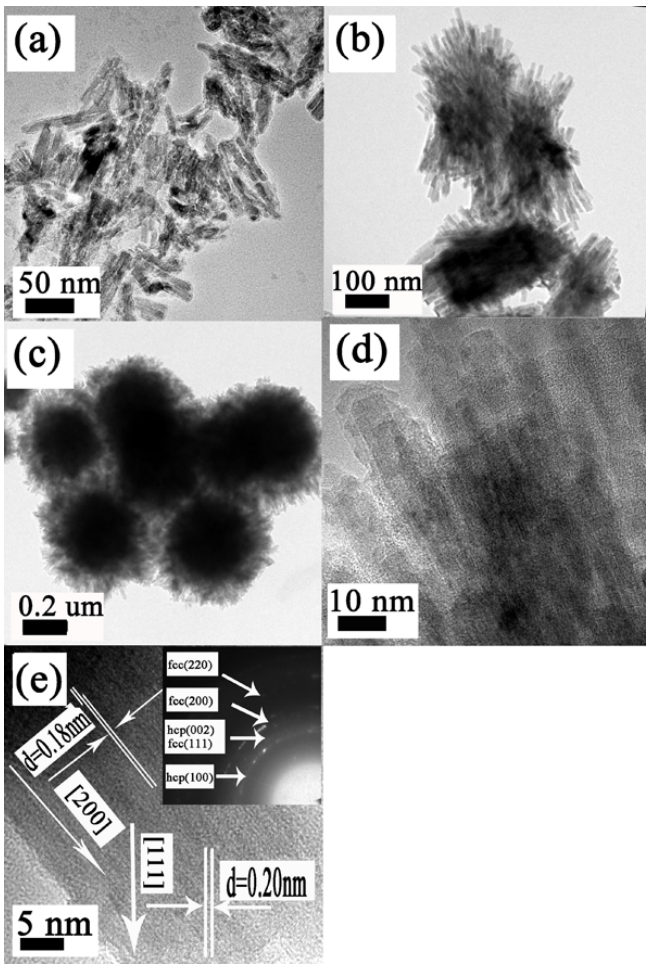

Figure 5. 8. Typical TEM image of Co nanoparticles with different reaction time (a) 2 hours; Sample 8, (b) 3 hours; Sample 9, (c) 4 hours; Sample 10 and (d) magnified view of Sample 9, (e) high resolution of TEM image of Sample 10 and the insert is the electron diffraction pattern of mix fcc and hcp-Co nanoparticles.

A series of products Sample 8, Sample 9 and Sample 10 synthesized with 2, 3 and 4 hours aging time were investigated and from the TEM images, a systematic evolution of hairy ball like morphology was observed. With 2 hours reaction time, the Sample 10 was in the form of Co nanoneedles with 100 nm in length and was coated with a layer of surfactant OA as showed in Figure 5. 8(a). From the TEM image of Sample 9, the nanoneedles grown longer and started to intersect each other (Figure 5. 8(b)), forming the flower bouquet shape over 500 nm. At the last stage, the hairy ball Co nanoparticles were observed in the image of Sample 10 with the aging time of 4 hours by assembling of nanoneedles in various directions (Figure 5. 8(c)). This self-assembly process was similar to what reported by [44] and the particles that form assembly were called as superparticles, however, the size of assembly ball nanoparticles in report were in micron level while in my study, the as-synthesized hairy ball-shape Co nanoparticles with the diameter around 0.5um.

5.3.2 Cytotoxicity test

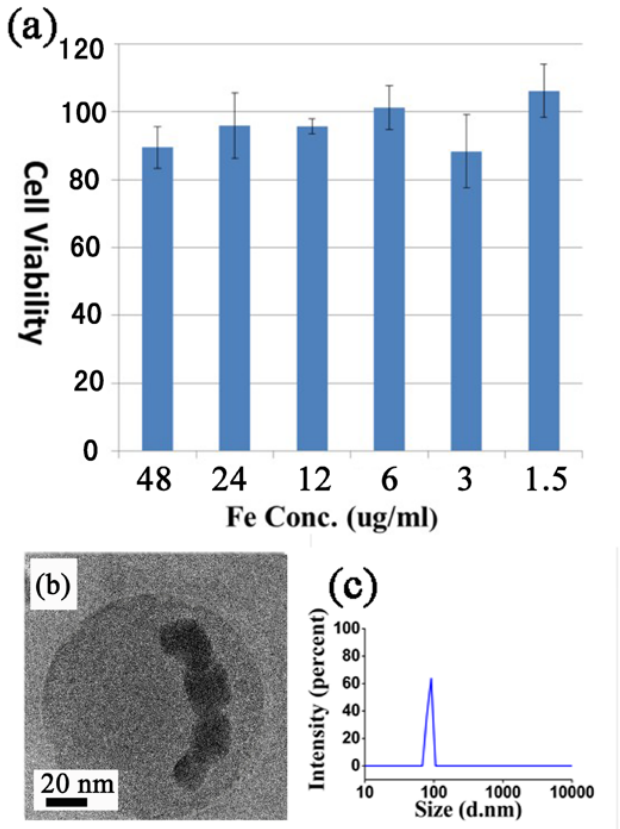

Figure 5. 9. (a) Dose-dependent viability evaluation of NIH/3T3 Cells treated with nanoparticles, (b) TEM image of FeCo@PBMA dispersed in ethanol and dried on the copper grid, (c) DLS plot of nanoparticles.

The as-prepared FeCo nanoparticles were hydrophobic because of immobilization of oleic acid on the surface via carboxylic acid group. The hydrophobic OA-coated FeCo nanoparticles were converted into hydrophilic by coating with PBMA. Typical HRTEM (Figure 5. 9(b)) indicated that the obtained FeCo@PBMA nanoparticles were well dispersed in the water and the diameter observed was around 70 nm. In the meantime, the average size of the nanoparticles of FeCo @PBMA characterized by DLS measurement(Figure 5. 9(c)) was nearly 85 nm which was larger than that observed under electron microscope, presumably because of the swelling of the nanogels in the wet

state as compared to the dry state[24]. From the cell viability image Figure 5. 9(a), the prepared FeCo@PBMA showed no cytotoxicity within in the range concentrations. Thus the as-synthesized FeCo nanoparticles along with the PBMA layer possessed high bio-compatibility and could be termed as a promising material for future biomedicine application like drug delivery and biosensor.

5.4 FeCo film

5.4.1 Structure characterization

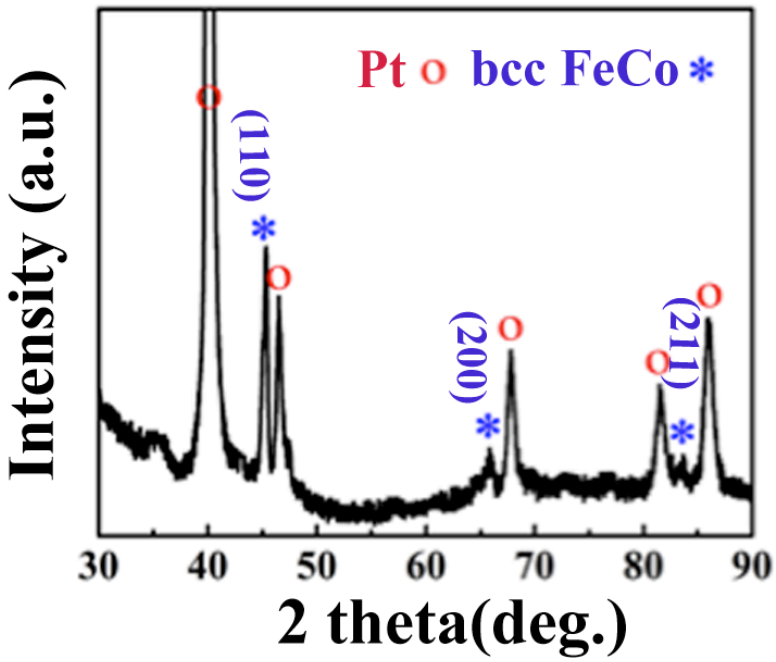

Figure 5 . 10. XRD spectra of the FeCo film.

The molar ratio of Co:Fe in the precursors was 1:2, which is consistent with the result detected from the EDS analysis. Figure 5. 10 shows the XRD patterns of bcc-FeCo film deposited on Pt substrate. From the patterns, it can be seen that the film have a bcc-FeCo phase with crystal planes of (110) (200)

(211) that are corresponding to the peak indexes at 44.8°, 65.0°, 82.6° (JCPDS card no.000441433). [45]

5.4.2 Morphology

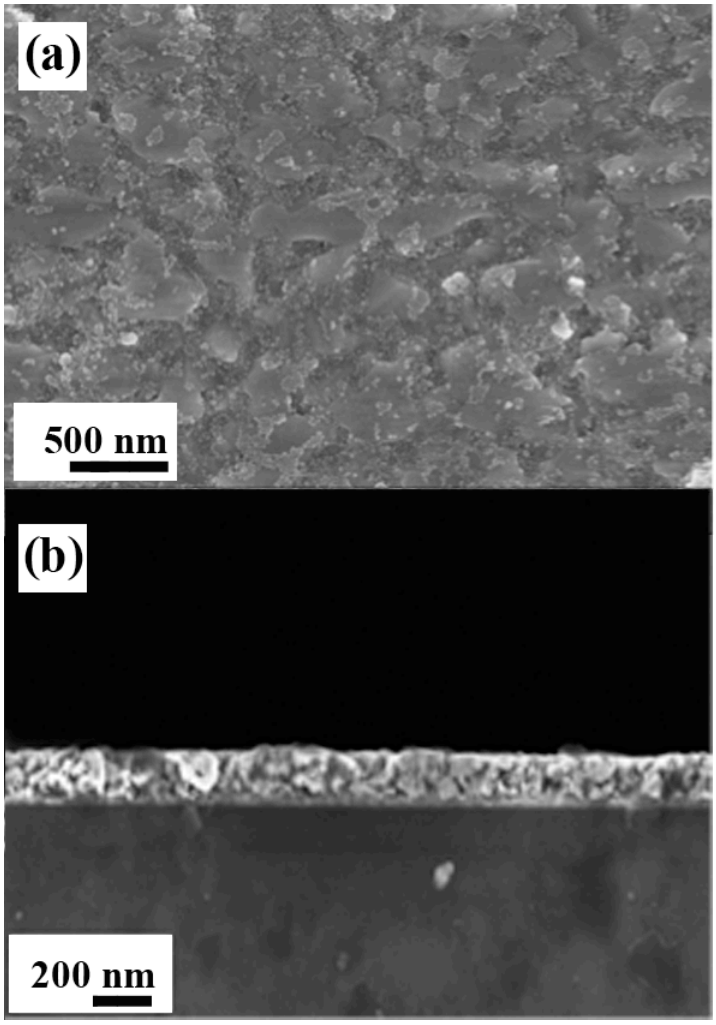

Figure 5. 11. (a) SEM images showing morphology of FeCo film, (b)Cross-section of SEM micrograph.

Figure 5. 11 shows the surface morphology of bcc-FeCo films deposited on Pt substrate by thermal decomposition. The surface of film shows a relatively poor quality when compared with Fe_3O_4 film deposited with similar method descried in the chapter 4. The films are uniform and around 250nm in thickness according to cross-section SEM images.

5.4.3 Magnetic property

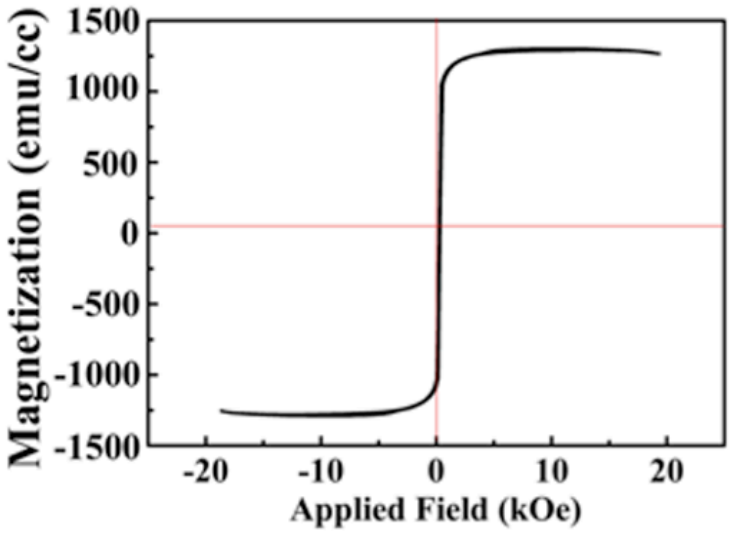

Figure 5. 12. In-plane hysteresis loop of bcc-FeCo film.

The magnetic property of as-deposited bcc-FeCo film is detected by the VSM (Figure 5.12). The saturation magnetization of bcc-FeCo film is around 1300 emu/cc. This value is lower than the bulk bcc-$Fe_{65}Co_{35}$ (around 1900 emu/cm^3), [46] it is probably caused by the oxidation of sample when rinse the film before VSM test.

5.5 Conclusions

We have developed an ecofriendly and safe method for the synthesis of hydrophobic and mono-dispersed FeCo nanoparticles. The saturation magnetization of the particles was dependent on composition and the highest magnetization was 187emu/g with Fe/Co ratio at 2:1. After the nanoparticles were transferred to aqueous phase by coating with PBMA, the cytotoxicity test indicated that the obtained nanoparticles have no cytotoxic effect upon the cell. The high bio-compatibility of FeCo@PBMA particles makes it a promising

material for future biomedicine applications. In addition, this method also had been approved available to synthesis 10nm Fe_3O_4 spherical nanoparticles and self-assembly hairy ball shape Co nanoparticles.

A wet chemical method had been presented to deposit FeCo film in thickness of 250nm. The bcc-FeCo phase was identified by XRD and its morphology was observed by SEM. The saturation magnetization of as-deposited film was 1300 emu/cc with Fe/Co ratio at 2:1.

REFERENCES:

[1] H. Zeng, J. Li, J.P. Liu, Z. L.Wang ,S.H. Sun, Nature **2002**, 420 , 395.

[2] T. D Schladt, K. Schneide, H. Schild, W. Tremel, Dalton T, **2011**, 40, 6315.

[3] K. E. Mooney, M. J. Wagner. J Mater Chem. **2009**, 19, 611.

[4] S.G. Kwon, Y. Piao, J. Park, S. Angappane, Y. Jo, N. M. Hwang, J. G. Park, T. Hyeon. J Am Chem Soc. **2007**, 129, 12571.

[5] L. Li, Y. Yang, J. Ding, J. M. Xue . Chem Mater. **2010**, 22, 3183.

[6] W. S. Seo, J. H. Lee, X. M. Sun, Y. Suzuki, D. Mann, Z. Liu, M. Terashima, P. C. Yang, M. V. McConnell , D. G. Nishimura, H. J. Dai. Nat Mater. **2006**, 5, 971.

[7] Y. Jing, H. Sohn, T. Kline, R. H. Victora, J. P. Wang. J Appl Phys. **2009**, 105, 305.

[8] N. Nishimura1, T. Hirai, A. Koganei, T. Ikeda, K. Okano, Y. Sekiguchi, Y. Osada,

J. Appl. Phys. **2002**, 91, 5246.

[9] D. Y. Kim, J. Hong, J. Magn. Magn. Mater. **2009**, 321, 1821.

[10] C, J, Jiang, C. Zhang, C. H. Dong, D. W. Guo, D. S. Xue, Appl. Phys. Lett. **2015**, 106, 122406.

[11] I. Jepu, , C. Porosnicu, C. P. Lungu, I. Mustata, C. Luculescu, V. Kuncser, G. Iacobescu, A. Marin, V. Ciupina, Surf Coat Tech, **2014**, 240, 344.

[12] C. Desvaux, C. Amiens, P. Fejes, P. Renaud,M. Respaud, P. Lecante, E. Snoeck, B. Chaudret. Nat Mater **2005**, 4, 750.

[13] X. W. Wei, G. X. Zhu, Y. J. Liu, Y. H. Ni, Y. Song, Z. Xu. Chem Mater **2008**, 20, 6248.

[14] D. Kodama, K. Shinoda, K. Sato, Y. Konno, R. J. Joseyphus, K. Motomiya, H. Takahashi, T. Matsumoto, Y. Sato, K. Tohji, Jeyadevan B. Adv Mater. **2006**, 18, 3154.

[15] C. Wang, S. Peng, L. M. Lacroix, S. H. SuN, Nano Res. **2009**, 2 ,380.

[16] G. S. Chaubey, C. Barcena, N. Poudyal, C. B. Rong, J. M. Gao , S. H. Sun, J. P. Liu, J Am Chem Soc. **2007**, 129, 7214.

[17] K. Zhang, O. Amponsah, M. Arslan, T. Holloway, D. Sinclair, W. Cao , M. Bahoura , A. K. Pradhan. J Magn Magn Mater. **2012**, 324, 1938.

[18] S. Alikhanzadeh-Arani, M. Salavati-Niasari, M. Almasi-Kashi, J Magn Magn Mater. **2012**, 324, 3652.

[19] M, Sorescu, A, Grabias, Intermetallics, **2002**, 10, 317.

[20] J. Grafe, M. Welke, F. Bern, M. Ziese, R. Denecke, J. Magn. Magn. Mater. **2013**, 339, 84.

[21] G. H. Jaffari, A. K. Rumaiz, C. Ni, E. Yassitepe, M. Bah, S. I. Shah, Curr. Appl Phys. **2015**, 15, 717.

[22] C. P. Yen, C. S. Wong, C. Y. Yeh, Y. M. Chen, H. H. Chu, J. Y. Lin, J. Wang P. H. Lin, S. Y. Chen, Appl. Phys. A, **2014**, 115, 671.

[23] K. Shikada, M. Ohtake, F. Kirino, M. Futamoto, J. Appl. Phys. **2009**, 105, 07C303.

[24] R. Zuberek, A. Wawro, H. Szymczak, A. Wisniewski, W. Paszkowicz, M.R.J. Gibbs. J. Magn. Magn. Mater. **2000**, 214, 155.

[25] N.Tsutomu, M. Ohtake, Kirino, . Kirino, M. Futamoto, J. Appl. Phys. **2010**, 107, 09A306.

[26] V. A.Vas'ko, Magnetics, IEEE Trans. **2004**, 40, 2335.

[27] D. Clemens, A. Vanantia, C. Terriera, P. Bönia, B. Schnyderb, S. Tixiera, M. Horisbergera, Physica B: Condensed Matter. **1997**, 234, 500.

[28] Y.P. Wu, G. C.H anb, L. B. Kong, J. Magn. Magn. Mater. **2010**, 322, 3223.

[29] K. Kakizaki, S. Yasoshim, K. K. Choi, K. Kamishim, N. Hiratsuk, J. Magn. Magn. Mater. **2007**, 310, 870.

[30] S. Groudeva-Zotova, H. Karl, A. Savan, J. Feydt, B. Wehner, T. Walther, N. Zotov, B. Stritzker, A. Ludwig, Thin Solid Films **2006**, 495, 169.

[31] Z. L. Wang, Z. R. Dai, S. H. Sun , Adv Mater. **2000**, 12, 1944.

[32] S. H. Sun, C. B. Murray, D. Weller, L. Folks, A. Moser, Science **2000**, 287, 1989.

[33] T. Hyeon, S. S. Lee, J. Park, Y. Chung, H. Bin, J Am Chem Soc. **2001**, 123, 12798.

[34] S. Si, A. Kotal, T. K. Mandal, S. Giri, H. Nakamura, T. Kohara. Chem Mater. **2004**, 16, 3489.

[35] T. Hyeon T, Chem Commun.**2003,** 8, 927.

[36] Y. L. Hou, Z. C. Xu, S. H. Sun. Angew Chem Int Edit **2007**, 46, 6329.

[37] Z. C. Xu, C. M. Shen, Y. L. Hou, H. J. Gao, S. S. Sun, Chem Mater. **2009**, 21, 1778.

[38] J. Park, K. J. An, Y. S. Hwang, J. G. Park, H. J. Noh, J. Y. Kim, J. H . Park, N. M. Hwang, T. Hyeon , Nat Mater. **2004**, 3, 891.

[39] D. Kim, J. Park, K. An, N. K. Yang, J. G. Park, T. Hyeon. J Am Chem Soc **2007**, 129, 5812.

[40] E. S. G. Choo, X. S. Tang, Y. Sheng, B. Shuter, J. M. Xue, J Mater Chem. **2001**, 21, 2310.

[41] S. Shen, J. F. Rena, J. Chen, X. H. Lu, C. H. Deng, X. G. Jiang, J. Chromatogr. A. **2011**, 1218, 4619.

[42] M. Castrill, A. Mayoral, A. Urtizberea, C. Marquina, S. Irusta, J. G. Meier, J. Santama, Nanotechnology, **2013**, 24, 505702.

[43] R. L. Johnston, J. P. Wilcoxon, Metal Nanoparticles and Nanoalloys, Elsevier, USA **2012**.

[44] T. Wang, D. LaMontagne, J. Lynch, J. Zhuang, Y. C. Cao. Chemical Society Reviews **2013**, 42, 2804.

[45] N. A. M. Barakat, M. F. Abadir, K. T. Nam, A. M. Hamza, S. S. Al-Deyab, W. Baek, H. Y. Kim, J. Mater. Chem. **2011**, 21, 10957.

[46] N. Ji, X. Q. Liu, J. P. Wang, New, J, Phys. **2010**, 12, 063032.

Chapter 6 Chemical synthesis of magnetic FePt nanoparticle and $L1_0$- FePt film

In Chapter 5, we have investigated the typical Fe-3d transition metal alloy; FeCo nanoparticles and films. In this chapter, Fe-5d transition metal alloy will be studied. In Fe–5d alloys, the large magnetic moments of the Fe 3d electrons are combined with the rather large spin–orbit interaction ξ of the 5d electrons. The Fe–5d alloys will be studied in this chapter is FePt. In FePt alloy, the spin-orbit interaction of 5d element Pt (ξPt = 0.6 eV) is about one order of magnitude higher than that of Fe(ξFe = 0.08 eV), resulting in an increase of the orbital moment of the 3d electrons and a larger magnetic anisotropy. [1].

6.1 Introduction

Currently, magnetic materials with high coercivity have been intensively studied by many researchers because of their promising application in recording medium, micro electromechanical systems (MEMS), permanent magnet or bias layer for spin electronic devices [2-10]. Among various hard magnetic materials, FePt with ordered $L1_0$ phase had drawn a significant attention because of their high magnetocrystalline anisotropy, high Curie temperature, large saturation magnetization and good corrosive resistance [11-16]. In addition, fcc disordered phase of FePt has also attracted some attention in connection with its possible use as a room temperature superparamagnet for biomedical applications. [17-21]

Some synthesis protocols had been reported for preparation of FePt nanoparticle and film. Till now, most technique for FePt nanoparticle growth is based on thermal decomposition. Usually, disordered fcc-FePt nanoparticle is formed through decomposition of $Fe(CO)_5$ and reduction of $Pt(acac)_2$, [22-24] or co-reduction of iron salt and $Pt(acac)_2$ [25,26] while $L1_0$-FePt nanoparticle is synthesized by post-annealing process of fcc-FePt nanoparticle. [27-29]. With respect to the deposition techniques for FePt films, most of them are vacuum deposition methods, such as pulse laser deposition [30-32], molecular bean epitaxy [33] and sputtering [34-37]. However, all these procedures are involved with high vacuum systems and the high cost of the equipment severely limits their application [38,39]. As an alternative approach, the wet chemical route we presented offers several advantages, particularly, low cost of equipment.

In chapter 5, we presented a we chemical route to fabricate FeCo nanoparticle. In the former part of this chapter, this method had been successfully applied for synthesis of fcc-FePt nanoparticle. The magnetic properties of fcc-FePt nanoparticle was investigated by VSM. In the later part, we have developed a method to fabricate FePt films by a combination of chemical deposition and post-annealing. Pt-doped Fe films were deposited on Pt(100nm)/Ti(50nm)/SiO_2/Si substrate using thermal deposition and the as-deposited films were subsequently annealed from 300°C to 800°C under 5%H_2/95%N_2. $L1_0$-phase FePt films were achieved through diffusion and rearrangement of Fe and Pt atoms in post-annealing process. We investigated the structure of as-deposited and annealed FePt films with annealing

temperatures, and studied the effects of post-annealing treatment on magnetic properties of the films.

6.2 Experimental

6.2.1 Materials and characterization

FeO(OH) (catalyst grade 30-50 mesh), oleic acid (OA), TOA (Trioctylamine 98%), 1-2 hexadecanediol (technical grade 98%) were purchased from Sigma-Aldrich and H_2PtCl_6 (~%38Pt) was brought from Tianjin Yingda Sparseness & Noble Reagent Chemical Factory. All the reagents were of analytical grade and were used without further purification.

The crystal phase of the FePt film was determined by the θ–2θ geometry X-ray diffractometer system (XRD; Bruker D8 Advanced Diffractometer System, Karlsruhe, Germany) with a Cu Ka (1.5418 Å) source. Transmission electron microscope (TEM) images were obtained with a JEOL 2010 microscope at an acceleration voltage of 200 kV. Magnetic properties were detected by superconducting quantum interference device (SQUID; Quantum Design, MPMS, XL-5). The morphology of samples was examined by scanning electron microscopy (SEM; Zeiss Supra 40). Energy-dispersive X-ray spectroscopy (EDS) attached with the SEM and TEM was used for elemental analysis with the accelerating voltage at 15 kV. The samples for observation under TEM were treated with a mechanical polishing followed by an ion milling to perform final stage thinning. The Bravman-–Sinclair method was used to prepare cross-sectional samples.

6.2.2 Synthesis of FePt nanoparticles

Firstly, mixtures of FeO(OH) and H_2PtCl_6 in desired proportions with suitable amount of solvent TOA (Trioctylamine) were loaded into a three neck flask, and then the mixture was dehydrated at 180°C for 1h under a flow of argon. After that, the solution was quickly heated to 365°C while stirring using a stirring bar and aged for 2 hours. During the process, we observed that the solution containing Fe and Pt ions turn rapidly into muddy black when reaching the refluxing temperature. Lastly, the resulting black solution was cooled to room temperature and washed several times with ethanol and hexane followed by centrifugation at 10000 prm. Half of product obtained was dispersed into hexane while the rest was dried overnight for further characterization.

6.2.3 Fabrication of FePt film

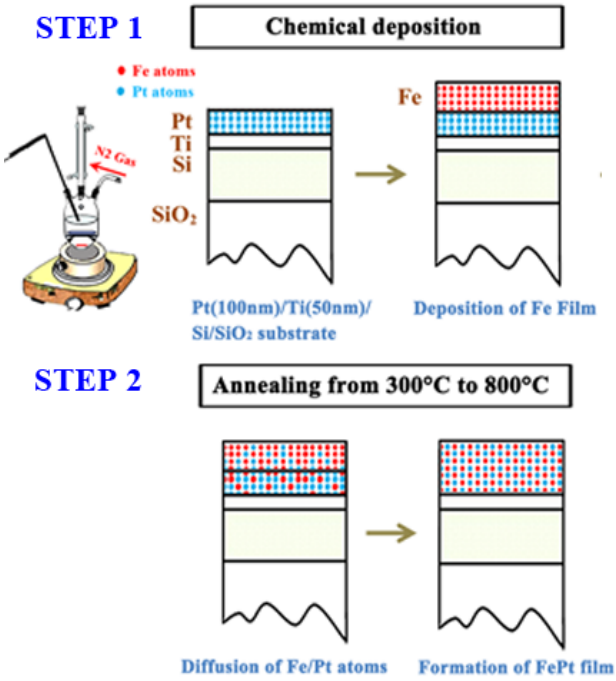

Figure 6. 1. Reaction scheme for the synthesis of FePt films.

The fabrication procedure is shown in Figure 6.1. The deposition of Fe Film on Pt(100nm)/Ti(50nm)/SiO_2/Si substrate is based on thermal decomposition. Its procedure is similar to that of our previous report [40] which describes a wet chemical route to synthesize Fe_3O_4 nanoparticles. We found that the same procedure is applicable for film deposition if a substrate is placed in the three-neck flask. The product is the Fe film that is grown on Pt(100nm)/Ti(50nm)/SiO_2/Si substrate. Firstly, substrate was placed in a three-neck flask, then the desired proportions of FeO(OH), H_2PtCl_6 and 1-2 hexadecanediol with suitable amount of TOA solvent and OA were loaded inside. After glass separator and magnetic bar were set, the mixture was dehydrated at 180 °C for 1 hour under a flow of argon and then quickly heated to 300 °C for 3 hours. At the refluxing temperature, it was found that the solution turned from red into muddy black. After the black solvent was cooled to room temperature, the substrate was removed from the flask and washed 3 times with hexane in asonicator. Lastly, the as-deposited FePt film was annealed at an annealing temperature between 300 and 800 °C.

The same synthesis procedure was applied for the reaction without H_2PtCl_6, after dehydration, the solution was heated to 300 °C for 3 hours and the as-synthesized film was washed for characterization.

6.3 FePt nanoparticle

6.3.1 Structure characterization

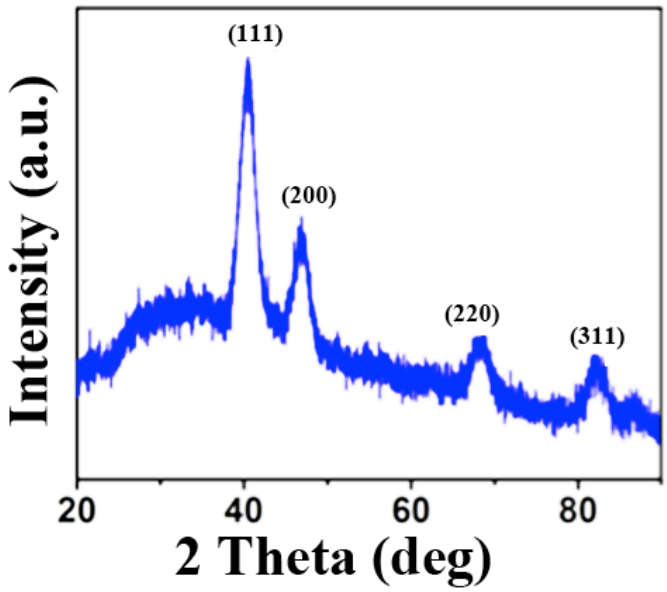

Figure 6. 2. XRD spectra of the fcc-FePt nanoparticle.

Figure 6. 2 shows X-ray diffraction pattern of the resulting product. The sharp peaks matched well with those standard data for fcc-FePt (JCPDS, 29-0718). [41]. From the XRD pattern, we can observe crystal planes of (111), (200), (220) and (311) that are corresponding to the peak indexes at 40.04°C, 47.02°C, 68.71°C and 82.79°C. The elemental composition of as-synthesized nanoparticles was confirmed with EDS analysis and their final particle composition is $Fe_{76}Pt_{24}$.

6.3.2 Morphology

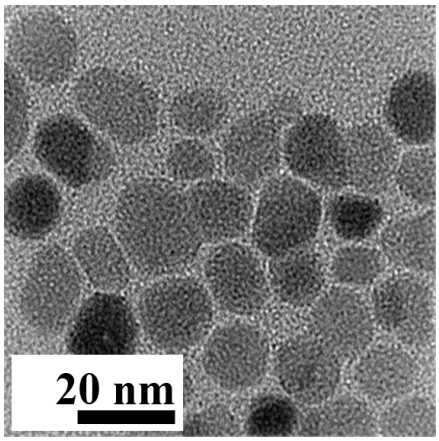

Figure 6. 3. SEM images showing morphology of fcc-FePt nanoparticle.

Figure 6. 3 shows a typical TEM image of the as-synthesized fcc-FePt nanoparticles. Different from the methods used in other reports that fabricate FePt nanoparticle less than 5 nm [23, 42-45], the approach we presented is capable to produce fcc-FePt nanoparticle in larger size at around 15 nm. However, from the TEM image (Figure 6. 3), compared with FeCo and Fe_3O_4 nanoparticles synthesized in the Chapter 4 and 5, as-synthesized FePt nanoparticle is not so uniform. In addition, dispersibility of sample powder in organic solution is not good.

6.3.3 Magnetic property

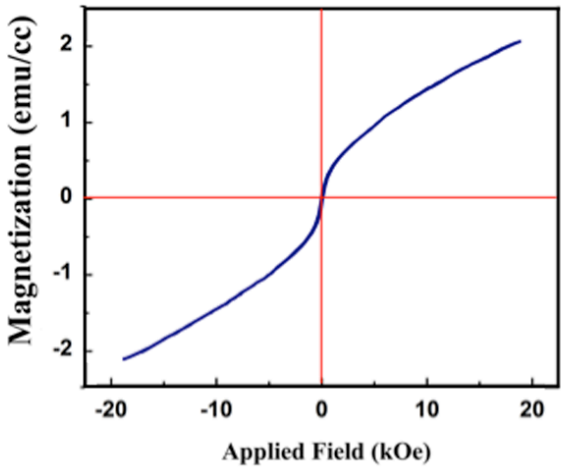

Figure 6. 4. In-plane hysteresis loop of fcc-FePt nanoparticle.

The in-plane hysteresis loop for the samples synthesized is shown in Figure 6. 4. The coercively is around 150 Oe at room temperature. The magnetic curve and the presence of nonzero value for the coercivity indicates paramagnetic behavior, suggesting not all the FePt particles are completely superparamagnetic and some amount of ordering should be present

6.4 FePt film

6.4.1 Fe film and Pt-doped Fe film synthesis

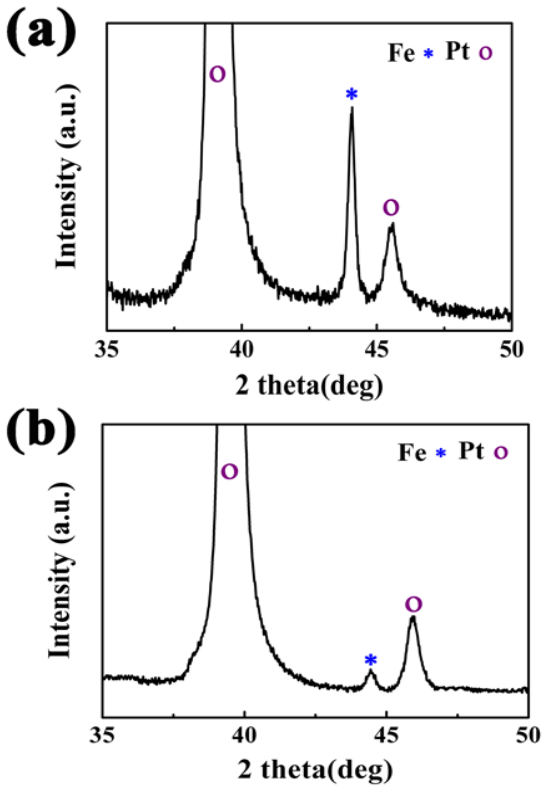

Figure 6. 5. (a) XRD pattern of Fe film, (b) XRD pattern of Fe film after 168 hours.

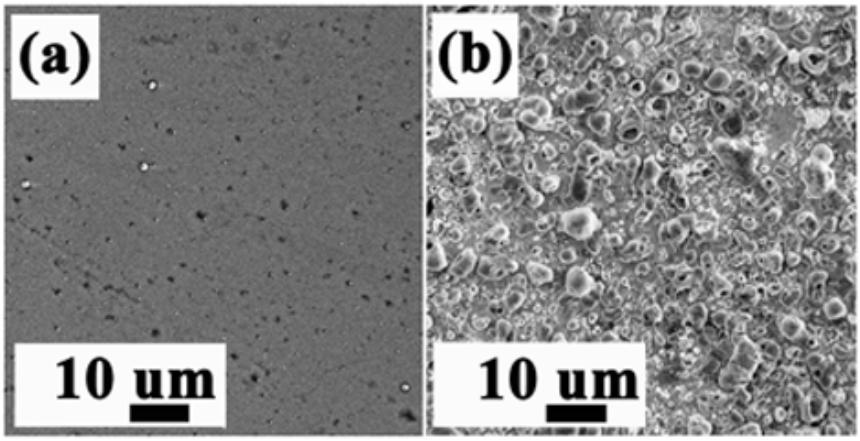

Figure 6. 6. (a) and (b) morphology images of as-synthesized film from SEM observed directly and 168 hours later.

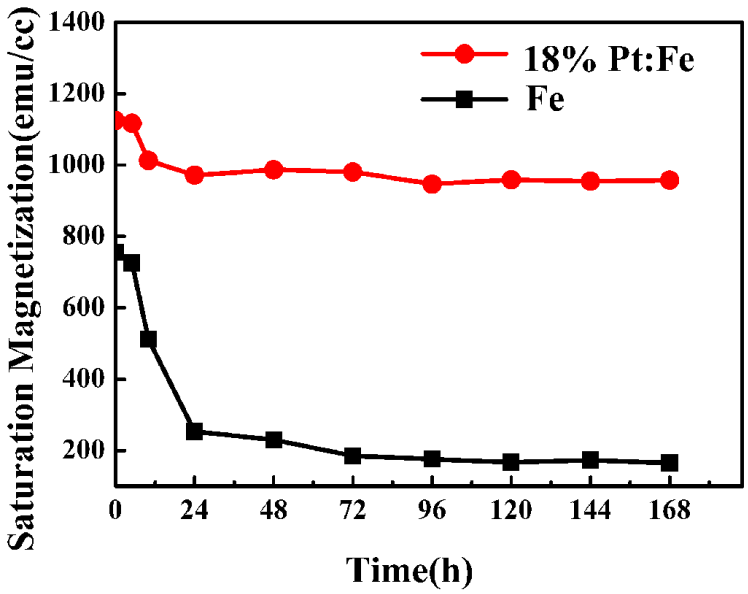

Figure 6. 7. The saturation magnetization trend as function of exposed time of Fe film and Pt-doped Fe film.

The Fe film of 150 nm was synthesized with the single precursor FeO(OH). XRD was used in the study of films. The formation of bcc-Fe was confirmed by the (110) peak at 44.6° in the XRD pattern (Figure 6. 5(a)). Figure 6. 6(a) showed the SEM morphology of Fe film, the surface of deposited films was smooth and continuous. As shown in Figure 6. 7, the as freshly deposited Fe film possessed a saturation magnetization of approximately 800 emu/cc, which is expected by metallic bcc-Fe (with a theoretical saturation magnetization of 1700 emu/cc) [46]. However, saturation magnetization decreased rapidly with time when the film was exposed to air, approximately 200 emu/cc after 24 hours. After exposure of the Fe film in air for 168 hours, saturation magnetization was further reduced to 130 emu/cc, which is higher than the bulk value of α-Fe_2O_3 (1 emu/cc) [47] and lower than that of Fe_3O_4 (477 emu/cc) [48] and γ-Fe_2O_3(408 emu/cc) [47], suggesting that part of bcc-Fe phase may transform to α-Fe_2O_3 phase. In addition, much lower bcc-Fe (110)

peak was found in XRD spectrum (Figure 6. 5(b)) for films exposed in air for 168 hours and our EDS study suggested oxidation of metallic. Nevertheless, from the Figure 6. 6(b) that the sample was observed after exposure to air for 168 hours and the surface of films was cracked and curled up to a tube-like shape. This work shows that metallic Fe film prepared by this method was not stable when exposed in air and can be easily oxidized.

In order to enhance chemical stability, Pt was doped by adding H_2PtCl_6 together with FeO(OH) for the deposition of Fe films. As shown above, Fe films of a thickness of 150 nm could be formed conveniently. In order to form FePt films by Pt diffusion (or Fe diffusion), the ratio of Fe and Pt should be kept around 1:1. As there was a Pt underlayer of 100 nm, the ratio of Fe:Pt should be around 5:1 in the Pt-doped Fe film with a thickness of 150 nm. After an adjustment of the amount of H_2PtCl_6, we deposited Pt-doped Fe films with a Pt composition of 18 at.%. The Pt-doped Fe films showed greatly improved chemical stability in air. As shown in Figure 6. 7, saturation magnetization was remained around 1000 emu/cc after exposure in air over 160 hours. From the analysis of XRD, no obvious change has been found after the Pt doping (18 at.%) and XRD pattern remained nearly unchanged after exposure in air over 160 hours.

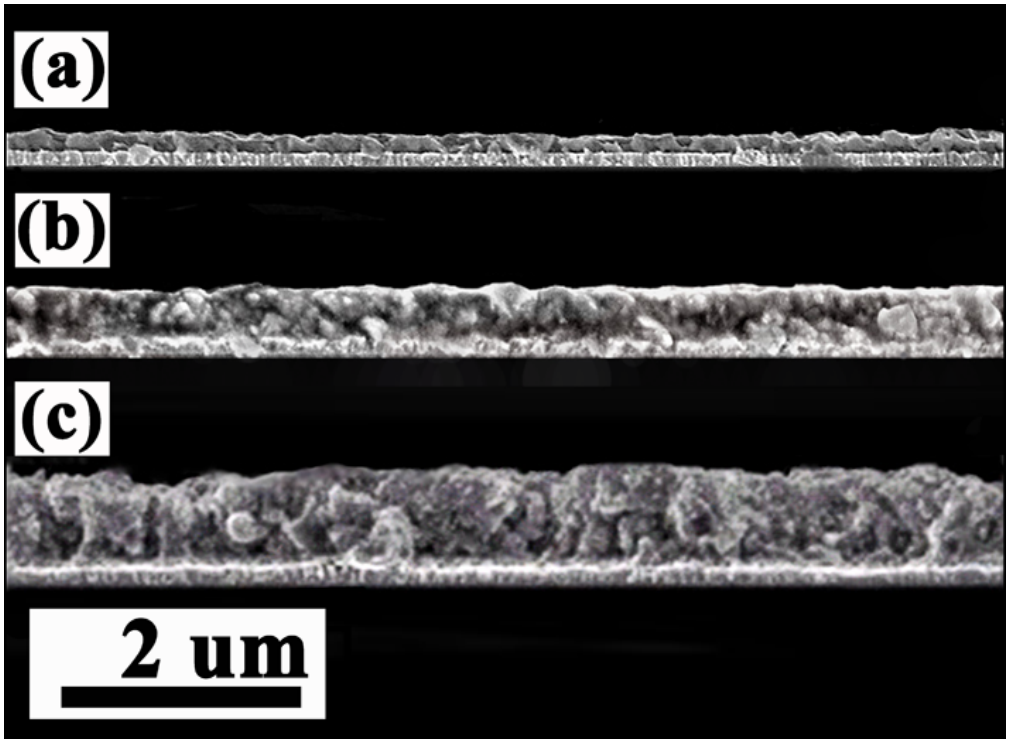

Figure 6. 8. SEM cross-section image of as-synthesized Fe films with different thickness (a) 150nm, (b) 400nm and (c) 700nm.

Despite the Pt-doped Fe films in the thickness of 150 nm as shown in SEM cross-section image of Figure 6. 8(a), the thickness could be tuned to 400 nm (Figure 6. 8(b)) and 700 nm (Figure 6. 8(c)). The boundary of the as-synthesized Pt-doped Fe film and underlayers could be clearly seen. The increase of the film thickness was the result of the more surfactant (Oleic acid) used.

6.4.2 FePt synthesis by annealing and structure characterization

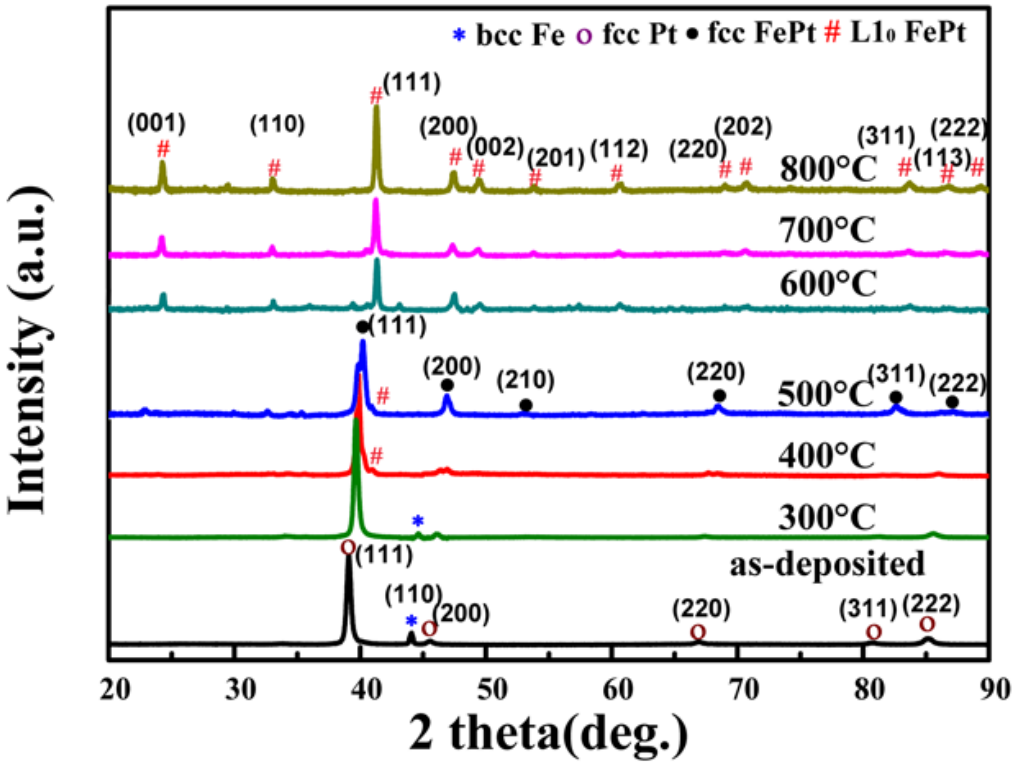

Figure 6. 9. X-ray diffraction of films after annealing at different temperature.

The Pt-doped Fe Film was annealed in the atmosphere of 5%H_2/ 95%N_2 at different temperatures. XRD was used in the study of the formation of the desired hard magnetic $L1_0$-FePt phase. It could be seen in Figure 6. 9 that the as-deposited Pt-doped Fe film showed a mixture of bcc-Fe and $L1_0$-Pt (of the Pt underlayer). The fundamental (111) peak (40.31°) of disordered fcc-FePt phase appeared after annealing at 300 °C, whereas the intensity of the bcc-Fe peak was much lower than that of the as-deposited film. This result shows that the formation of disordered fcc-FePt phase started to form at 300 °C due to diffusion of Fe and/or Pt. The annealing at 400 °C and 500 °C led to the domination of the disordered $L1_0$-FePt phase, as both XRD peaks of bcc-Fe and fcc-Pt disappeared. A small peak corresponding to the (111) plane of the

ordered $L1_0$-FePt phase was exhibited at 41.09 °C after annealing at 400°C or higher. After annealing at 600 °C, the (001) super lattice peak of the $L1_0$ phase appeared with the intensity ration (I_{001}/I_{111}) of about 0.36 which is slightly higher than the ratio of 0.33 estimated from the XRD database @ Socabin (03-065-9121), suggesting a small (001) texture. There was nearly no fcc phase after anealing at 600 °C or higher, indicating the complete transformation from fcc to $L1_0$ phase. Further increase in annealing temperature to 800 °C resulted in higher intensities of peaks for $L1_0$ phase, especially the (001) peak. The relative intensity of the super-lattice (001) peak for $L1_0$-FePt phase is higher compared with the standard PDF file of isotropic FePt (JCPDS file 431359). The degree of (001) texturing (I_{001}/I_{111}) increased with the annealing temperature, indicating that the film has a small crystallographic (001) texture. At 800 °C, the calculated d-spacings of the FePt (001) and (111) planes according to Bragg law are d=0.368 nm and 0.219 nm respectively, which are similar to the other results for $L1_0$-FePt reported in the literature [49-52].

6.4.3 Effect of annealing temperature on ordering parameter

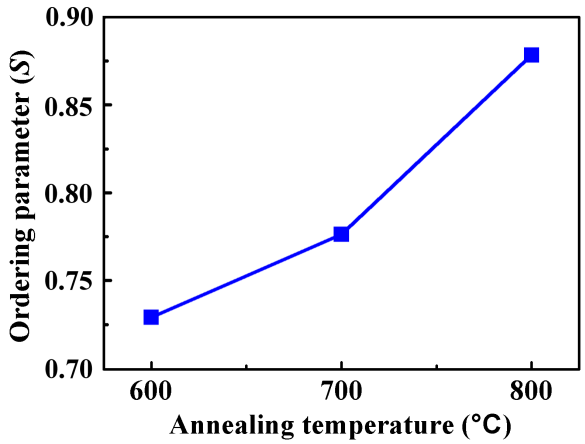

Figure 6. 10. Dependence of ordering parameter (*S* order) of FePt film on annealing temperature.

To investigate the growth degree of $L1_0$ phase after annealing, the ordering parameter *S* was evaluated as follows. From the integrated intensity of FePt (0 0 1) and FePt (0 0 2), the ordering parameter *S* is defined as [53]:

$$S = [(\frac{I_{(001)}}{I_{(002)}}) \times \left(\frac{F_f}{F_s}\right)^2 \frac{(L \times A \times D)_f}{(L \times A \times D)_s}]^{1/2} = k \times (\frac{I_{(001)}}{I_{(002)}})^{1/2} \quad (1)$$

Where $I_{(001)}$ and $I_{(002)}$ represent the integrated intensities of the (001) and (002) peaks, F, L, A and D are the structure factor, Lorentz polarization factor, absorption factor and temperature factor, respectively. f refers to fundamental peak and s refers to superlattice peak. The k value (0.59) was estimated by following the analysis described in [53]. Fig. 7 plots the results as a function of annealing temperature. The chemical ordering *S* was found to increase with increasing temperature from 600 °C to 800 °C, from 0.73 to 0.88.

6.4.4 Magnetic properties

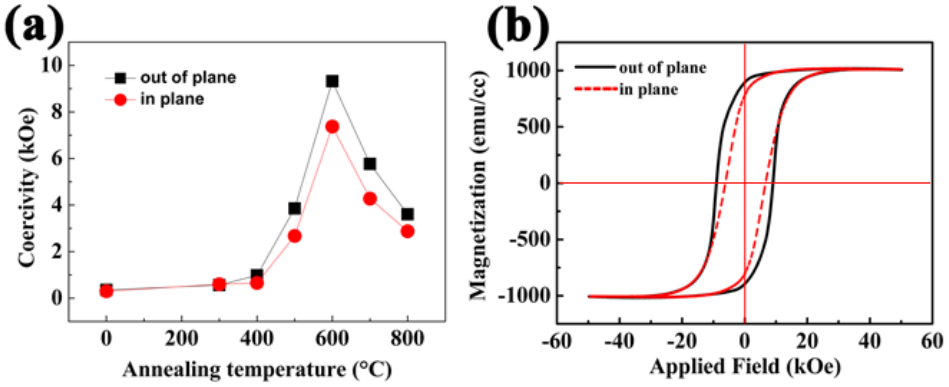

Figure 6. 11. (a) In-plane and out-of-plane coercivities depend on various temperatures, (b) The in-plane and out-of-plane hysteresis loops of FePt film at 600°C.

The in-plane and the out-of-plane coercivities in dependence of annealing temperature are plotted in Figure 6. 11(a). The SQUID result agrees well with our XRD results. With the formation of $L1_0$-FePt phase, coercivity started to increase (after annealing at 400 °C). Maximum coercivity (9 kOe) was obtained after annealing at 600 °C, whereas the phase transformation from soft-magnetic fcc to hard-magnetic $L1_0$ was completed and the film possessed a nanograined structure. At higher temperatures, coercivity decreased with increasing annealing temperature, as a result of grain growth.

Another observation is that out-of–plane coercivity is always slightly higher than that of in-plane coercivity. The small out-of-plane magnetic anisotropy may originate from the magnetocrystalline anisotropy because of a small out-of-plane (001) texture. A set of in-plane and out-of-plane hysteresis loops of the film annealed at 600 °C is shown in Figure 6.11(b). The hysteresis loops demonstrate magnetic out-of-plane anisotropy. With increasing the annealing temperature from 300°C to 500°C, the saturation magnetization (Ms) of FePt film increases from 720 emu/cc to 850 emu/cc, which is lower than bulk value of fcc-FePt (1030 emu/cc) [54]. At 600°C, the Ms of FePt is 1000 emu/cc and it slightly increases to 1080 emu/cc at 800 °C, which is close to the bulk value of $L1_0$-FePt (1140 emu/cc) [55].

6.4.5 Morphology

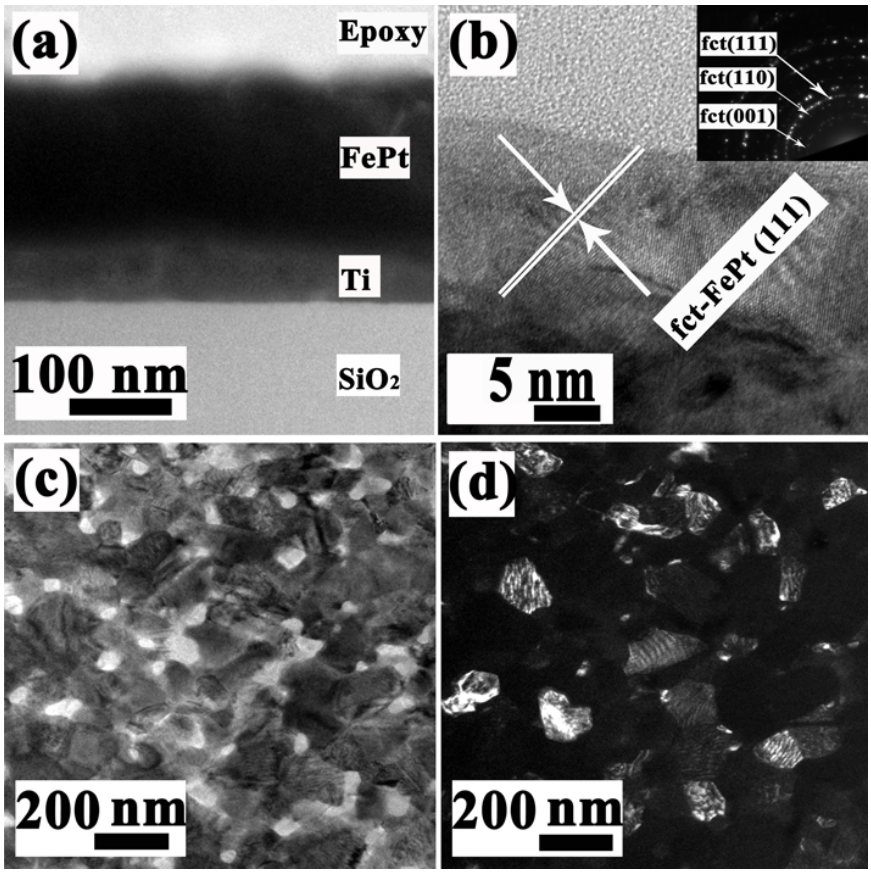

Figure 6. 12. (a) Cross-section of TEM micrograph of FePt film after annealing at 800 °C, (b) HRTEM image of the prepared FePt and inset is an electron diffraction pattern of the selected area, the rings labeled with Miller indices correspond to the expected $L1_0$-FePt pattern, (c) and (d) showed the plane view bright and dark-field TEM images of the $L1_0$-FePt film annealed at 800 °C.

The TEM cross-section micrograph of FePt after annealing at 800 °C was illustrated in Figure 6. 12(a). Based on the densities of bcc-Fe, fcc-Pt and the alloy $L1_0$-FePt, the volume of fcc-FePt should be reduced by 20-25% if the bi-layers of bcc-Fe and fcc-Pt form the single phase $L1_0$-FePt. Our TEM results showed a thickness of 160 nm for $L1_0$-FePt, which agree well with the expected thickness. By EDS examination (which is equipped with our TEM system), the composition of the FePt film was found to approximately 50

at.%Fe & 50 at.%Pt, showing a good agreement with our calculation expectation. Besides, it has been observed that the composition of Fe and Pt was uniform throughout the thickness of the film. From d spacing analysis of the HRTEM in Figure 6. 12(b), the lattice fringe was consistent with the $L1_0$-FePt (111) plane. The diffraction rings from $L1_0$-(001) (110) and (111) can be observed in electron diffraction pattern, consistent with XRD patterns as shown in Figure 6. 9. There is no clear ring from fcc phase observed, suggesting the high $L1_0$ ordering after post-annealing. Different from the cross-section view of Fe film in Figure 6. 6, no Pt underlayer could be observed, as we could only find the $L1_0$-FePt layer above Ti underlayer, indicating that the bcc-Fe and fcc-Pt layers form $L1_0$-FePt intermetallic after annealing at 800 °C through diffusion under H_2. Figure 6. 12(c) and (d) showed the bright and dark-field images of $L1_0$-FePt film annealed at 800 °C. The bright area in Figure 6. 12(d) is the area with $L1_0$ ordered structure satisfying the diffraction condition. The average grain size measured from TEM image is 110nm, which is nearly 50 nm higher than the value evaluated by Scherrer's formula from XRD pattern of FePt film after being annealed at 600 °C.

6.5 Conclusions

A thermal decomposition method was applied for synthesis of FePt nanoparticles. The fcc-FePt phase was identified by XRD and the morphology was observed by TEM. The nanoparticle size measured from TEM image is around 15nm. From VSM study, the coercivity of fcc-FePt sample is around 150 Oe at room temperature rather than 0 Oe as expected for typical superparamagnetic disordered FePt phase, indicating the presence of some amount of ordering ($L1_0$) phase. In addition, We have developed a method for

the synthesis of FePt film by annealing of Pt-doped Fe film on Pt(100nm)/Ti(50nm)/SiO_2/Si substrate. A wet chemical route was used in the synthesis of Pt-doped Fe films on Pt underlayer. We have found out that doping with a relatively small amount of Pt can enhance chemical stability significantly. A post-annealing can lead inter-diffusion between Fe and Pt layers to form FePt intermetallic phase. Diffusion occurs after post-annealing to form disordered fcc-FePt at 300 °C, which can further transform into hard-magnetic $L1_0$-FePt phase. The FePt films showed out-of-plane anisotropy with the maximum coercivity of 9 kOe after annealing at 600°C. Reduced coercivity obtained after annealing at higher temperatures (700°C and 800°C) was probably due to grain growth. TEM and TEM-EDS results confirmed the $L1_0$-FePt phase and uniform composition approximately Fe:Pt = 50:50 throughout the thickness of film.

REFERENCES:

[1] J. Honolka, T.Y. Lee, K. Kuhnke, A. Enders, R. Skomski, S. Bornemann, S. Mankovsky, J. Minar, J. Staunton, H. Ebe, M. Hessler, K. Fauth, G. Schütz, A. Buchsbaum, M. Schmid, P. Varga, K. Kern, Phys. Rev. Lett. 2009, 102, 067207.

[2] K. Leistner, J. Thomas, H. Schlorb, M. Weisheit, L. Schultz,S. Fahler, Appl. Phys. Lett. 2004, 85, 3498.

[3] S. Sun, Adv. Mater. 2006, 18, 393.

[4] G. Sáfrán, T. Suzuki, K. Ouchi, P.B. Barna, G. Radnóczi, Thin Solid Films 2006, 496, 580.

[5] S. Simizu, R.T. Obermyer, B. Zande, V.K. Chandhok, A. Margolin,S.G. Sankar, J. Appl. Phys. 2003, 93, 8134.

[6] X. Rui, J.E. Shield, Z. Sun, L. Yue, Y. Xu, D.J. Sellmyer, Z. Liu and D.J. Miller, J. Magn. Magn. Mater. 2006, 305, 76.

[7] Y.N. Hsu, S. Jeong, D.N. Lambeth, D.E. Laughlin, Trans. Magn. 2000, 36, 2945.

[8] X.J. Liu, M.Y. Gao, A.D. Li, Y.Q. Cao, X.F. Li, B.L. Guo, Z.Y. Cao, D. Wu, J. Alloys Comp. 2014, 588, 103.

[9] T. Seki, Y. Hasegawa, S. Mitani, S. Takahashi, H. Imamura, S. Maekawa, J. Nitta,K. Takanashi, Nat. Mater. 2008, 7, 125.

[10] G.J. Li, C.W. Leung, Z.Q. Lei, K.W. Lin, P.T. Lai, P.W.T. Pong, Thin Solid Films 2011, 519, 8307.

[11] Y.S. Yu, H.B. Li, W.L. Li, M. Liu, Y.M. Zhang, W.D. Fei,D.J. Sellmyer, Thin Solid Films 2010, 518, 2171.

[12] R.F. Marks, M.F. Toney, A. Cebollada, G.R. Harp, , J. Appl. Phys. 1996, 79, 5967.

[13] S. Thongmee, B.H. Liu, J. Ding, J.B. Yi, Thin Solid Films 2010, 518, 7053.

[14] O. A. lvanov, L. V. Solina, V. A. Demshina, L. M. Magat, Phys. Met. Metallogr. 1973, 35, 81.

[15] C.W. Hsu, S.K. Chen, W.M. Liao, F.T. Yuan, W.C. Chang, J.L. Tsai, J. Alloys Comp. 2008, 449, 52.

[16] C.B. Rong, Y. Li, J.P. Liu, J. Appl. Phys. 2007, 101, 09K505.

[17] R. Hergt, W. Andra, C. G. d'Ambly, I. Hilger, W. A. Kaise, U. Richter, H. G. Schmidt, IEEE Trans. Magn. 1998, 34, 3745.

[18] S. H. Chung, A. Hoffmann, S. D. BadeR, C. Liu, B. Kay, L. Makowski, L. Chen, Appl. Phys. Lett. 2004, 85, 2971.

[19] T. Neuberger, B. Schopf, H. Hofmann, M. Hofman, B. V. Rechenberg, J. Magn. Magn. Mater. 2005, 293, 483.

[20] P. Nikitin, P. M. Vetoshko , T. I. Ksenevich , J. Magn. Magn. Mater. 2007, 311, 445.

[21] R.Hergt, S. Dutz, J. Magn. Magn. Mater. 2007, 311, 187.

[22] B. Stahl, N. S. Gajbhiye, G. Wilde, D. Kramer, J. Ellrich, M. Ghafari, H. Hahn, H. Gleiter, J. Weissmu¨ller, R. Wu¨rschum, P. Schlossmacher, AdV. Mater. 2002, 14, 24.

[23] S. Sun, E. E. Fullerton, D. Weller, C. B. Murray, IEEE Trans. Magn. 2001, 37, 1239.

[24] M. Chen, D. E. Nikles, Nano Lett. 2002, 2, 211.

[25] T. Iwaki, Y. Kakihara, T. Toda, M. Abdullah, K. Okuyama, J. Appl. Phys. 2003, 94, 6807.

[26] B. Jeyadevan, K. Urakawa, A. Hobo, N. Chinnasamy, K. Shinoda, K. Tohji, D. D. Djayaprawira, M. Tsunoda, M. Takahashi, Jpn. J. Appl. Phys. 2003, 42, L350.

[27] M. S. Seehra, V. Singh, P. Dutta, S. Neeleshwar, Y. Y. Chen, C. L. Chen, S. W. Chou, C. C. Chen, J. Phys. D: Appl. Phys. 2010, 43, 145002.

[28] Y. Tamada, Y. Morimoto, S. Yamamoto, M. Takano, S. Nasu, T. Ono, J. Magn. Magn. Mater. 2007, 310, 2381.

[29] C. B. Rong, N. Poudyal, G. S. Chaubey, V. Nandwana, Y. Liu, Y. Q. Wu, M. J. Kramer, M. E. Kozlov, R. H. Baughman, J. P. Liu, J. Appl. Phys. 2008, 103, 07E131.

[30] Y. Wang, R. Medwal, N. Sehdev, B. Yadian, T.L. Tan, P. Lee, A. Talebitaher, U. Ilyas, R.V. Ramanujan, Y. Huang,R.S. Rawat, Appl. Surf. Sci. 2014, 288, 381.

[31] L.J. Qiu, J. Ding, A.O. Adeyeye, J.H. Yin, J.S. Chen, S. Goolaup, N. Singh, IEEE Trans. Magn. 2007, 43, 2157.

[32] K.f. Dong, X.f. Yang, J.b. Yan, W.m. Cheng, X.m. Cheng, X.s. Miao, X.h. Xu,F. Wang, J. Alloys Comp. 2009, 476, 662.

[33] T. Konagai, Y. Kitahara, T. Itoh, T. Kato, S. Iwata, S. Tsunashima, J. Magn. Magn. Mater. 2007, 310, 2662.

[34] J. Wang, B. Yang, W. Pei, G. Qin, Y. Zhang, C. Esling, X. Zhao,L. Zuo, J. Magn. Magn. Mater. 2013, 345, 165.

[35] O.P. Pavlova, T.I. Verbitska, I.A. Vladymyrskyi, S.I. Sidorenko, G.L. Katona, D.L. Beke, G. Beddies, M. Albrecht, I.M. Makogon, Appl. Surf. Sci. 2013, 266, 100.

[36] X.J. Mo, H. Xiang, W. Lu, Y.P. Zheng, G.Q. Li, H. Saito, S. Ishio, D.M. Jiang, X.W. Tan, Y.Q. Lin, JPCS. 2011, 266, 012040.

[37] B. Yao, K.R. Coffey, J. Appl. Phys. 2008, 103, 07E107.

[38] Q. X. Jia, T. M. McCleskey, A. K. Burrell, Y. Lin, G. Collis, H. Wang, A. D. Q. Li, S. R. Foltyn, Nature Materials. 2004, 3, 529.

[39] L. Fei, M. Naeemi, G. F.Zou, H.M.Luo, The Chemical Record. 2013, 13, 85.

[40] X. L. Hong, M. Li, N. Bao, E. Peng, W. Li, J. Xue, J. Ding, J Nanopart Res. 2014, 16, 01.

[41] K. Fukuda, S. Fujieda, K. Shinoda, S. Suzuki, B. Jeyadevan, J. Phys.: Conf. Ser. 2012, 352, 012020.

[42] C. Min, J. P. Liu, S. H. Sun, J. Am. Chem. Soc., 2004, 126, 8394.

[43] M. Aslam, L. Fu, S. Li, V. P. Dravid, J Colloid Interface Sci. 2005, 290, 444.

[44] D. Li, N. Poudyal, V. Nandwana, Z. Jin, K. Elkins, J. P. Liu, J. Appl. Phys. 2006, 99, 08E911.

[45] K. E. Elkins, T. S. Vedantam, J. P. Liu, H. Zeng, S. H. Sun, Y. DingM, Z. L. Wang, Nano Letters, 2003, 3, 1647.

[46] B. D. Cullity, C. D. Graham, Introduction to Magnetic Materials, 2nd ed. Wiley, Hoboken, N.J., 2009.

[47] P. Kumar, H. No-Lee, R. Kumar, J Mater Sci Mater Electron. 2014, 25, 4553.

[48] H. Takahashi, S. Soeya, J. Hayakawa, K. Itp, A. Kida, C. Yamamoto, H. Asano, M. Matsui, J, Appl. Phys. 2003, 93, 8029.

[49] W. S. Seo, S. M. Kim, Y. M. Kim, X. Sun, and H. Dai, Small. 2008, 4, 1968.

[50] Q. C. Dong, G. J. Li, H. Wang, P. W. Pong, C. W. Leung, L. Manners, C. L. Ho, H. Li, W. Y. Wong, J. Mater. Chem. C. 2015, 3, 734.

[51] Z. Y. Pan, J. J. Lin, T. Zhang, S. Karamat, T. L. Tan, P. Lee, S. V. Springham, R. V. Ramanujan, R. S. Rawat, Thin Solid Films 2009, 8, 2753.

[52] T. Yokota, M. L. Yan, Y. F. Xu, L. Gao, R. Zhang, L. Nicholl, L. Yuan, R. Skomski, D. J. Sellmyer, S. H. Liou, C. H. Lai, C. H. Yang, S. H. Huang, J. Appl. Phys. 2005, 97, 10H306.

[53] J. A. Christodoulides, P. Farber, M. Daniil, H. Okumura, G. C. Hadjipanayis, V Simopoulos, D. Weller, IEEE Trans. Magn. 2001, 37, 1292.

[54] A. Butera, Eur. Phys. J. B. 2006, 52, 297.

[55] L. A. W. Green, Trinh T. Thuy, D. Mott, S. Maenosono, Nguyen T. K. Thanh, RSC Adv. 2014, 4, 1039.

Chapter 7 Conclusions and Future Work

7.1 Conclusions

This thesis mainly investigated wet chemical synthesis, magnetic and electrical properties of Fe-based systems in both nanoparticles and film forms which have drawn considerable attention for their wide range of applications recently. Firstly, the shapes, surface and magnetic properties of Fe_3O_4 nanoparticles were manipulated by introduction of external magnetic field during thermal decomposition process. The hyperthermia application of as-synthesized Fe_3O_4 in different shapes was studied. Furthermore, a simple and wide wet chemical route was demonstrated to deposit high-quality epitaxial thick Fe_3O_4 and ferrite film on different substrates. The potential applications of Fe_3O_4 had been explored for microwave absorption and MEMS supercapacitor. Typical Fe-3d metal alloy (FeCo) nanoparticles had been studied and a detail insight into the composition effect on the microstructure and magnetic properties was provided. The as-fabricated monodispersed FeCo nanoparticles were promising candidate for use in biomedicine according to cytotoxicity test. In addition, the similar wet chemical method that applied to deposit Fe_3O_4 film could also use to deposit FeCo film. The bcc-FeCo phase was identified by XRD and its magnetic property was investigated by VSM. Similarly, Fe-5d metal alloy (FePt) nanoparticle and film were also studied in our work. fcc-FePt nanoparticles had been synthesized with particle size around 15nm. $L1_0$-FePt films were achieved by a combination of chemical deposition of Pt-doped Fe films and post-annealing in furnace. The structure

and magnetic property of as-deposited and annealed FePt films with annealing temperatures were investigated.

The detailed results can be summarized below:

(1) An external magnetic field was utilized during thermal decomposition process to manipulate the shapes, surfaces and magnetic properties of Fe_3O_4 nanoparticles. The applied magnetic field of 500 Oe induced formation of uniform Fe_3O_4 nanocubes of 250 nm, in sharp contrast with the nanocuboctahedrons if no magnetic field was present. Size of Fe_3O_4 nanoparticles was also effectively controlled by adjusting the pre-heating time of reaction precursor. It is noticed that the magnetic field promotes the change of Fe_3O_4 nanocuboctahedrons to nanocubes and has no effect on nanooctahedrons. Furthermore, first-principles calculation was employed to understand the interaction between magnetic field and synthesized nanoparticles by studying surface magnetic anisotropy of Fe_3O_4 (001) and (111) surfaces. Moreover, Fe_3O_4 nanocubes and nanocuboctahedrons were coated with chitosan and well dispersed in water for hyperthermia measurement. The intrinsic loss power (ILP) of the Fe_3O_4 nanocubes (1.71 nH·m2/kg) was 56% higher than that of nanocuboctahedrons (1.09 nH·m2/kg) inferring surface magnetic effect on hyperthermia performance.

(2) A wet chemical (thermal decomposition method) had been presented for high-quality and epitaxial thick ferrite. A silicon-technology compatible process has been developed, that highly textured Fe_3O_4

can be grown on Si substrate with a MgO seed layer and patterned structure can be relatively easily realized. As-prepared Fe_3O_4 thick films have demonstrated their potential applications for microwave and MEMS supercapacitor. Different ferrite compounds have been successfully fabricated, including Co-ferrite with high coercivity and perpendicular anisotropy, and Ni-ferrite with high resistivity and enhanced magnetization.

(3) A facile chemical process has been developed for the preparation of magnetic Fe-3d alloy FeCo nanoparticles. The FeCo nanoparticles were mono-dispersed obtained by the safe and ecofriendly method, possessed saturation magnetization up to 187 emu/g and demonstrated excellent chemical stability. In this work, we have studied how to control Fe/Co ratio by variation of precursor ratio, and how to vary particle size from 9.3nm to 12.3nm by surfactant amount used. The cytotoxicity of as-synthesized nanoparticles was investigated after coating with the poly(methyl methacrylate-co-butyl acrylate) (PMBA) by the emulsion process and the results demonstrated high biocompatibility. Similarly, the same synthesis method was used with the single precursor FeO(OH) or Co_3O_4. The results showed that this method can also fabricate 10nm mono-dispersed spherical Fe_3O_4 particles and self-assembly Co nanoneedles. In addition, we had successfully deposit bcc-FeCo film on Pt substrate via thermal decomposition. The as-deposited FeCo film has the saturation magnetization around 1300emu/cc.

(4) fcc-FePt particles were synthesized through thermal decomposition. Its elemental composition was detected by EDS and their final particle composition was $Fe_{76}Pt_{24}$. The particle sizes observed form TEM were around 15 nm although it was not as uniform as the Fe_3O_4 and FeCo nanoparticles fabricated before. Compared with superparamagnetic behavior of disordered fcc-FePt phase, the VSM result showed nonzero value (150Oe) for the coercivity, indicating some amount of ordering should be present in fcc-FePt phase. In addition to FePt nanoparticle, a method to fabricate FePt films by a combination of chemical deposition and post-annealing had been presented. Pt-doped Fe films were deposited on Pt(100nm)/Ti(50nm)/SiO_2/Si substrate using thermal deposition and the as-deposited films were subsequently annealed from 300°C to 800°C under 5%H_2/95%N_2. FePt films were achieved through diffusion and rearrangement of Fe and Pt atoms in post-annealing process. From X-ray diffraction results, the fcc-FePt phase appeared at 300 °C and the transformation from fcc to $L1_0$ phase started at 400°C. The $L1_0$-FePt film possessed an out-of-plane anisotropy and a coercivity of 9 kOe after annealing at 600 °C. A further increase in annealing temperature led to lower value of coercivity, probably because of grain growth. In addition, the thickness of Pt-doped Fe films could be controlled from 150 nm to 700 nm by adjusting amount of the surfactant used. Our SQUID analysis showed that Pt dopant could significantly improve the chemical stability of Fe films in air.

7.2 Recommendations for future work

Based on the substantial experimental results, scientific discussion and conclusions drawn from this thesis, several potential directions for future research are presented:

(1) The work in the chapter 3 indicated that the shape, surface and magnetic properties of Fe_3O_4 could be manipulated by the external magnetic field. However the effect of external field on the other nanoparticles fabricated in our study (FeCo and FePt) is negligible. This is maybe because Fe_3O_4 is saturated at lower external filed (around 400 Oe) than that of FeCo and FePt observed from magnetic study. Further study may be focus on figuring out why the external magnetic field has more influences on the growth of Fe_3O_4 nanoparticle than other ferrous alloys. In addition, the external magnetic field could be used in the future study for controlling the growth and properties of other magnetic oxide nanoparticles as well as some magnetic semiconductors (TiO_2, ZnO).

(2) The potential of the solution-based method we presented for the deposition of thick films could be further explored in the future work. In our work, we have demonstrated that this method could be applied to deposit Fe-based films including, Fe_3O_4, ferrites, FeCo, FePt and Fe films. However, it would be interesting to broaden this method for growth of other oxide and metal films. Additionally, the quality of films deposited by this method is very different. Compared with high-quality epitaxial structure and smooth surface of as-deposited Fe_3O_4

and ferrites films, FeCo film that was deposited on Pt substrate has poor morphology, which is probably due to the poor matching between substrate and film or oxidation of FeCO film in air environment. Some work in the future could be concentrated on the improvement of quality of FeCo film by adjusting the thermal decomposition process.

(3) The excellent hyperthermia properties of Fe_3O_4 and biocompatibility of FeCo magnetic nanoparticles pave their ways for biomedicine applications in future. On the other hand, the poor disperbility and uniformity of as-synthesized FePt nanoparticle restricts us form further study on its potential for biomedicine use. In addition, because of the presence of ordering ($L1_0$) phase from our magnetic study, fcc-FePt nanoparticle shows non-superparamagnetic behavior and, thus, not desirable for biomedicine application. In terms of FeCo magnetic nanoparticles, in order to make it more suitable for biomedicine test, efforts should be made to increase this concentration after transferring to water phase.

Therefore, in future work, we will optimize reaction conditions and phase-transfer technique to achieve better quality of fcc-FePt nanoparticle and higher concentration of FeCo nanoparticle in water phase.

(4) We just have grabbed a small aspect of the epitaxial thick Fe_3O_4 films to investigate. There is still a broad scope of the research gaps to be fulfilled. Mechanism of growth of thick Fe_3O_4 and ferrites films by

thermal decomposition is rewarding to be further investigated. Some work could be done by comparing the magnetic properties, strain effect, and defect state of as-deposited thick epitaxial Fe_3O_4 with its bulk or thin counterparts.

(5) We have explored the use of as-deposited Fe_3O_4 for patterning, microwave absorbing and supercapacitor. Various ferrites films with high resistivity, high magnetization, and high coercivity were also obtained. Thus, investigation for their applications like, spintronics device, is counted for the days.